7-31-2020 2:30 PM

Experimental and Numerical Study on Three-Edge Bearing Test for Reinforced Concrete Pipe

Abdul-Aziz Younis, *The University of Western Ontario*

Supervisor: Nehdi, Moncef L., *The University of Western Ontario*

A thesis submitted in partial fulfillment of the requirements for the Master of Engineering Science degree in Civil and Environmental Engineering

Recommended Citation

Younis, Abdul-Aziz, "Experimental and Numerical Study on Three-Edge Bearing Test for Reinforced Concrete Pipe" (2020). *Electronic Thesis and Dissertation Repository*. 7146.
https://ir.lib.uwo.ca/etd/7146

Abstract

Reinforced Concrete Pipe (RCP) is widely used in storm and wastewater management owing to its resiliency and reliability. The century old Three-Edge Bearing Test (TEBT) is currently used to classify RCP strength. The test relies on the skill and experience of the operator for capturing the occurrence of a 0.3-mm-wide crack using a leaf-gauge, which induces subjectivity and error. Studies have also indicated the TEBT crack bears little structural significance.

This thesis aims at improving the TEBT by replacing the arbitrary crack-width with rational capacity-driven criteria. A wide range of full-scale RCP were instrumented and subjected to the modified TEBT to obtain load vs. deflection curves. Two rational criteria were developed to replace the arbitrary crack-width measurement, vastly improving the reliability of the TEBT. Parametric analysis was conducted on finite-element models (FEMs) to investigate the effect of RCP reinforcement area, yield strength, cover, and positioning on the proposed criteria.

Keywords: Reinforced Concrete Pipe; Three Edge Bearing Test; Steel Cage; Reinforcement; Design; D-Load; Standard; Finite Element Analysis; Concrete Damage; Plasticity.

Summary for Lay Audience

Reinforced-concrete pipe (RCP) is generally made with precast concrete and reinforced with one, two, or three layers of cages manufactured from steel wire. RCPs are buried underground and generally serve as wastewater sewers or stormwater drains. When buried, RCP must possess adequate mechanical strength to resist the weight of soil and any structures which may be built above. To ensure an that RCP can withstand the design loads, a specimen is tested by crushing it along its length and recording the load required to cause a 0.3-mm-wide crack to appear. This test is known as the Three-Edge Bearing Test (TEBT). The TEBT requires a human operator to determine when the specified crack occurs, which can lead to inaccuracies due to the operator calling the crack too early or too late. Furthermore, the 0.3-mm crack width was randomly selected and does not indicate a definite structural capacity.

To solve this problem, the present thesis investigates whether pipe strength can be classified based on load-deflection behaviour instead. Load-deflection is a plot of how much a given pipe specimen deflects (or deforms) as the applied load increases. The TEBT was carried out on full-scale RCP specimens instrumented with sensors, which measured the change in diameter during loading. Based on these results, modified TEBT criteria are suggested to replace the existing crack-measurement requirement. The suggested criteria should allow the industry to classify pipe based on rational scientific principles rather than error-prone crack measurements. To investigate the effect of reinforcement on the modified criteria, numerical models were created using computers to simulate RCP undergoing the TEBT. These simulations also provided some insight into how certain reinforcement variables can affect the overall load-deflection behaviour of RCP, providing benefit to the field of RCP design.

Co-Authorship Statement

This thesis has been prepared with adherence to the integrated-article format as set by the Faculty of Graduate Studies at Western University in London, Ontario, Canada. All experimental, analytical, and numerical work, along with writing of draft manuscripts, was carried out by Abdul-Aziz Younis under the supervision of Dr. M.L. Nehdi. Other co-authors assisted in experimental testing, verifying the numerical models, and/or revision of draft manuscripts. Based on Chapters 2, 3, and 4, the following articles have been submitted for publication to peer-reviewed technical journals:

1) **Younis, A.**, Ramadan, A., Wong, L.S., and Nehdi, M.L. "New Rational Test for Reinforced-Concrete Pipe Eliminating Subjective Crack-Width Criteria" *Structures, Elsevier*. Submitted.
2) **Younis, A.**, Shehata, A., Ramadan, A., Wong, L.S., and Nehdi, M.L. "Modeling Structural Behavior of Reinforced-Concrete Pipe with Single, Double and Triple Cage Reinforcement" *Engineering Structures, Elsevier*. Submitted.

Dedication

To My Mother, May Hani
My Father, Namir Younis
My Brother, Abdul-Kareem Younis

Acknowledgments

Recognizing the collaboration necessary for scientific discovery, Isaac Newton once wrote “If I have seen further, it is by standing on the shoulders of Giants”. I would like to recognize the Giants I have encountered on this journey, without whom this thesis would not exist.

Dr. Moncef L. Nehdi, for supervising and guiding me towards completion of my Master’s studies. I have learned many valuable life-lessons and skills during this exciting and fulfilling voyage which I owe to Dr. Nehdi’s support and instruction.

Sammy Wong, for his invaluable guidance, support, and mentorship throughout this undertaking. Sammy was present at every stage, and I can say without a doubt that I am a better professional and academic today because of his influence. I will miss the Monday discussions, where week-long clouds of confusion would be lifted in minutes.

The wonderful people at Con Cast Pipe, for their part in sponsoring this project both financially, logistically, and physically. Special thanks are due to the Quality Control departments at both Oakville & Guelph and all the workers we interacted with for making us feel like part of the team. I owe every single specimen tested in this thesis to their expertise, assistance, and patience.

Those who accompanied my journey at Western University, from staff, faculty, and friends, without whom this journey would not have been so fruitful. Although I do not have the space to list you all, I trust you know who you are and the difference you made.

Abdullah Ramadan, for his faithful role as my co-researcher and co-author, but most importantly as my friend. Whether working through late nights, early mornings, or both, Abdullah always somehow maintained an optimistic perspective regardless of the challenges and hurdles which we faced.

Finally, and above all else, I would like to express my endless appreciation and gratitude to my family. None of this would have been possible without their boundless support, motivation, and guidance throughout my life. I could write an entire thesis expressing my appreciation and it still would not be enough, so instead I dedicate this one to you.

Table of Contents

List of Tables

List of Figures

List of Symbols

δ	deflection as a percentage of the total pipe diameter (%)
A_s	area of reinforcing steel (mm^2/m)
A_{si}	area of inner-cage reinforcing steel (mm^2/m)
A_{so}	area of outer-cage reinforcing steel (mm^2/m)
A_{se}	area of elliptical-cage reinforcing steel in triple-cage pipe (mm^2/m)
D	load applied on a pipe specimen, given in units of Newton load per metre lay length per millimeter diameter (N/m/mm)
$D_{0.3}$	*D*-load at which a crack of width 0.3-mm and length of 300-mm is observed during the three-edge bearing test (N/m/mm)
D_{ult}	maximum *D*-load resisted by a pipe specimen during the three-edge bearing test (N/m/mm)
D_{peak}	maximum *D*-load resisted by a pipe specimen during the three-edge bearing test in the linear load-deflection phase before a sudden drop is observed (N/m/mm)
D_δ	*D*-load at a deflection of δ (N/m/mm)
f'_c	compressive strength of concrete (MPa)

List of Appendices

Chapter 1

Introduction

“For a long distance I caused a canal to be dug to the meadows of Nineveh. Over deep-cut ravines I spanned a bridge of white stone blocks. I caused those waters to flow over it.”

─ Inscription on the Aqueduct at Jerwan, 1500 B.C.

1.1 Background

The use of pipes as underground water conduits dates back thousands of years. Early urban developments in ancient Iraq saw terracotta clay pipes (**Fig. 1.1**) used to transfer waste-water beneath latrines from as early as 4000 B.C. (George, 2015). Later, the ancient Romans would construct large-scale pipeline projects using hydraulic cement and natural stone. One such example is the Cloaca Maxima, a sprawling underground sewer network used across several centuries (Hopkins, 2007). Some segments of the Cloaca are still functional today, demonstrating the long-term capabilities of underground concrete structures. In fact, the key advantage of modern concrete pipe over its steel and plastic counterparts is its proven performance spanning over 100 years of use. The US Army Corps of Engineers (USACE) recommends design lives of 70 – 100 years for concrete pipe, at least 50 years for steel pipe, and only 50 years for plastic pipe (USACE, 1998).

Figure 1.1: Pottery drain pipe with cuneiform inscriptions (left) and in-situ drains (right) found in Ur (from The Trustees of the British Museum).

Modern precast reinforced-concrete pipe (RCP) products are used globally to transport liquid in stormwater drains, sanitary sewers, and culverts. In Canada, the precast concrete pipe and block industry generated a revenue of CAD $1.2 billion in 2018. Concrete pipe products accounted for 35.1% of this revenue, or roughly $0.42 billion (Gonzales, 2018). Total industry revenue is projected to continue growing at an annual rate of 1%, reaching $1.3 billion by 2023 (Gonzales, 2018).

Although the use of unreinforced concrete pipe is permitted, most concrete pipes today are manufactured with steel reinforcement (OCPA, 2010). Steel reinforcement is fabricated as circular or elliptical cages spanning the length of the RCP product. Common RCP falls into one of three reinforcement configuration categories: single-cage, double-cage, and triple-cage. The reinforcement amount and configuration used varies depending on pipe size and project requirements.

Current industry practice worldwide relies on the century-old Three-Edge Bearing Test (TEBT) to assess the service and ultimate load capacities of RCP. The TEBT is used for both quality control inspections and proof-of-design verification. The test method relies on the skill and experience of the operator for capturing the occurrence of a 0.3-mm wide crack using a leaf-gauge, which induces subjectivity and error. For lined pipes, the liner must be stripped to expose part of the concrete for crack monitoring. This can misrepresent the true strength of the pipe, and in some cases the crack may be inaccessible or could form outside the stripped area. Furthermore, the significance of the 0.3-mm crack-width is questionable, as it is an arbitrary criterion based on measurability rather than structural performance (ACPA, 2007).

By investing in research, RCP industry stakeholders are looking to automate manufacturing and quality-control operations to increase output without greatly increasing labor costs (Gonzales, 2018). For the concrete pipe industry to remain competitive against other pipe industries, improved testing methods and technologies are needed to allow innovative products to be developed and to bridge the gap between the industry and emerging technologies.

1.2 Research Objectives

The TEBT crack-width criterion relies on human judgement in identifying the occurrence of a 0.3-mm wide crack. This allows for substantial subjectivity and error, while not assuring accurate comparison of RCP tested by different operators. Moreover, the relationship between specified crack-width and structural performance is unclear.

The primary objective of the research conducted in this thesis is to scrutinize the existing TEBT method and explore the feasibility of adopting rational load-deflection criteria rather than the current operator-sensitive crack inspection criteria. Specific objectives are as follows:

1) Identify motives and reasoning behind the 0.3-mm crack measurement criterion.
2) Study and compare load-deflection behaviour of RCP with single, double, and triple-cage reinforcement undergoing the TEBT.
3) Assess the possibility of eliminating the 0.3-mm crack measurement criterion in favour of capacity-driven criteria.
4) Develop finite-element models (FEMs) representing the three standard cage-configurations of RCP to explore stress development and propagation in the RCP concrete and steel during the TEBT.
5) Perform a reinforcement-based parametric study to investigate the effects of certain design variables on the load-deflection response of RCP.

1.3 Original Contributions

The research presented in this thesis serves industry and academia by bridging advances in both sectors to fill a knowledge gap relating to RCP. Previous studies have overwhelmingly focused on steel-fibre reinforced concrete pipe (SFRCP), neglecting the more commonly used RCP cage reinforcement designs. Research regarding larger, more costly triple-cage RCP is especially absent. Over the past decade, research involving the TEBT has often made use of deflection sensing technologies to better understand RCP and SFRCP behaviour, however there is a distinct lack in research discussing the viability of replacing the crack-width measurement with these rational methods.

This thesis helps address the problem via providing the following specific original contributions:

1) Detailed experimental study on over 40 full-scale RCP specimens, generating and discussing load-deflection behaviour for a variety of pipe sizes, cage configurations, and classes, including the rarely studied triple-cage configuration.

2) Recommended two new rational criteria (D_{peak} & $D_{\delta = 0.36\%}$) for comparing RCP strength based on load-deflection output.

3) For the first time in the open literature, developed a FEM for triple-cage RCP specimen calibrated using actual load-deflection results. Single and double-cage FEMs were also developed, and a detailed discussion of the stress propagation in the concrete and steel during the TEBT was presented.

4) Performed an in-depth reinforcement-based parametric study on single and double-cage RCP FEMs by varying reinforcement parameters relevant to industry design methods. Effects of these parameters on D_{peak} and $D_{\delta = 0.36\%}$ were also investigated.

1.4 Thesis Structure

This thesis has been structured and prepared according to the integrated-article format per the guidelines of the Faculty of Graduate Studies at Western University, Canada. It contains five chapters covering the behaviour of common RCP configurations undergoing the TEBT.

Chapter two provides a historical background and review of TEBT research. The development of the TEBT into its current form is discussed, and an in-depth explanation of the procedure is provided. Additionally, a review of relevant state-of-the-art methodologies and research is included.

Chapter three presents the results of an extensive experimental program encompassing a wide range of common RCP sizes and classes. Load-deflection data was analyzed for all specimens and compared based on cage configuration. From these results and analysis, two rational criteria for determining pipe class without measuring crack-width are suggested.

Chapter four details the development and validation of 3D finite-element models representing 825-mm, 1200-mm, and 1800-mm RCP undergoing the TEBT. The pipe sizes were selected in order to cover the three traditional RCP cage configurations considered in the research. The FEMs provided insight into the state of stress in the concrete and steel material of RCP during TEBT loading. Using the FEMs, a reinforcement-based parametric study was conducted to explore the effect of relevant reinforcement variables on load-deflection behaviour of RCP. The effect of these parameters on the criteria suggested in Chapter 3 was also studied.

Chapter five completes the thesis by summarizing key research conclusions, stating the limitations of this work, and offering suggestions and recommendations for future research.

1.5 References

ACPA. (2007). *Cracks in Installed Reinforced Concrete Pipe* (Resource No. 02–712; Concrete Pipe Information). American Concrete Pipe Association. http://www.concretepipe.org

George, A. R. (2015). On Babylonian Lavatories and Sewers. *Iraq*, *77*, 75–106. https://doi.org/10.1017/irq.2015.9

Gonzales, E. (2018). *Concrete Pipe & Block Manufacturing in Canada* (Industry Report No. 32733CA). IBISWorld.

Hopkins, J. N. N. (2007). *The Cloaca Maxima and the Monumental Manipulation of Water in Archaic Rome*. *4*, 15.

OCPA. (2010). *Concrete Pipe Design Manual*. Ontario Concrete Pipe Association. http://www.ocpa.com

USACE. (1998). *Conduits, Culverts, and Pipes* (Engineer Manual No. EM1110-2–2909; Engineering and Design). U.S. Army Corps of Engineers.

Chapter 2

Literature Review

2.1 Introduction

This chapter provides an in-depth literature review concerning the Three-Edge Bearing Test (TEBT). The history of early North American pipe strength tests leading to the development of the TEBT is investigated, followed by an explanation of current TEBT specifications and limitations. Finally, relevant research developments on the TEBT are reviewed and summarized.

2.2 History of North American Pipe Strength Tests

During the late-1800s and throughout the 1900s, using precast concrete pipe became increasingly common across Canada and the US. Early concrete pipes often suffered cracking issues after installation due to lack of understanding of pipe design at the time. Preliminary load tests were mainly used to assess the effects of certain variables on pipe strength (Carleton *et al.*, 2017). Extensive research carried out by Marston & Anderson in 1913 was crucial in setting a foundation for understanding pipe behaviour under loading. The research was also a first step towards exploring the correlation between pipe performance under load tests and actual in-situ soil loads. Marston and Anderson used the Ames Standard Testing Machine, a precursor of the hydraulic pipe-testing machines used today. Ames machines rested the test specimen between two sandboxes, with load being applied through the upper box, as shown in **Fig. 2.1** (Marston & Anderson, 1913). A drawback of the Ames machine – and similar sand-bearing tests – was the complexity of their standards, as well as the general disorder caused when dealing with sand. Specific machine parameters, such as the size of the sand containers, needed to change depending on the size of the tested pipe.

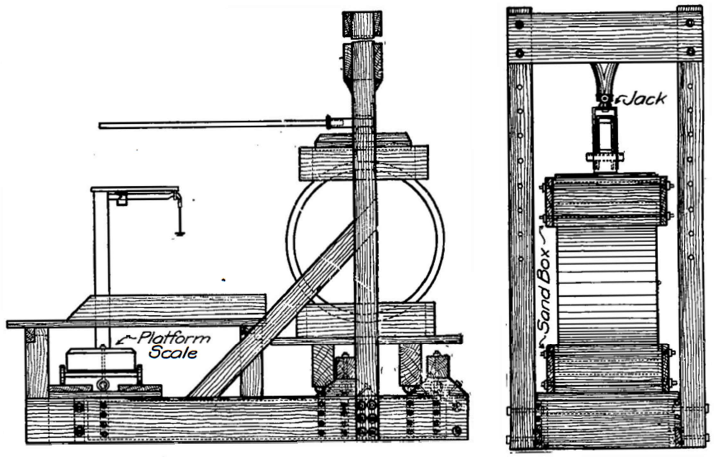

Figure 2.1: The Ames Standard Testing Machine (Marston & Anderson, 1913, with permission).

Two-edge bearing tests – where the pipe specimen would be pinched along its lower and upper lengths by two edges – were also available, but were discontinued due to the unwarranted challenge associated with balancing a heavy concrete pipe on a one-inch bearing (Carleton *et al.*, 2017). Preliminary three-edge bearing tests existed, although at the time no unifying standards were available. Three-edge bearing tests would rest the pipe specimen between two edges running along its bottom length, with a third edge applying load along the top length of the pipe. While the sand-bearing test method provided a direct assessment of in-situ strength, Marston found in 1917 that the three-edged bearing method could predict in-situ strength by multiplying the result by a factor of 10/7 (Carleton *et al.*, 2017).

General practice at the time saw two minimum load criteria being assessed by the three-edge bearing method; first-crack load and ultimate load. First-crack load refers to the load at which the first visible crack is observed on the pipe face, while ultimate load refers to the maximum load the pipe withstands before collapse (Spangler, 1967). Determining the exact load at which the first visible crack occurs was found to be a challenging undertaking, clouded in uncertainty due to the various factors associated. Spangler (1967) credits W.J. Schlick with determining "light conditions in the laboratory, surface texture of the test specimen, and even the visual acuity of the observer" as the main factors affecting the first-crack reading. To overcome these uncertainties, Schlick recommended crack-load be based on a crack of width 0.01-in. (0.3-mm) rather than the first visible crack (Spangler, 1967). Schlick is believed to have arbitrarily selected 0.3-mm as the critical crack-width based on the leaf-gauge in his possession. Serendipitously, it would later be found that smaller cracks would often close through autogenous healing, and larger cracks may lead to corrosion and durability concerns (Watkins, 1999, p. 142). Following Schlick's suggestion, the 0.3-mm crack-width criterion was adopted in the first tentative ASTM three-edge bearing test standard, sometime in the 1930s (Spangler, 1967). ASTM would continue to permit strength tests to be conducted via the three-edge bearing or sand-bearing methods, until ASTM C76-65T removed the obsolete sand-bearing test method (Spangler, 1967).

It should also be noted here that while the 0.3-mm crack provides a useful measurable criterion for assessing RCP, it does not necessarily indicate a pipe's true structural capacity. With regards to healing, recent studies by Suleiman *et al.* (2019; 2018) have shown that autogenous healing is heavily dependent on environmental factors and not solely crack-width. In the studies, cracks exposed to cyclic changes in temperature and relative humidity did not exhibit self-healing, even when crack widths were as low as 0.15-mm (2018, p. 6).

2.3 Existing Three-Edge Bearing Test

The existing Three-Edge Bearing Test (TEBT) is a widely-used crushing test in precast concrete pipe industries around the world. Despite today's hyper-connected world, many different versions of the TEBT exist in international RCP standards. Wong and Nehdi (2018) provide an in-depth analysis of a range of international RCP standards and compare their crushing test requirements. In some standards, such as the UK standard, up to four bearing edges are used, whereas others only require two bearings. The TEBTs defined under the North American ASTM C497 (2018) and CSA A257 (2014) standards were found to be largely identical in most criteria. The scope of the present study will be limited to the North American form of the TEBT, specifically the CSA A257 standard.

For context, it should be noted that the load test forms one of four acceptance criteria for RCP in Canada. CSA A257.2 (2014, pp. 31–53) prescribes the RCP acceptance criteria as follows: i) Strength test, in the form of (a) concrete cylinder tests to verify the concrete design compressive strength, and (b) the Three-Edge Bearing Test to verify the pipe design class; ii) Absorption test to ensure that the water absorption of concrete is limited to 9% (when specified by the owner); iii) Hydrostatic test to ensure that pipes do not leak under hydrostatic pressure (when specified by the owner); and iv) Visual inspection to ensure that product labelling and conditions conform to specification requirements.

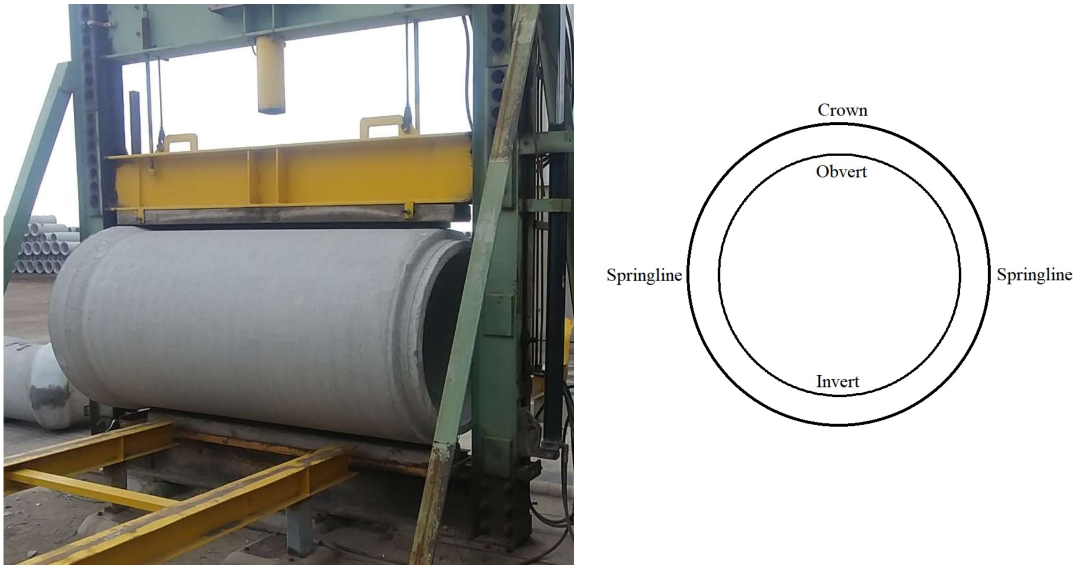

Figure 2.2: TEBT setup following CSA A257 (left) and pipe cross-section with labelled regions (right).

Per CSA A257.0 (2014, pp. 3–15), the TEBT is conducted by placing the concrete pipe specimen upon two longitudinal rubberized bearing strips, as shown in **Fig. 2.2**. The gap between the bottom two rubber bearings is defined to be 25-mm for every 300-mm of internal pipe diameter. The Shore Durometer hardness of the rubber is required by the standard to be in the range of 45 to 60. The specimen is then loaded at a rate of 7 to 37-kN/min/m through a third rubberized bearing strip placed longitudinally above the pipe. As loading increases, cracks tend to form on the pipe invert and obvert, followed by cracks on the outer walls at the spring-line. The maximum load supported before the formation of a crack that is 0.3-mm wide and 300-mm long is recorded as the '0.3-mm crack load' (referred to in this Chapter as $D_{0.3}$-load for brevity). The 0.3-mm wide crack is determined using a leaf-gauge specified within the standard. The standard defines the ultimate load

(D_{ult}-load) simply as the largest load supported by the pipe. $D_{0.3}$ and D_{ult} are calculated in units of Newton force per metre length of pipe per millimetre diameter, i.e. N/m/mm. Factors of safety for pipe classes between 100D and 140D are linearly interpolated between 1.5 and 1.25, respectively. The equivalent pipe class is calculated per **Eq. 1**.

$$\text{Equivalent Class} = \text{minimum of } \begin{cases} D_{0.3} \\ \dfrac{D_{ult}}{FS} \end{cases} \qquad \text{Eq. 1}$$

Where *FS* is 1.5 for design class 100D and below ($D_{ult} \leq 150$) and 1.25 for design class 140D and above ($D_{ult} > 175$). For $150 < D_{ult} \leq 170$, *FS* is linearly interpolated between 1.5 and 1.25.

The TEBT's 100-year history is a testament to its reliability and usefulness. However, there are several key issues associated with the procedure. One of the most notable shortcomings of the TEBT is its reliance on human judgement to determine when the 0.3-mm wide, 300-mm long crack occurs. With larger diameter pipes, several cracks tend to develop before the $D_{0.3}$-load is reached, requiring the operator to monitor and gauge several cracks simultaneously. This – along with operator speed, judgement, and attentiveness – can lead to inconsistencies in data reporting between different operators, depending on their experience and skill.

2.4 Further Developments of Three-Edge Bearing Test

Various research studies have validated the use of Linear Variable Differential/Inductive Transducers (LVDTs) with the TEBT as a viable means of assessing and comparing pipe performance (Abolmaali et al., 2012; de la Fuente, Escariz, et al., 2012; Figueiredo et al., 2012; Mohamed et al., 2014, 2015; Park et al., 2015; Peyvandi et al., 2013; Silva et al., 2018; Wilson & Abolmaali, 2014). Figueiredo (2012) proposed a tentative modified testing method for steel-fibre reinforced-concrete pipe (SFRCP) undergoing TEBT. The TEBT specification being considered was the European EN-1916 standard, as well as the

Brazilian ABNT NBR-8890 standard. Both standards require the use of loading cycles, where the pipe is first loaded to its required ultimate load, then unloaded and reloaded to its required service load. Figueiredo proposed D-load for SFRCP be taken as the load corresponding to a 0.4% crown displacement, and the ultimate load be taken as the load corresponding to 2% displacement. However, it was also suggested that further research be carried out in order to confirm and lend a higher degree of confidence to the findings.

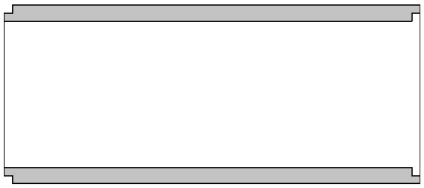

(a) OJP

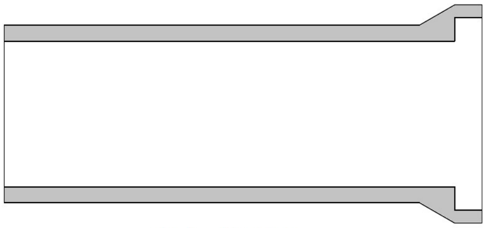

(b) SPP

Figure 2.3: Longitudinal cross-section of (a) Ogee-Joint Pipe and (b) Spigot-Pocket Pipe (From Da Silva, 2011, with permission).

Silva (2018) used load-deflection profiles to assess the behaviour of ogee-joint pipes (OJP) against spigot-pocket pipes (SPP), shown in **Fig. 2.3**. The research was conducted on specimens having one and two lines of reinforcement (single and double-cage, respectively). Single-cage OJP and SPP specimens experienced sharp but temporary loss of load capacity beyond the linear-elastic deformation phase, before regaining strength in the plastic deformation phase. Double-cage SPP also experienced a similar loss of strength. However, double-cage OJP specimens did not experience a significant loss of strength at cracking, but rather underwent a more gradual shift between elastic and plastic load-deformation behaviour. **Table 2.1** surveys LVDT placement in current literature. Most of the existing literature favours measuring deflections at the spigot, as that is the critical section due to its lower rigidity compared to the socket.

Table 2.1: Number and positioning of displacement sensors in existing literature.

Research	Total LVDTs used	Positioning of sensors	Comments
De la Fuente *et al.* (2012)	2	Spigot obvert, socket obvert	Sensors were fixed at inverts, so only obvert displacement was needed to measure net vertical deflection.
Figureiredo *et al.* (2012)	2	Spigot overt, socket obvert	Sensors fixed at inverts. Spigot deflections were found to be more critical due to lower structural rigidity.
Abolmaali *et al.* (2012)	2 wire potentiometer displacement sensors	Vertically and horizontally at spigot	Wire potentiometers were fixed to inner pipe face, measuring net vertical/horizontal deflection.
Peyvandi *et al.* (2013)	1	Unclear	–
Wilson *et al.* (2014)	2 wire potentiometer displacement sensors	Vertically and horizontally at spigot	Sensors fixed to inner pipe face.
Park *et al.* (2015)	2 wire potentiometer displacement sensors	Vertically and horizontally at spigot	Sensors fixed to inner pipe face.
Mohamed *et al.* (2014)	2	Spigot obvert, socket obvert	Sensors fixed to inner pipe face.
Mohamed *et al.* (2015)	3	Spigot obvert and springlines	Obvert sensor fixed to invert.
Da Silva *et al.* (2018)	12	3 vertical pairs, 3 horizontal pairs	Each pair positioned in opposite directions to measure net vertical/horizontal deflection.

2.5 Conclusions

In this chapter, the history of early concrete pipe strength tests leading up to the current TEBT was discussed to provide contextual background. Although the existing standard TEBT is a clear improvement over preliminary sand-bearing and two-edge bearing tests, some limitations still exist. The three key limitations of the present TEBT are as follows:

1. The TEBT is operator sensitive due to its reliance on human judgement in assessing the formation of a 0.3-mm wide, 300-mm long crack.
2. The TEBT classes pipes based on occurrence of the 0.3-mm wide crack, although the significance of this crack-width is dubious and not indicative of structural capacity.
3. The TEBT is a costly test due to its destructive nature, but in its standardized form provides limited information to engineers regarding the behaviour of RCP specimens under load.

Over the past decade, research involving the TEBT has increasingly made use of deflection sensors to overcome these limitations. Assessing TEBT load-deflection response yields greater insight into the performance of concrete pipe. Despite these advances in academia, industry is yet to benefit from these TEBT alterations. This can be attributed to a lack of research specifically investigating the feasibility of classing RCP using load-deflection profiles.

Furthermore, much of the current TEBT research centres on steel-fibre reinforced-concrete pipe (SFRCP), overlooking the more common cage RCP configurations. Additionally, RCP research is often limited to single and double-cage specimens, with larger triple-cage RCP not being considered.

These elements indicate clear need for research to study a range of RCP diameters reinforced using common industry configurations, with the goal of assessing the viability of classing RCP based on load-deflection data obtained from the TEBT.

2.6 References

Abolmaali, A., Mikhaylova, A., Wilson, A., & Lundy, J. (2012). Performance of Steel Fiber–Reinforced Concrete Pipes. *Transportation Research Record: Journal of the Transportation Research Board*, *2313*(1), 168–177. https://doi.org/10.3141/2313-18

ASTM C497-18. (2018). *Test Methods for Concrete Pipe, Manhole Sections, or Tile*. ASTM International. https://doi.org/10.1520/C0497-18

Carleton, E., Hiner, S., & Kurdziel, J. (2017). The History and Application of the Three-Edge Bearing Test for Concrete Pipe. In J. J. Meyer & J. Beakley (Eds.), *Concrete Pipe and Box Culverts* (pp. 18–27). ASTM International. https://doi.org/10.1520/STP160120160118

CSA A257. (2014). *Standards for Concrete Pipe and Manhole Sections* (p. 92). CSA Group.

de la Fuente, A., Escariz, R. C., de Figueiredo, A. D., Molins, C., & Aguado, A. (2012). A new design method for steel fibre reinforced concrete pipes. *Construction and Building Materials*, *30*, 547–555. https://doi.org/10.1016/j.conbuildmat.2011.12.015

Figueiredo, A., de la Fuente, A., Molins, C., & Aguado, A. (2012). A New Approach on Crushing Strength Test for Fibre Reinforced Concrete Pipes. *8th RILEM International Symposium on Fibre Reinforced Concrete: Challenges and Opportunities (BEFIB2012)*, 1082–1095.

Marston, A., & Anderson, A. O. (1913). The Theory of Loads on Pipes in Ditches, and Tests of Cement and Clay Drain Tile and Sewer Pipe. *Iowa State College of Agriculture and Mechanic Arts*, *11*(5).

Mohamed, N., Soliman, A. M., & Nehdi, M. L. (2014). Full-scale pipes using dry-cast steel fibre-reinforced concrete. *Construction and Building Materials*, *72*, 411–422. https://doi.org/10.1016/j.conbuildmat.2014.09.025

Mohamed, N., Soliman, A. M., & Nehdi, M. L. (2015). Mechanical performance of full-scale precast steel fibre-reinforced concrete pipes. *Engineering Structures*, *84*, 287–299. https://doi.org/10.1016/j.engstruct.2014.11.033

Park, Y., Abolmaali, A., Mohammadagha, M., & Lee, S. (2015). Structural performance of dry-cast rubberized concrete pipes with steel and synthetic fibers. *Construction and Building Materials*, *77*, 218–226. https://doi.org/10.1016/j.conbuildmat.2014.12.061

Peyvandi, A., Soroushian, P., & Jahangirnejad, S. (2013). Enhancement of the structural efficiency and performance of concrete pipes through fiber reinforcement.

Construction and Building Materials, *45*, 36–44. https://doi.org/10.1016/j.conbuildmat.2013.03.084

Silva, J. L. da, El Debs, M. K., & Kataoka, M. N. (2018). A comparative experimental investigation of reinforced-concrete pipes under three-edge-bearing test: Spigot and Pocket and Ogee Joint pipes. *Acta Scientiarum. Technology*, *40*(1), 30860. https://doi.org/10.4025/actascitechnol.v40i1.30860

Spangler, M. G. (1967). The Case Against the Ultimate Load Test for Reinforced Concrete Pipe. *Highway Research Record*, *176*, 35–42.

Suleiman, Ahmed R., Nelson, A. J., & Nehdi, M. L. (2019). Visualization and quantification of crack self-healing in cement-based materials incorporating different minerals. *Cement and Concrete Composites*, *103*, 49–58. https://doi.org/10.1016/j.cemconcomp.2019.04.026

Suleiman, A.R., & Nehdi, M. L. (2018). Effect of environmental exposure on autogenous self-healing of cracked cement-based materials. *Cement and Concrete Research*, *111*, 197–208. https://doi.org/10.1016/j.cemconres.2018.05.009

Watkins, R. K. (1999). *Structural Mechanics of Buried Pipes*. CRC Press. https://doi.org/10.1201/9781420049572

Wilson, A., & Abolmaali, A. (2014). Performance of Synthetic Fiber-Reinforced Concrete Pipes. *Journal of Pipeline Systems Engineering and Practice*, *5*(3), 04014002. https://doi.org/10.1061/(ASCE)PS.1949-1204.0000166

Wong, L. S., & Nehdi, M. L. (2018). *Critical Analysis of International Precast Concrete Pipe Standards*.

Chapter 3

Rational Test for Reinforced-Concrete Pipe Eliminating Subjective Crack-Width Criteria

3.1 Introduction

In this chapter, an experimental study was undertaken to scrutinize the existing methods of testing RCP using the three-edge bearing test (TEBT) and explore the feasibility of modifying the existing TEBT standard to adopt more scientific load-deflection criteria rather than operator sensitive crack inspection criteria.

3.2 Experimental Program

3.2.1 Materials and Specimen Preparation

A total of 43 full-scale RCP specimens were manufactured using the dry-cast method at an industrial precast concrete pipe manufacturing facility based in Ontario, Canada. Specimens ranged in diameter from 450-mm to 2400-mm, covering a wide range of RCP used in practice. The three traditional cage-configurations, shown in **Fig. 3.1**, were investigated.

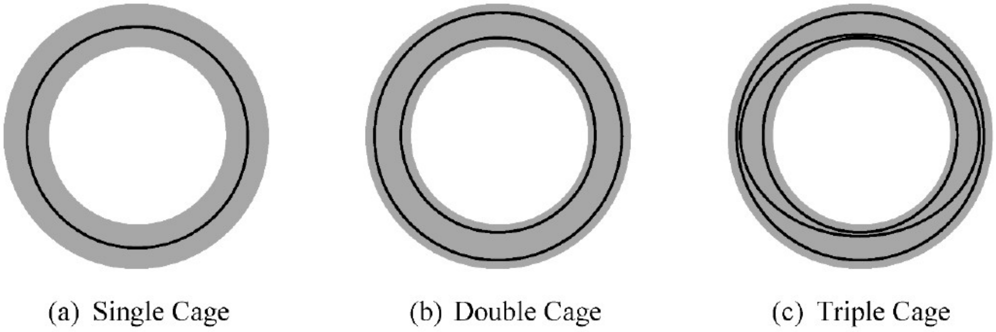

(a) Single Cage (b) Double Cage (c) Triple Cage

Figure 3.1: Traditional RCP cage configurations (Wong, 2018, with permission).

Smaller sized pipes (up to and including 825-mm) were manufactured using a single-cage of steel reinforcement. Mid-size pipes (between 825-mm and 1200-mm) were manufactured using the double-cage configuration. Larger pipes (1800-mm and greater) were manufactured using the triple-cage configuration of two circular cages and one elliptical cage, apart from two 1950-mm specimens manufactured using the double-cage configuration. One 2100-mm and all 2400-mm diameter specimens were manufactured with stirrups. RCP specimens having a diameter smaller than 1050-mm were manufactured using the SPP shape, with remaining RCP specimens manufactured using the OJP shape shown previously in **Fig. 2.3**.

Specimens were manufactured based on common industry design classes of 65D, 100D, and 140D. Specimen manufacturing methods adhered to the specifications prescribed in CSA A257.2 (2014) and ASTM C76 (2016). It should be noted that design classes do not indicate actual equivalent classes; a pipe designed for a certain class may in fact have a smaller or larger equivalent class depending on its performance under the TEBT. Regardless of design class, all specimens used a dry-cast zero-slump concrete mixture. Concrete pipes were removed from the mold after vibration, followed by steam curing for an 8-hour minimum period. Compressive strength cylinders were tested at 7, 28, and 120 days to establish a strength profile for the concrete and estimate pipe concrete strength based on age, as shown in **Fig. 3.2**.

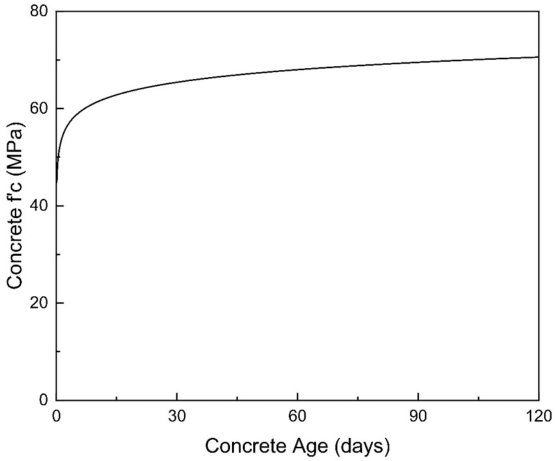

Figure 3.2: Strength gain over time from concrete cylinder tests.

Reinforcing steel was made into spiral helical cage using cold-drawn deformed-wire. The wire diameter varied from 6.07-mm to 11.46-mm depending on the size and class of RCP. The wire was manufactured in accordance with ASTM A1064/A1064M (2018) with yield and tensile strengths of 550 MPa and 620 MPa, respectively.

The RCP specimen test data was grouped by cage configuration and presented in **Tables 3.1** to **3.3**. Each specimen was given a label in the following format: [nominal diameter]-[design class]-[specimen number]. For example, 1200-065-2 is the second 1200-mm 65D RCP specimen. Specimens containing stirrups were marked with (S) following their label. A_{si} refers to the inner cage area of steel, while A_{so} refers to the outer cage area of steel, and A_{se} refers to the area of steel of the elliptical cage in triple-cage specimens. All steel areas were measured in millimeter squared per meter lay length of pipe.

Table 3.1: Single-cage RCP specimen properties

Pipe	**Diameter (mm)**	**Wall (mm)**	***Asi* (mm^2/m)**	**f'_c (MPa)**	**Age (days)**
450-140-1	457.2	83	290	59.1	9
525-140-1	533.4	89	290	57.8	7
525-140-2	533.4	89	290	61.0	13
600-140-1	609.6	95	484	81.7	727
600-140-2	609.6	95	484	81.7	727
675-140-1	685.8	102	645	81.2	662
675-140-2	658.8	102	645	81.2	658
750-100-1	762.0	108	415	69.5	68
750-100-2	762.0	108	415	69.5	67
825-065-1	838.2	114	290	60.2	11
825-065-2	838.2	114	290	60.2	11
825-065-3	838.2	114	290	60.2	11
825-100-1	838.2	114	484	71.5	99
825-100-2	838.2	114	484	76.1	244

Table 3.2: Double-cage RCP specimen properties

Pipe	Diameter (mm)	Wall (mm)	*Asi* (mm^2/m)	*Aso* (mm^2/m)	*f'$_c$* (MPa)	Age (days)
825-140-1	838.2	121	581	323	63.7	22
900-140-1	914.4	121	645	393	65.8	33
900-140-2	914.4	121	645	393	65.8	33
975-100-1	990.6	127	387	290	60.2	11
975-140-1	990.6	127	753	452	66.5	38
1050-100-1	1066.8	133	581	290	60.2	11
1050-140-1	1066.8	133	1129	452	82.1	782
1200-065-1	1219.2	127	565	376	59.7	10
1200-065-2	1219.2	127	565	376	59.7	10
1200-065-3	1219.2	127	565	376	59.7	10
1200-100-1	1219.2	127	821	645	57.8	7
1200-140-1	1219.2	127	1548	645	57.0	6
1200-140-2	1219.2	127	1548	645	61.8	15
1950-100-1	1981.2	191	1721	968	59.1	9
1950-100-2	1981.2	191	1721	968	59.1	9

Table 3.3: Triple-cage RCP specimen properties

Pipe	Diameter (mm)	Wall (mm)	*Asi* (mm^2/m)	*Aso* (mm^2/m)	*Ase* (mm^2/m)	*f'$_c$* (MPa)	Age (days)
1800-100-1	1828.8	178	822	452	1290	57.8	7
1800-140-1	1828.8	178	1807	775	1290	55.0	4
1800-140-2	1828.8	178	1807	775	1290	55.0	4
1800-140-3	1828.8	178	1807	775	1290	55.0	4
2100-100-A1	2133.6	203	1334	431	1075	57.8	7
2100-100-B1	2133.6	203	258	258	774	65.8	33
2100-100-B2	2133.6	203	258	258	774	65.8	33
2250-140-1	2286.0	216	2592	1331	1588	57.8	7
2250-14-2	2286.0	216	2194	646	903	58.5	8
2250-14-3	2286.0	216	2194	646	903	58.5	8
2100-140-1 (S)^A	2133.6	203	1596	1596	1189	64.0	23
2400-140-1 (S)^B	2436.0	233	1549	1291	1290	62.7	18
2400-140-2 (S)^B	2433.0	233	1549	1291	1290	62.7	18
2400-140-3 (S)^B	2439.0	233	1549	1291	1290	64.2	24

(S)^A Stirrup area = 245 mm^2/m.
(S)^B Stirrup area = 382 mm^2/m

3.2.2 Testing Equipment and Apparatus

Testing was carried out using TEBT machines typical of that used by quality control departments located at industrial RCP manufacturing facilities. The two TEBT machines used were Hydrotile hydraulic presses capable of applying a maximum load of 560-kN for pipe diameters lower than 1500-mm, and 1200-kN for pipe diameters larger than 1500-mm. A pair of LVDT sensors were used to measure deflections during testing. These sensors were supplied by Alliance Sensors Group and have stroke ranges of 101.6-mm and 50.8-mm, and linearity error of ±0.15%. The 101.6-mm stroke range was used to measure deflections at the pipe obverts, since preliminary tests revealed obvert deflections to be larger than invert deflections. Load and deflection sensor signals were resolved using data-logger modules supplied by ICP DAS. The data-logger output real-time readings and recorded data every second to a tablet PC. A rough schematic of the wire connections between the apparatus elements is shown in **Fig. 3.3**.

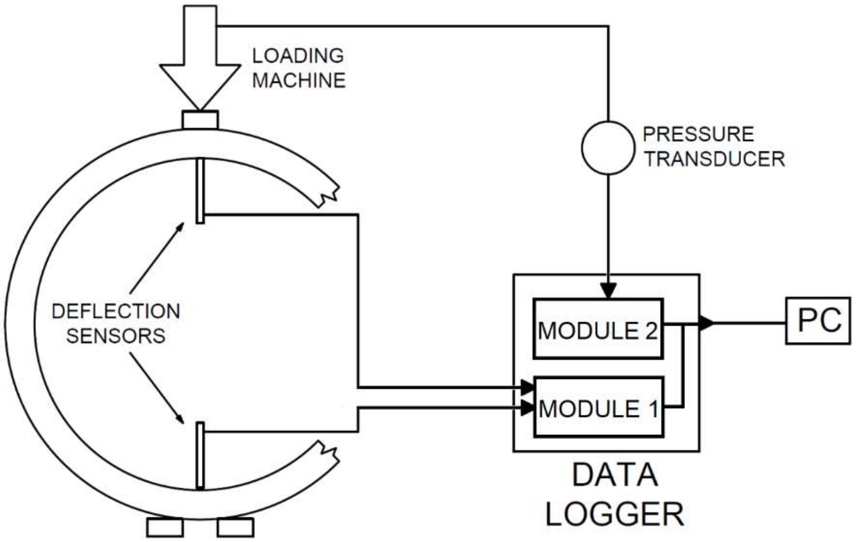

Figure 3.3: Schematic showing positioning of deflection sensors and load on pipe specimen, and connections between the test equipment. Modules 1 and 2 resolve signals from the deflection sensors and pressure transducer (load cell), respectively. Both modules are enclosed within the data-logger, and output results via ethernet connection to the tablet PC.

3.2.3 Experimental Procedures

Testing was carried out per CSA A257.0 (2014) guidelines, which are almost identical to the ASTM C497 (2018) specifications (Wong & Nehdi, 2018). Once the pipe was positioned as required for the TEBT, the two LVDT displacement sensors were positioned at the spigot invert and obvert to measure vertical deflections during the test. **Figure 3.4** (left) shows the positioning of the displacement sensors for small diameter pipes. LVDT sensors were fastened to solid aluminum vertical rods, which in turn were connected to horizontal rods extending from a custom-made steel bracket. The steel bracket was clamped to the hydraulic machine supports as shown in **Figure 3.4** (right). While one operator controlled and maintained a constant loading rate, a second operator monitored and noted critical cracks occurring on the concrete face.

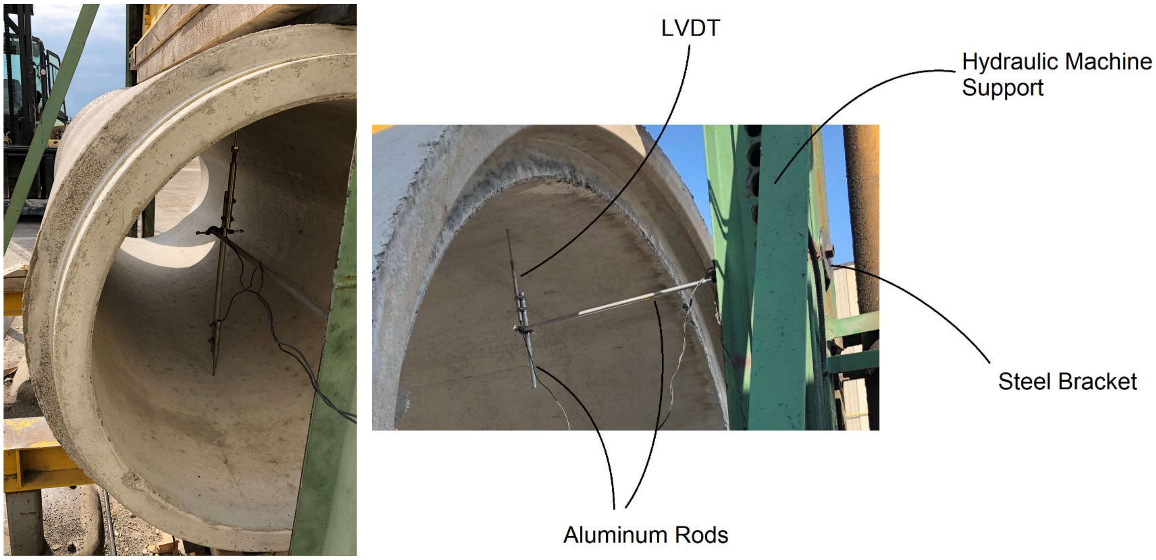

Figure 3.4: Positioning of displacement sensors (left), mounting of LVDT sensors on a large diameter pipe (right). Large diameter pipes required sensors to be mounted separately due to the large invert-obvert distance.

The 0.3-mm wide crack was determined using a leaf gauge, as shown in **Fig. 3.5**. Loading continued until the pipe reached ultimate failure and was unable to resist further load, at which point the test was complete.

Figure 3.5: Leaf gauge indicating a 0.3mm crack while an LVDT sensor measures deflection.

During testing, the operator monitoring crack patterns on the pipe specimen records three critical loads: i) First-crack load: the load at which the first hairline crack was observed; ii) Multiple-crack load: the load at which multiple hairline cracks were observed, if they form; and iii) the $D_{0.3}$-load: the load at which a 0.3-mm wide crack is observed. Upon test completion, the gathered data was used to generate load-deflection curves from which further data points can be obtained and have been defined in this study as: i) D_{peak}-load: a value which is observed based on the largest load sustained by the specimen during the initially linear behaviour of the load-deflection profile, before a significant drop marks the onset of plastic behaviour; ii) D_{δ}-load: which corresponds to the load at a deflection δ (**Fig. 3.6**); and iii) D_{ult}-load: a value that is observed based on the maximum load captured by the instrumentation. **Figure 3.7** presents a typical RCP load-deflection curve marked with locations of D_{peak}, D_{δ}, and D_{ult}. $D_{0.3}$ and D_{ult} are used in the standard TEBT to classify pipes as explained by **Eq. 1** outlined in the previous chapter. D_{peak} and D_{δ} have been defined to discuss load-deflection phenomena in this study. All D-load values are normalized as measured load in Newton per millimeter pipe diameter per metre lay length (N/m/mm). Expressing D-load values in N/m/mm allows for direct comparison between pipe class and D-loads across all pipe sizes.

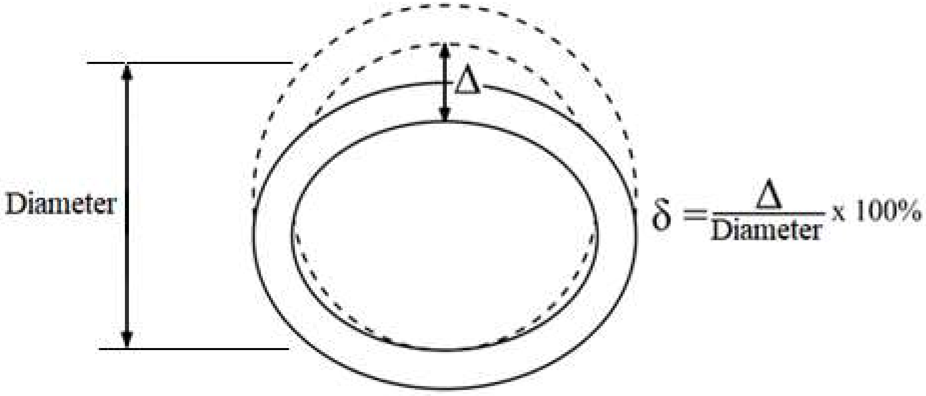

Figure 3.6: Calculation of deflection percentage, δ, used for D_{δ}-load.

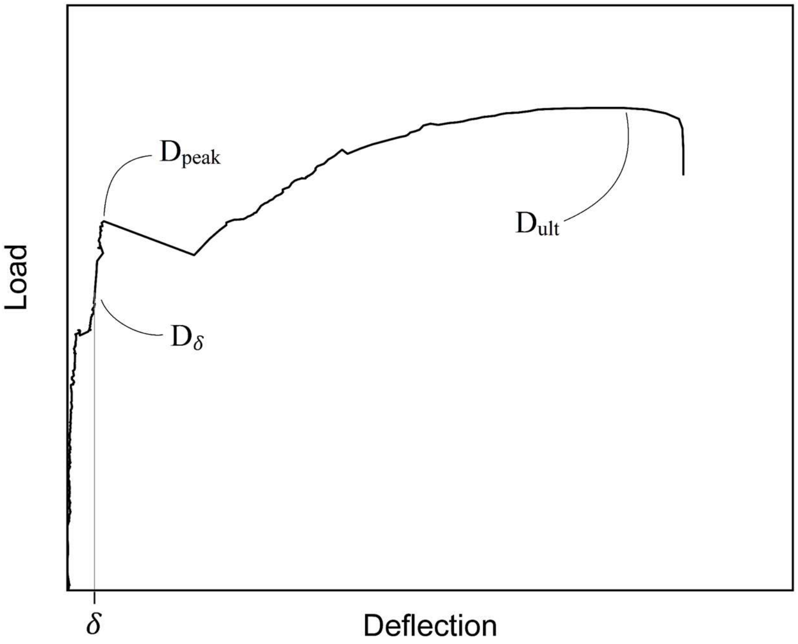

Figure 3.7: Typical RCP load-deflection profile labelled with D-load positions.

3.3 Experimental Results

3.3.1 Failure Mechanisms

(a) (b) (c)

Figure 3.8: Flexural (a), diagonal tension (b), and radial tension (c) crack patterns.

Three distinct failure mechanisms were observed during testing. **Figure 3.8** (a) shows flexural failure, which occurred in smaller diameter single-cage pipes and is characterized by single longitudinal cracks forming along the pipe invert and obvert. As the cracks propagated, concrete crushing occurred on the inside face of the pipe spring-lines, indicating the formation of plastic hinges at the invert, obvert, and spring-lines of the pipe. Flexural failures of pipe specimens were brittle and abrupt.

Figure 3.8 (b) shows diagonal tension (shear) failure, common in double and triple-cage pipes of diameter larger than 825-mm and is characterized by multiple invert and obvert cracks propagating diagonally from the bearing supports towards the inner face away from the centre-line. As failure continued, multiple parallel longitudinal cracks formed along both spring-lines. Pipe specimens undergoing diagonal tension failures exhibited steady and ductile failure, undergoing massive deflection without gaining significant strength.

Figure 3.8 (c) shows radial tension failure, common in RCP of high class and large diameter with no stirrups, which occurred in some large diameter pipes and is characterized by radial cracking around pipe rings. Radial tension failure is caused when high tensile forces in the steel reinforcement cause the inner circular cage to begin straightening. Radial tension can greatly disrupt the concrete structure and cause major spalling. Radial tension failures are severe, rapid, and destructive, with large portions of concrete separating and spalling from the structure. Delamination of concrete along the pipe length is observed at either the 5 o'clock or 7 o'clock positions; and 11 o'clock or 1 o'clock positions. In circular structures subjected to high load, radial tensions stresses can significantly reduce diagonal tension strength (Heger, 1963). There is some difficulty in capturing ultimate failures purely caused by radial tension, as radial tension stresses often lead to a weaker section, which then fails by diagonal tension.

During testing, all pipes initially formed a hairline (first) crack either along the invert or the obvert. In most cases, the invert crack formed first due to the added stresses imposed by the own weight of the pipe. As increased loading led to tension developing in the steel reinforcement, mid and larger sized pipes begun forming multiple hairline cracks, especially along the invert. Smaller pipes failing by flexure did not form these secondary hairline cracks, due to the reinforcing cage being positioned closer to the neutral axis of the pipe wall. Cracks also begun to form at the spring-lines. As with invert and obvert cracks, pipes failing by flexure generally form only one crack on each spring-line, while larger pipes form several spring-line cracks. This is usually when the 0.3-mm crack is observed at the invert or obvert. The 0.3-mm crack opened very suddenly in single-cage pipes; the operators often called $D_{0.3}$-load by visual inspection without needing to gauge the sudden crack due to its large size. Double and triple-cage pipes experienced a more gradual 0.3-mm crack formation than their single-caged counterparts. As loading continued, diagonal and radial tension crack patterns begun to form and led to eventual collapse of the pipe and ultimate load being was reached.

3.3.2 Three-Edge Bearing Test Results

Tables 3.4 to **3.6** present the results obtained through the existing TEBT method prescribed in CSA A257. $D_{0.3}$-load was calculated for all pipe specimens as per the current standard. D_{ult} was determined based on the maximum load resisted by the pipe specimen captured through the data-logging system. Based on $D_{0.3}$ and D_{ult}, the equivalent class was determined for each specimen. For some single-cage pipes, specifically specimens 450 through 600 and two 825 65D specimens, the operator was unable to capture the hairline crack. For the remaining 825 65D specimens, the percent difference between first-crack and $D_{0.3}$-load was only 0.65%, indicating $D_{0.3}$-load was reached almost immediately following formation of the first-crack for single-cage pipes.

Table 3.4: Single-cage TEBT results

Pipe	First-crack (N/m/mm)	$D_{0.3}$ (N/m/mm)	D_{ult} (N/m/mm)	$D_{ult}/D_{0.3}$ (%)	Eq. Class (N/m/mm)
450-140-1	-	227.9	373.6	164	228
525-140-1	-	187.6	261.7	139	188
525-140-2	-	214.5	259.9	121	208
600-140-1	-	166.2	299.6	180	166
600-140-2	-	195.1	226.8	116	181
675-140-1	132.2	161.5	233.5	145	162
675-140-2	127.4	147.7	215.6	146	148
750-100-1	101.2	134.6	360.4	268	129
750-100-2	105.0	123.8	201.3	163	124
825-065-1	121.4	122.2	134.0	110	89
825-065-2	-	134.8	137.8	102	92
825-065-3	-	128.3	143.7	112	96
825-100-1	99.8	126.7	193.1	152	127
825-100-2	56.8	106.7	185.2	174	107

Table 3.5: Double-cage TEBT results

Pipe	First-crack (N/m/mm)	$D_{0.3}$ (N/m/mm)	D_{ult} (N/m/mm)	$D_{ult}/D_{0.3}$ (%)	Eq. Class (N/m/mm)
825-140-1	120.4	149.3	238.4	160	149
900-140-1	100.9	150.3	242.4	161	150
900-140-2	100.9	153.0	250	163	153
975-100-1	93.2	108.1	165.4	153	108
975-140-1	103.1	164.0	235.1	143	164
1050-100-1	72.7	114.2	161.2	141	114
1050-140-1	83.8	163.4	204.7	125	163
1200-065-1	60.2	71.7	146.2	204	72
1200-065-2	35.0	73.7	132.7	180	74
1200-065-3	60.2	89.5	139.8	156	90
1200-100-1	65.3	114.7	167	146	111
1200-140-1	80.4	163.2	195.9	120	158
1200-140-2	99.2	164.8	196	119	157
1950-100-1	83.4	128.6	128.6	100	86
1950-100-2	84.5	124.2	125.2	101	84

Table 3.6: Triple-cage TEBT results

Pipe	First-crack (N/m/mm)	$D_{0.3}$ (N/m/mm)	D_{ult} (N/m/mm)	$D_{ult}/D_{0.3}$ (%)	Eq. Class (N/m/mm)
1800-100-1	65.9	123.8	156.7	127	105
1800-140-1	83.7	159.5	182.6	114	146
1800-140-2	80.7	153.0	165.6	108	133
1800-140-3	89.7	158.1	184.5	117	148
2100-100-A1	109.8	157.1	162.2	103	108
2100-100-B1	55.8	133.1	166.8	125	111
2100-100-B2	41.1	116.8	154.9	133	103
2250-140-1	95.3	174.0	175.6	101	141
2250-140-2	89.9	153.9	175.6	114	141
2250-140-3	92.0	163.1	181.7	111	145
2100-140-1(S)	62.2	176.3	218.1	124	175
2400-140-1(S)	62.6	151.2	188.9	125	151
2400-140-2(S)	55.6	164.6	193.5	118	155
2400-140-3(S)	60.3	159.5	196.2	123	157

3.3.3 Load-Deflection Results

Figure 3.9 presents the load-deflection plots for all tested specimens separated by the corresponding cage configuration. All load-deflection plots presented have been normalized through dividing each specimen's load by its corresponding $D_{0.3}$-load. Thus, the value of "1" on the vertical axis represents the 0.3-mm crack observation for all specimens. Deflection has been normalized through dividing each specimen's deflection by its corresponding longitudinal length and internal diameter. Observation reveals consistent load-deflection behavior amongst specimens of the same cage configuration.

Figure 3.10 presents characteristic crack and damage patterns observed during experiments. Single-cage RCP specimens usually underwent brittle failure and formed single cracks at the invert, obvert, and springline locations. Alternatively, double and triple-cage RCP specimens formed multiple cracks at the invert, obvert, and springlines, demonstrating higher ductility than their single-cage counterparts. A detailed discussion of these results is presented in the following subsections, with each cage configuration studied separately.

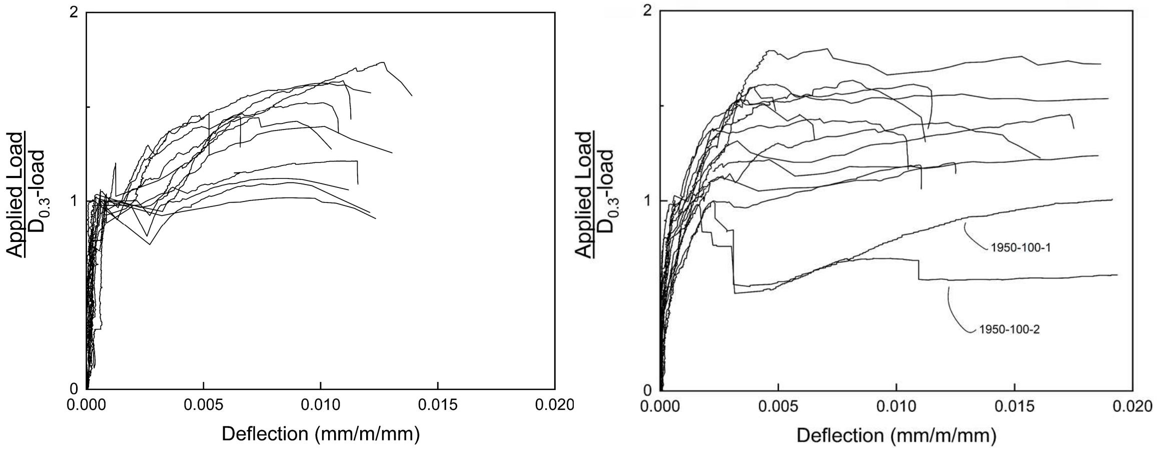

(a) Single-cage (b) Double-cage

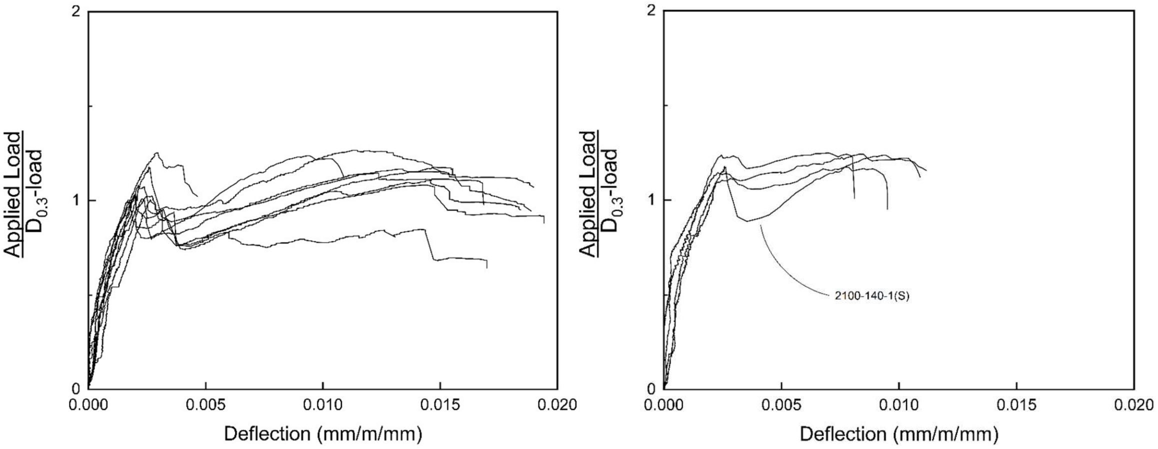

(c) Triple-cage (d) Triple-cage (stirrups)

Figure 3.9: Load-Deflection profiles of RCP specimens normalized by $D_{0.3}$-load.

(a) Evidence of reinforcing steel yielding in single-cage specimen tests.

1200-mm RCP showing multiple cracks at invert and spring-line during TEBT.

(c) Typical cracking features of triple-cage RCP undergoing TEBT.

Figure 3.10: Crack patterns and damage shown by RCP specimens during TEBT.

3.3.3.1 Single-Cage RCP

All tested single-cage pipes failed by flexure. Yielding of the steel rebar was visible through the cracks in some cases, as shown in **Fig. 3.10** (a). Single cracks formed along the inside face of the pipe invert and obvert, and along the outside face of the pipe spring-lines during testing. Concrete ring compression failure was observed at the inner face of the spring-lines (**Fig. 3.8**, a). The load-deflection behaviour of tested single-cage RCP is presented in **Fig. 3.9** (a). Before observation of the 0.3-mm crack, specimens experienced linear load-deflection behaviour. Following observation of the $D_{0.3}$-load, a significant loss in strength was evidenced by a drop in the load-deflection curve. This drop signals the end of the specimen's linear-elastic behaviour. This feature occurred in all single-cage specimens, showing a consistent pattern across pipe diameters. This behaviour was corroborated by single-cage load-deflection results presented in (Abolmaali *et al.*, 2012; Mohamed *et al.*, 2014; Silva *et al.*, 2018). All single-cage pipe specimens surpassed their maximum linear-elastic load in the plastic deformation phase, apart from one 825-mm 65D specimen, which did not regain full capacity in the plastic phase.

3.3.3.2 Double-Cage RCP

The predominant failure mode for double-cage specimens was diagonal tension (shear) failure, with radial tension occurring in few cases. **Figure 3.10** (b) shows typical cracks observed during testing of double-cage specimens. Unlike single-cage specimens, double-cage specimens showed multiple parallel longitudinal cracks at both spring-lines. Multiple cracks also formed along the invert and obvert during testing. This is attributed to the steel reinforcement being more favorably positioned within the tension block of the pipe wall for double-cage specimens compared to their single-cage counterparts. Since initial crack depth was controlled by the depth of reinforcing steel, multiple smaller cracks formed on the tension faces instead of a single major crack as observed in single-cage specimens.

The load-deflection behavior of tested double-cage RCP is presented in **Fig. 3.9** (b). The two 1950-mm specimens were marked separately due to their distinct size and behavior. When compared to single-cage RCP, double-cage RCP experienced much more gradual change in stiffness when transitioning from linear-elastic to plastic behavior. Double-cage load-deflection profiles did not feature significant drop in strength following $D_{0.3}$-load. However, the two 1950-mm outlier specimens experienced large loss in capacity following critical crack formation; load capacity for the 1950-100-1 and 1950-100-2 fell to 54.9% and 53.5%, respectively.

3.3.3.3 Triple-Cage RCP (without stirrups)

Like double-cage specimens, most triple-cage specimens failed by diagonal tension, with some cases of radial tension. The specimens also formed multiple longitudinal cracks along the obvert, invert, and both spring-lines. However, triple-cage specimens featured more cracks along the invert and spring-lines than their double-cage counterparts. **Figure 3.10** (c) presents typical cracking patterns observed in triple-cage specimens. The need to monitor multiple cracks over a large concrete area presented a challenge when determining $D_{0.3}$-load; the 0.3-mm crack location varied among the invert or obvert of the bell or spigot ends, with each location presenting several cracks, which must be gauged. Load-deflection profiles for triple-cage specimens are shown in **Fig. 3.9** (c). As with single-cage specimens, triple-cage specimens experienced a loss in strength following $D_{0.3}$-load, with most pipes regaining strength and surpassing their $D_{0.3}$-load. While $D_{0.3}$ was followed by a sudden drop in load readings for single-cage specimens, triple-cage specimens experienced a more gradual loss of strength before recovering in the plastic phase.

3.3.3.4 Triple-Cage RCP (with stirrups)

Triple-cage specimens equipped with stirrups did not show signs of radial tension behavior. The stirrups effectively distributed tension between the inner and outer reinforcing cages, increasing the radial tension capacity. All specimens failed by diagonal tension, and failure was more ductile than that of triple-cage specimens without stirrups. A greater number of cracks formed on specimens with stirrups compared to specimens without stirrups. Load-deflection profiles for triple-cage with stirrup specimens are shown in **Fig. 3.9** (d). The load capacity drops following $D_{0.3}$ were not as pronounced in triple-cage specimens with stirrups yet were still noticeable in the load-deflection profiles. This indicates that transition from elastic to plastic behavior was more gradual in specimens containing stirrups than in their no-stirrup counterparts. The stirrups allowed for efficient transfer of tensile stresses between the steel cages, greatly reducing radial tension action on the inner cage. However, specimen 2100-140-1 (S) experienced large load capacity drop following peak elastic load. This may be attributed to the lower quantity of stirrups used in the 2100-mm specimen as opposed to the 2400-mm specimens (245-mm^2/m and 382-mm^2/m, respectively), however further research is necessary to investigate the effect of stirrup reinforcement in triple-cage RCP.

3.4 Discussion

3.4.1 Ratio of D_{ult}:$D_{0.3}$

Figure 3.11 (a) shows the ratio of D_{ult} to $D_{0.3}$ for single-cage specimens, arranged by their intended design class then diameter. The average ratio for single-cage specimens was 1.49 with a relative standard-deviation (*RSD*) of 27.2%. The lack of consistency in post-crack capacity for single-cage specimens was indicated by high *RSD*. This inconsistency is expected, as load-deflection profiles for single-cage specimens reveal that the ultimate load occurred in the plastic phase. The single steel cage was positioned close to the neutral axis of the specimen cross-section, leading to limited tensile performance of steel pre-crack and sudden formation of large cracks. The 825-mm 65D specimens had D_{ult}:$D_{0.3}$ ratios close to 1, as the specimens did not gain significant strength in the plastic phase. D_{ult} for 825-065-2 occurred before the plastic phase of the load-deflection curve.

Figure 3.11 (b) shows the ratio of D_{ult} to $D_{0.3}$ for double-cage specimens. The 1950-mm diameter RCP specimens were placed furthest right to separate them due to the large difference in diameter between them and the next largest specimens. The ratio of D_{ult} to $D_{0.3}$ trended downwards with increasing specimen class and size. This trend indicates that specimens with a high size and class did not gain significant capacity past $D_{0.3}$-load. Those specimens were exposed to higher loads, making them more susceptible to radial tension action. Radial tension stresses can cause delamination of concrete, leading to debonding of steel rebar in critical areas and reducing the specimen's diagonal tension capacity. This greatly reduces post-crack performance, bringing the ultimate load closer to the crack load and reducing the D_{ult} to $D_{0.3}$ ratio. The average ratio for double-cage specimens was 1.45 with an *RSD* of 19.0%.

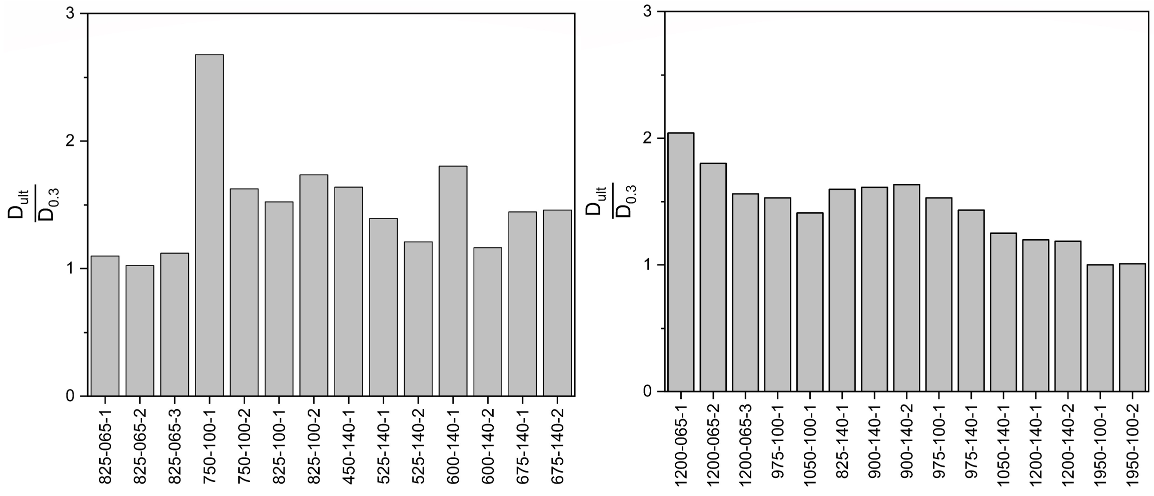

(a) Single-cage (b) Double-cage

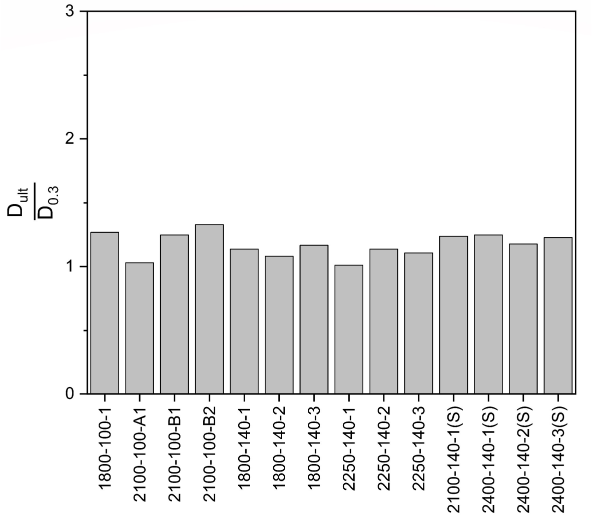

(c) Triple-cage

Figure 3.11: D_{ult} to $D_{0.3}$ ratios for each RCP specimen.

Figure 3.11 (c) shows D_{ult} to $D_{0.3}$ ratio for triple-cage specimens, arranged by intended design class then diameter. Specimens with stirrups were placed furthest right to distinguish them. The average ratio for triple-cage and triple-cage with stirrup specimens was 1.17, with an *RSD* of 7.6%. The low D_{ult} to $D_{0.3}$ ratio indicates that triple-cage specimens experienced limited load capacity gain following formation of the $D_{0.3}$ crack. The low *RSD* value indicates that this behaviour was consistent amongst triple-cage specimens. The limited gain in capacity was attributed to radial tension and diagonal tension forces causing concrete delamination, preventing the specimens from exploiting the full tensile capacity of the steel rebar. Another factor contributing to the low $D_{ult}:D_{0.3}$ ratio was the formation of multiple cracks. All tested triple-cage specimens formed a minimum of four parallel cracks across the invert. This allowed higher load to be applied before the critical 0.3-mm-wide crack was reached, as the total crack width was shared among numerous cracks.

3.4.2 Single-Cage RCP

The maximum linear-elastic load (D_{peak}) provides a distinct and consistent feature across load-deflection profiles for single-cage RCP. **Figure 13** compares the observed $D_{0.3}$-load values against the measured D_{peak}-load values. The high coefficient of determination (*R*-squared) shows very strong correlation between $D_{0.3}$ and D_{peak}, indicating the suitability of using D_{peak} to define a new test criterion without heavily disrupting current industry standards or the need for new costly testing equipment. Based on the trendline in **Fig. 13**, multiplying D_{peak} by a factor of roughly 0.97 would allow for a direct replacement of $D_{0.3}$. To provide an example, consider a hypothetical pipe with a D_{peak} of 120D and D_{ult} of 150D. Assuming the intended design class is 100D, the equivalent class would be taken as the lesser of 0.97 multiplied by D_{peak} (116.4D) or D_{ult} by a factor of safety 1.5 (100D). RCP specimens tested in Da Silva (2011) also exhibited clearly definable D_{peak}-loads, referred to in the Chapter as $F_{cracking}$.

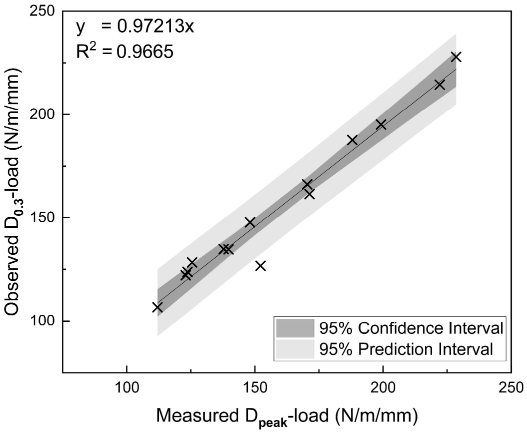

Figure 3.12: $D_{0.3}$-load vs D_{peak}-load for single-cage specimens.

3.4.3 Double-Cage RCP

While determining D_{peak} from single-cage load-deflection profiles is a straightforward process, double-cage load-deflection profiles do not show an easily identifiable capacity-driven trait. Consequently, defining a deflection-limit (δ-limit) criterion is a more rational approach to the double-cage TEBT. **Figure 3.13** shows plots of observed $D_{0.3}$-load versus measured load at different δ-limits (D_{δ}-load). For each case, D_{δ}-load is taken as the load at the corresponding δ-limit. δ-limit is given as a percentage of the inner diameter.

The trendlines for all charts in **Fig. 3.13** intercept through zero, and the corresponding slopes and R^2 coefficients are displayed. **Figure 3.14** (a) summarizes the slope and R^2 values. It can be observed that δ-limits lower than 0.20% show poor correlation between D_{δ} and $D_{0.3}$. This can be attributed to pre-crack deflections relying more on concrete tensile strength rather than the elastic behavior of reinforcing steel. Concrete tensile behavior can often be difficult to predict due to dependency of the tensile strength of concrete on numerous parameters such as curing conditions and age, whereas the tensile strength and elastic behavior of steel is more consistent. First-crack load and deflection values exhibited high variance across all specimens, with double-cage first-crack loads ranging from 35D to upwards of 100D. Deflection ranges where first-cracks occurred on double-cage specimens are shown in **Fig. 3.14** (b). Although initial hairline cracks occurred at varying deflections, all double-cage specimens cracked before 0.20% deflection. After the RCP cracked, the second moment-of-area of the concrete section decreased, thus decreasing the contribution of concrete and increasing the contribution of the reinforcing steel. After specimens had cracked, load-deflection behavior became more consistent, leading to higher R^2 correlation between $D_{0.3}$ and D_{δ} values. **Figure 3.14** (a) implies a deflection limit between 0.35% – 0.40% to be the optimal δ-limit criterion. This δ-limit would yield the highest correlation between $D_{0.3}$ and D_{δ} and the closest trendline slope to equality, thus remaining in agreement with current industry design benchmarks and standards. This δ-limit is also in agreement with the δ-limit of 0.4% reported in Figueiredo *et al.* (2012), although the specimens used were SFRCP.

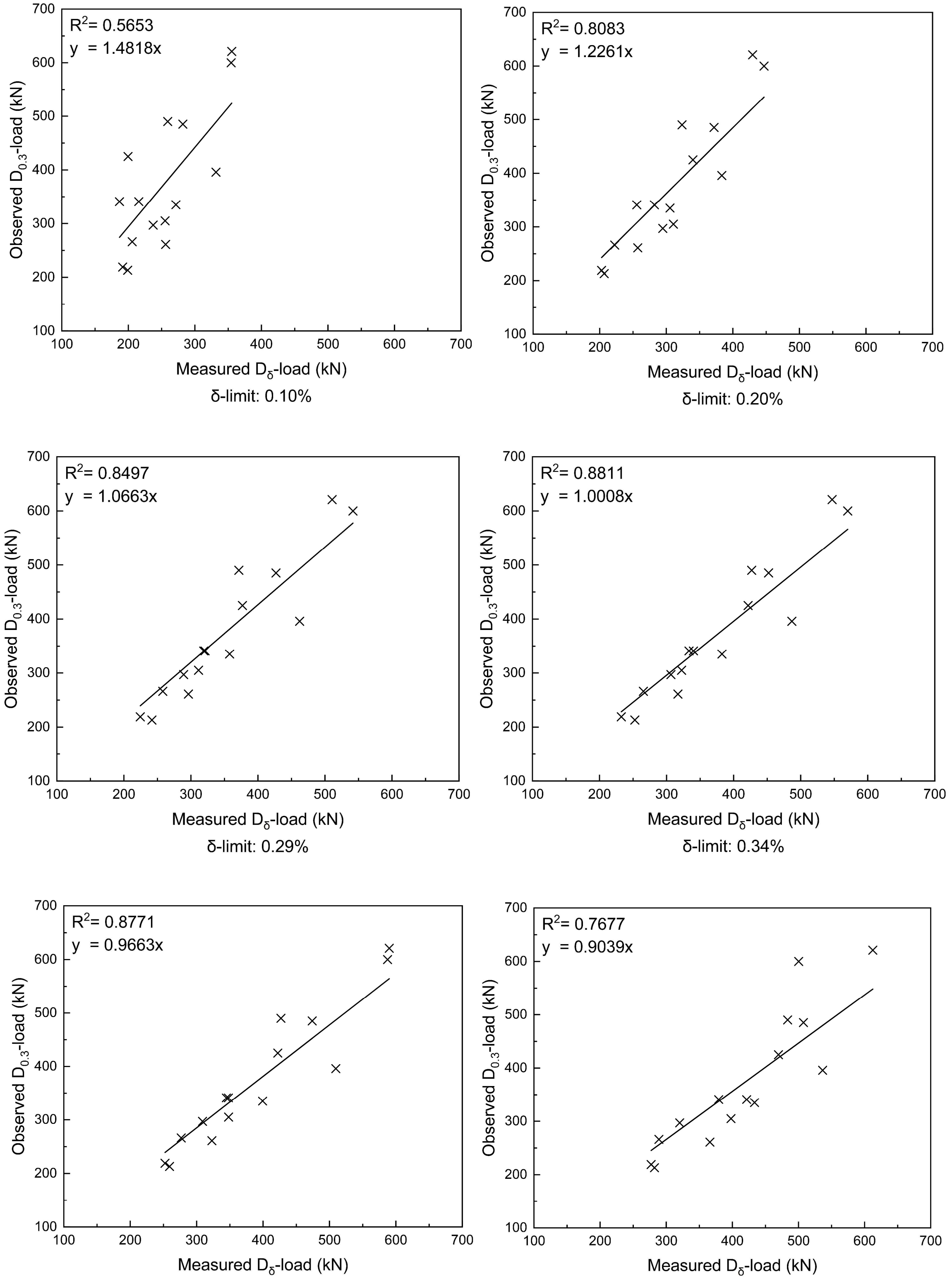

δ-limit: 0.10%

δ-limit: 0.20%

δ-limit: 0.29%

δ-limit: 0.34%

δ-limit: 0.39%

δ-limit: 0.49%

Figure 3.13: $D_{0.3}$ vs D_{δ} for double-cage RCP specimens.

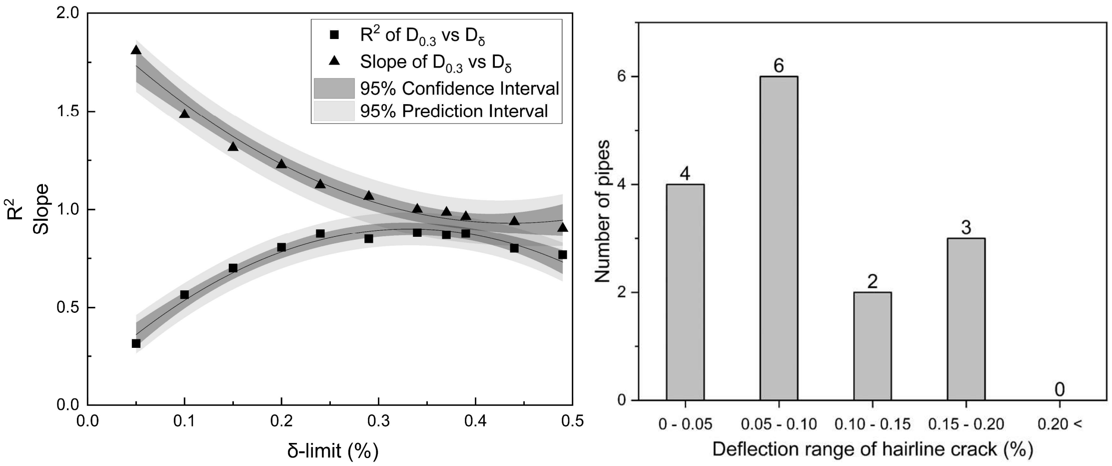

(a) (b)

Figure 3.14: (a) Slope and R^2-coefficients resulting from each δ-limit for double-cage specimens, and (b) number of double-cage RCP specimens to form first hairline crack at each deflection range.

3.4.4 Triple-Cage RCP

Triple-cage specimens were tested by two different operators, referred to here as Operator A and Operator B for ease-of-reference. Operator A had short-term experience running TEBTs, while Operator B was a quality control engineer with over 10-years of experience. Owing to the similar initial peak phenomenon present in single-cage pipe profiles, defining D_{peak} for triple-cage profiles is straightforward.

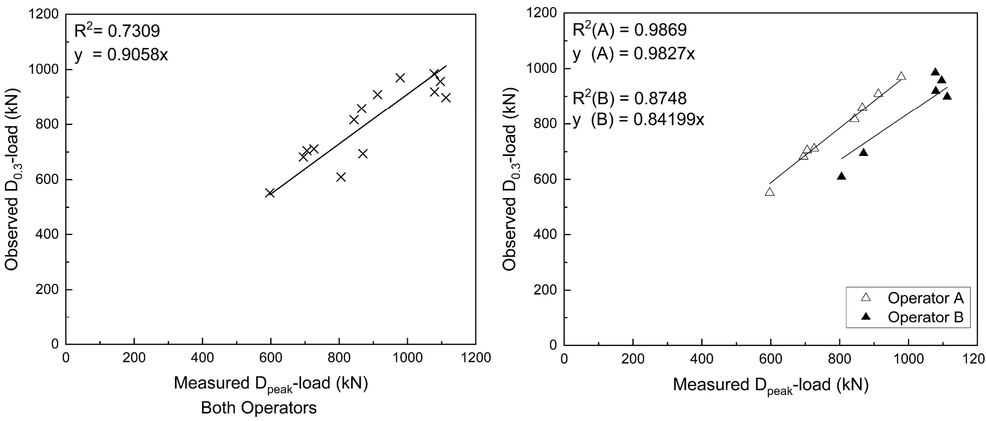

(a) (b)

Figure 3.15: $D_{0.3}$-load vs. D_{peak}-load comparison for triple-cage specimens.

Figure 3.15 compares the measured D_{peak} to the observed $D_{0.3}$ and indicates good R^2 correlation when separating datasets by operator (**Fig. 3.15**, b). When comparing all tested triple-cage specimens together, however, the R^2 coefficient becomes inadequate (**Fig. 3.15**, a). The results obtained by the more experienced Operator B were more conservative than those obtained by Operator A. The low R^2 value when comparing across operators shows another drawback of the current TEBT methods: comparing results across one operator's tests was appropriate but doing so across operators of different skill-levels became unreliable. This weakness in the current TEBT method can be remedied by applying a D_{peak}-load measurement for triple-cage pipes, replacing the manual 0.3-mm crack observation with a more consistent digital load measurement.

Alternatively, applying a δ-limit criterion and testing D_{δ}-load instead is worth considering. R^2 correlations of triple-cage $D_{0.3}$ versus D_{δ} for δ-limits between 0.05% – 0.68% were investigated. Sample plots are shown in **Fig. 3.16**. There was no correlation between the two D values at δ-limits lower than 0.20%. **Figure 19** summarizes these results and identifies that a δ-limit between 0.45% – 0.50% yields the highest correlation between the two D values, along with a trendline slope closest to equivalency. A δ-limit in the suggested range would provide D_{δ} values comparable to $D_{0.3}$, avoiding disturbance of current industry design practices.

The present data involving D_{peak} and D_{δ} for triple-cage pipes does not yield high R^2 correlation with $D_{0.3}$-load, indicating that neither modified D-load value can be used to confidently estimate $D_{0.3}$-load for triple-cage RCP. Furthermore, the low R^2 correlation between D_{peak} and $D_{0.3}$ indicates that formation of 0.3-mm crack-width in triple-cage RCP does not correspond to the specimen's true capacity. Basing serviceability criteria on D_{peak} rather than $D_{0.3}$ would benefit the TEBT by allowing industry to class pipes based on a rational capacity criterion, as opposed to an arbitrary crack observation-based criterion.

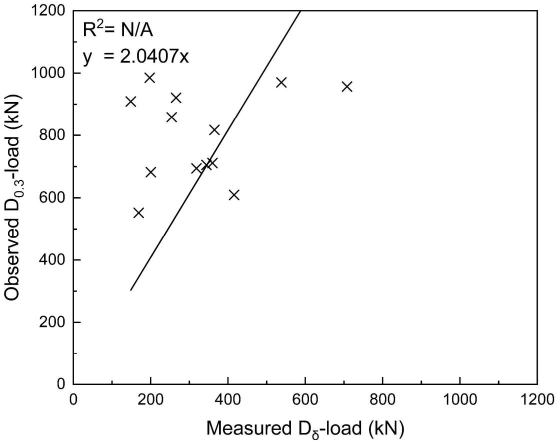

δ-limit: 0.10%

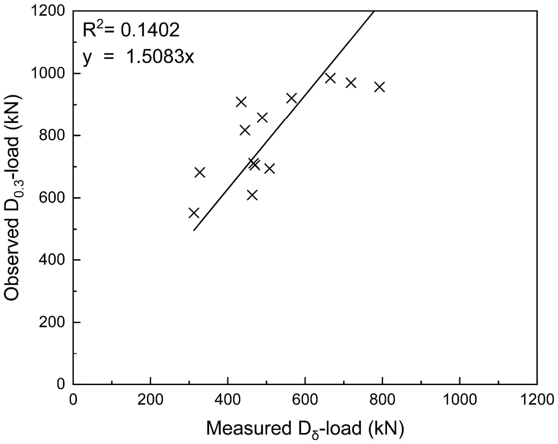

δ-limit: 0.20%

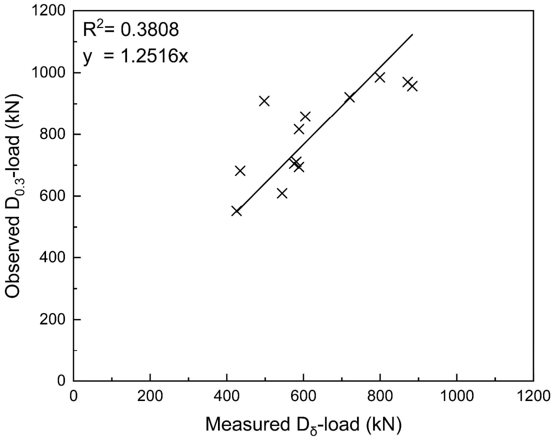

δ-limit: 0.29%

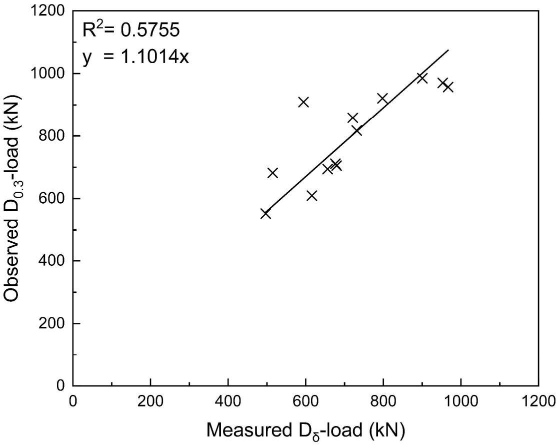

δ-limit: 0.39%

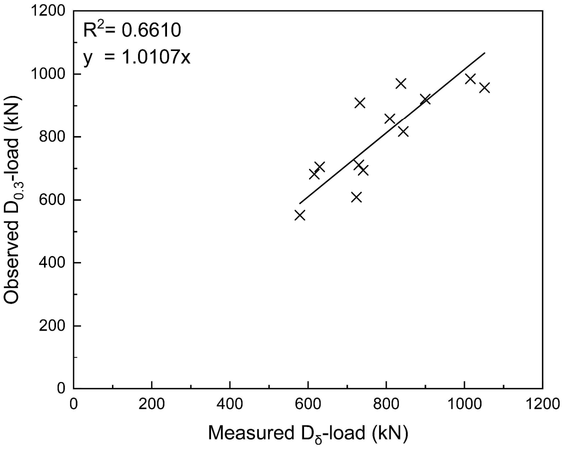

δ-limit: 0.49%

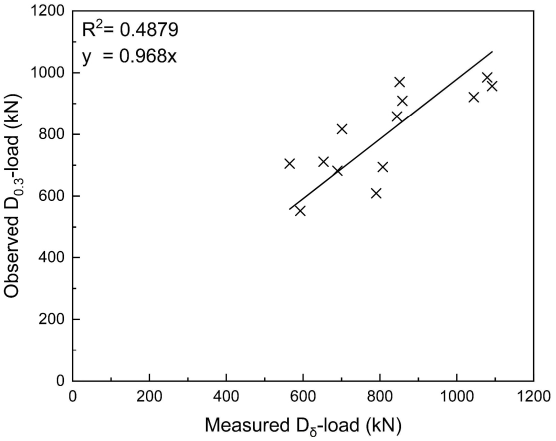

δ-limit: 0.59%

Figure 3.16: $D_{0.3}$ vs D_δ for triple-cage RCP specimens.

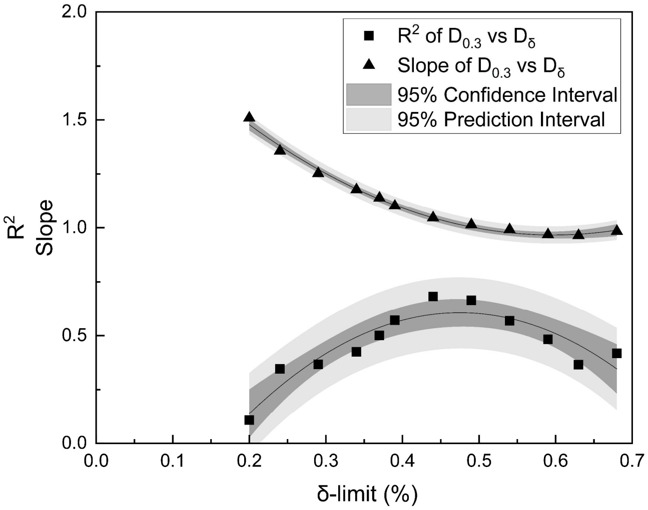

Figure 3.17: Slope and R-squared coefficients resulting from each δ-limit for triple-cage specimens.

3.5 Conclusions

This chapter studied the load-deflection behavior of full-scale RCP undergoing the TEBT across a wide range of pipe diameters and reinforcement configurations to assess the possibility of improving the century-old standard TEBT method by eliminating the operator sensitive crack-width observation requirement. RCP specimens were manufactured using the three traditional steel-reinforcement cage configurations. The load-deflection response during TEBT loading was measured for each specimen using LVDT sensors during the test. Based on the experimental results and analysis, the following conclusions can be drawn:

1. The 0.3-mm crack-width criterion, $D_{0.3}$, is a source of inaccuracy for the TEBT due to its reliance on operator skill and bias in determining the exact moment $D_{0.3}$ occurs. In larger diameter pipes, the operator must simultaneously monitor several crack-widths (**Fig. 3.18**) and be tall enough to reach and gauge the obvert cracks as well. Assessing RCP based on digital measurements of load-deflection data would greatly reduce the uncertainty currently associated with $D_{0.3}$ readings.

Figure 3.18: Operator monitoring multiple invert cracks over a large area to detect $D_{0.3}$ crack.

2. Load-deflection results revealed consistent and distinct behavior patterns during TEBT loading for each RCP steel cage configuration. Single-cage RCP tended to develop an initial linear-elastic peak-load before a sudden drop in the load-deflection relationship following crack formation. Conversely, double-cage RCP experienced gradual transition between linear-elastic and nonlinear-plastic load-deflection behaviors. On the other hand, triple-cage RCP formed similar peak-load concentration in the linear-elastic phase with a more gradual loss of load compared to single-cage specimens. Both single and triple-cage specimens tended to regain some strength in the plastic phase, however, not all specimens surpassed their linear-elastic maximum load.
3. The peak linear-elastic load, D_{peak}, as defined in this Chapter, can replace $D_{0.3}$ for single-cage RCP owing to the high correlation and proximity between the two values. The findings suggest that $D_{0.3}$ for single-cage RCP can be estimated as D_{peak} multiplied by a factor of 0.97.
4. Due to the lack of clearly identifiable points in double-cage RCP load-deflection patterns, the use of D_{peak} is not recommended for double-cage RCP. The deflection-controlled criterion, D_{δ}, has been defined in this research as the load corresponding to a certain deflection, δ, given as a percentage of the inside pipe diameter. Setting a δ-limit in the range of 0.35% – 0.40% for double-cage RCP yields D_{δ} values with high correlation and proximity to $D_{0.3}$ values.

5. $D_{0.3}$ loads assessed for triple-cage RCP had higher correlation with D_{peak} than with D_{δ} loads. As with single-cage RCP, using D_{peak} is recommended for triple-cage RCP considering the clear maximum linear-elastic peak load allowing for capacity-driven rather than crack-width governed criteria.
6. For triple-cage RCP, D_{peak} exhibited high correlation with $D_{0.3}$ when compared with pipes tested by the same operator. This reveals a key drawback of the current TEBT, which yields inconsistent results for data obtained by different operators. Using the modified serviceability D values proposed in this research would eliminate this inconsistency and inaccuracy of $D_{0.3}$ determination, by assessing pipe performance based on rational and indisputable capacity or deflection-controlled criteria.
7. Some single-cage and double-cage specimens were able to gain significant load capacity in the plastic phase, though high variance was observed. For single-cage specimens, D_{ult} was larger than $D_{0.3}$ by as much as 80% in some cases and as little as 2% in others. One specimen was even able to surpass $D_{0.3}$ by 168%. For most double-cage specimens, D_{ult} was between 20% and 80%. Triple-cage specimens only gained 17% in load capacity on average past $D_{0.3}$-load, however their behavior was much more consistent, as evidenced by a low standard deviation of 7.6%.

Producing and testing full-scale RCP for research purposes is a costly undertaking. However, the benefits industry and academia stand to gain by improving the TEBT outweigh the cost of investment. By adhering to clearly defined and indisputable testing criteria, TEBT results can be compared across different manufacturing facilities and research teams. By replacing the $D_{0.3}$ crack-width criterion, the modified serviceability D-loads, D_{peak} and D_{δ}, proposed in this chapter are promising alternatives for improving current TEBT standards.

3.6 References

Abolmaali, A., Mikhaylova, A., Wilson, A., & Lundy, J. (2012). Performance of Steel Fiber–Reinforced Concrete Pipes. *Transportation Research Record: Journal of the Transportation Research Board*, *2313*(1), 168–177. https://doi.org/10.3141/2313-18

ASTM A1064/A1064M-18a. (2018). *Specification for Carbon-Steel Wire and Welded Wire Reinforcement, Plain and Deformed, for Concrete*. ASTM International. https://doi.org/10.1520/A1064_A1064M-18A

ASTM C76. (2016). *Specification for Reinforced Concrete Culvert, Storm Drain, and Sewer Pipe*. ASTM International. https://doi.org/10.1520/C0076-16

ASTM C497. (2018). *Test Methods for Concrete Pipe, Manhole Sections, or Tile*. ASTM International. https://doi.org/10.1520/C0497-18

CSA A257. (2014). *Standards for Concrete Pipe and Manhole Sections*. CSA Group.

Figueiredo, A., de la Fuente, A., Molins, C., & Aguado, A. (2012). A New Approach on Crushing Strength Test for Fibre Reinforced Concrete Pipes. *8th RILEM International Symposium on Fibre Reinforced Concrete: Challenges and Opportunities (BEFIB2012)*, 1082–1095.

Heger, F. (1963). Structural Behavior of Circular Reinforced Concrete Pipe-Development of Theory. *ACI Journal Proceedings*, *60*(11). https://doi.org/10.14359/7905

Mohamed, N., Soliman, A. M., & Nehdi, M. L. (2014). Full-scale pipes using dry-cast steel fibre-reinforced concrete. *Construction and Building Materials*, *72*, 411–422. https://doi.org/10.1016/j.conbuildmat.2014.09.025

Silva, J. L. da, El Debs, M. K., & Kataoka, M. N. (2018). A comparative experimental investigation of reinforced-concrete pipes under three-edge-bearing test: Spigot and Pocket and Ogee Joint pipes. *Acta Scientiarum. Technology*, *40*(1), 30860. https://doi.org/10.4025/actascitechnol.v40i1.30860

Wong, L., & Nehdi, M. (2018). Critical Analysis of International Precast Concrete Pipe Standards. *Infrastructures*, *3*(3), 18. https://doi.org/10.3390/infrastructures3030018

Chapter 4

Numerical Modeling of Reinforced-Concrete Pipe with Single, Double and Triple-Cage Reinforcement

4.1 Introduction

Finite-element models (FEMs) for SFRCP undergoing the TEBT have been developed successfully by various researchers, such as (de la Fuente et al., 2012a, 2012b; Ferrado et al., 2016; Mohamed & Nehdi, 2016). However, only two FE models of conventional RCP were found in existing research: Tehrani (2016) and Kataoka et al. (2017). The model developed in Tehrani (2016) uses the FEM software ABAQUS and follows the concrete damaged plasticity model available in the software to model the nonlinear behaviour of concrete in tension and compression. Single and double-cage RCP configurations are considered across a range of diameters, although only three experimental validations are performed. The Kataoka et al. (2017) model instead uses FEM software DIANA and models concrete based on the total strain model and steel based on the Von Mises plasticity models. The study develops single-cage 800-mm and double-cage 1200-mm models. The numerical results in Kataoka et al. (2017) are calibrated based on a multitude of experimental results, however no parametric study is performed.

The study presented in this chapter advances the current state-of-the-art by developing three 825-mm and three 1200-mm ABAQUS models, each calibrated or validated using actual RCP specimen load-deflection results obtained in the previous chapter. Based on these validated models, 68 additional models are analyzed to provide an in-depth reinforcement-based parametric study. The aim of this chapter is to provide RCP industry with insight and knowledge into the effects of reinforcement area, yield, cover, and position on serviceability and ultimate loads of RCP specimens. Furthermore, a triple-cage RCP model is developed and validated using experimental results for future use in similar studies. At the time of writing, no other triple-cage model could be found in the existing literature.

Table 4.1 summarizes data of relevant RCP specimens from Chapter 3 modelled in this chapter.

Table 4.1: RCP specimen data used to build Chapter 4 numerical models

Diameter (mm)	**Class (N/m/mm)**	***Asi*** **(mm^2/m)**	***Aso*** **(mm^2/m)**	***Ase*** **(mm^2/m)**	**Wall (mm)**	**Specimens Tested**
825	65D	290	-	-	114	3
825	100D	484	-	-	114	2
825	140D	581	323	-	121	1
1200	65D	565	376	-	127	3
1200	100D	821	645	-	127	1
1200	140D	1548	645	-	127	2
1800	140D	1807	774	1290	178	3

4.2 Finite-Element Model Development

4.2.1 Constitutive Material Modelling

Two constitutive material models for analyzing concrete are available in ABAQUS/Standard: concrete smeared-cracking (CSC) and concrete damaged plasticity (CDP) models (Hamedani & Esfahani, 2012, p. 25). CSC is limited to modelling reinforced and unreinforced concrete in static problems with monotonic loading. The CDP approach allows for the modelling of reinforced and unreinforced concrete exposed to monotonic, cyclic, or dynamic loading scenarios by considering the material's stiffness reduction and recovery (Hamedani & Esfahani, 2012).

The CDP algorithms derived by Alfarah *et al.* (Alfarah et al., 2017) were used to develop the inelastic stress-strain concrete response in compression and tension. A notable benefit of these algorithms is their reliance on just two main input parameters: compressive strength of concrete (f'_c) and finite-element mesh size (l_{eq}). Despite the algorithms yielding highly mesh-sensitive inputs, the outputs of models based on these algorithms are insensitive to mesh size (Alfarah et al., 2017, p. 80).

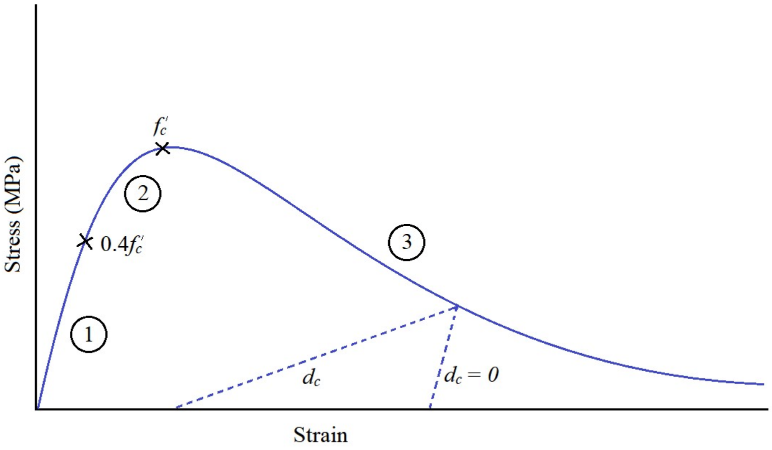

Figure 4.1: Compressive stress-strain curve used to model concrete in concrete-damaged plasticity models (After Alfarah *et al.,* 2017).

Figure 4.1 presents a generic compressive stress-strain curve used to represent the concrete element in CDP. The stress-strain curve is divided into three segments based on the type of behaviour and corresponding algorithm. In segment 1, the stress-strain response is assumed to be linear-elastic until stress in the concrete reaches $0.4f'_c$. Segment 2 is quadratic, and stress continues ascending until reaching the compressive strength of concrete (f'_c) (Alfarah *et al.,* 2017). Beyond this point, continued strain causes stress in the concrete to descend in segment 3. Behaviour in this final segment is described by nonlinear equations. The dashed lines represent the unloading response of the concrete, depending on the value of the damage parameter d_c. This parameter is a function of stress, maximum stress, strain, maximum strain, and rigidity. Tensile stress-strain behaviour is described by an ascending linear-elastic segment until tensile strength is reached, followed by a sharp inelastic descent. The complete algorithms and equations followed to develop the stress-strain responses in this paper can be found in (Alfarah *et al.,* 2017).

Figure 4.2 shows the compressive and tensile stress-strain responses used to model the concrete material. The concrete compressive strength was set at 60 MPa based on experimental results. During early calibration, the numerical models were found to be sensitive to the tension stiffening parameter of the concrete model. Different RCP specimens are expected to have different tensile strengths depending on concrete mixture design, curing environment and age.

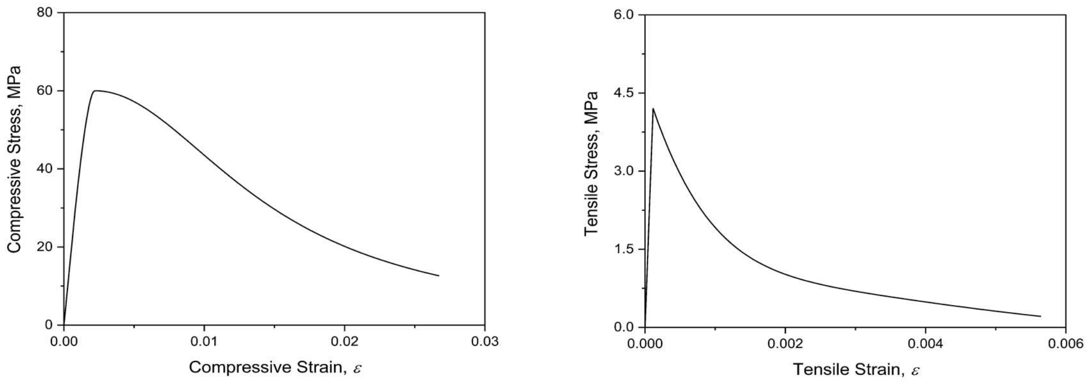

Figure 4.2: (a) Compressive and (b) tensile stress-strain used to model concrete material, developed using algorithms derived in Alfarah *et al.* (2017).

Five principal parameters must be defined for the CDP model in ABAQUS: dilation angle, viscosity, eccentricity, f_{b0}/f_{c0}, and K_C (*Abaqus Analysis User's Guide (6.13)*, 2013). Dilation angle (ψ) affects volumetric strain and ranges from 0˚ for brittle behaviour to a maximum of 56.3˚ for ductile behavior, with the range $30^\circ \leq \psi \leq 40^\circ$ recommended for concrete (Hamedani & Esfahani, 2012, p. 33). Viscosity (μ) can have large effect on the material behavior by greatly affecting its crack and damage pattern. Higher values of μ increase the damage zone (Michał & Andrzej, 2015), while lower values may cause convergence issues in the ABAQUS solver (Tehrani, 2016). For eccentricity (ϵ), f_{b0}/f_{c0}, and K_C, the ABAQUS default values of $\epsilon = 0.1$, $f_{b0}/f_{c0} = 1.16$, and $K_C = 2/3$ were used in all CDP models surveyed (Alfarah et al., 2017; Demir et al., 2016; Ferrado et al., 2016; Hamedani & Esfahani, 2012; Kmiecik & Kamiński, 2011; Michał & Andrzej, 2015; Mohamed & Nehdi, 2016; Tehrani, 2016). **Table 4.1** summarizes values selected by different researchers for modelling concrete pipe, while **Table 4.2** presents the CDP parameters used in this chapter.

Table 4.2: Summary of CDP model parameters used to model concrete pipe in literature

Research	ψ	μ	ϵ	f_{bo}/f_{co}	K_c
Tehrani (2016, p. 53)	30-40	0.0001	0.1	1.16	0.667
Mohamed et al. (2016, p. 198)	36.31	0	0.1	1.16	0.67
Ferrado et al. (2016, p. 2331)	36.51	0	0.1	1.16	0.67
Riahi (2016, p. 73)	38	1×10^{-7}	0.1	1.16	0.667

Table 4.3: CDP parameter values used to model RCP in this chapter

Parameter	**Value**
Dilation angle (ψ)	36
Viscosity parameter (μ)	0.0001
Eccentricity (ϵ)	0.1
f_{bo}/f_{co}	1.16
K_c	0.667

Based on the high commonality in CDP input values in the open literature, values for eccentricity, f_{bo}/f_{co}, and K_c were set equal to common practice. Dilatancy angle was set as $\psi = 36^\circ$ based on a previous study conducted at the manufacturing plant by Mohamed *et al.* (2016). Finally, the viscosity parameter was set as $\mu = 0.0001$ due to convergence issues in the ABAQUS solver and based on recommendations in (Michał & Andrzej, 2015). The same value has been used successfully in existing reinforced-concrete models (Demir et al., 2016; Tehrani, 2016).

4.2.2 Model Components

In general, concrete reinforcing is modelled using either the discrete or smeared concrete element approach in FEM (Dahmani & Khennane, 2010). The discrete method uses truss or bar elements to represent the reinforcing steel, and solid or shell elements to represent the concrete. The truss elements are then embedded and constrained to the solid element nodes. In the smeared concrete element approach, the concrete and reinforcement are represented in the same element with the effects of reinforcement averaged within the element (Dahmani & Khennane, 2010). While the smeared concrete element approach is useful when considering the global response of a structure, the discrete approach allows for stresses within specific steel or concrete elements to be considered. As such, the discrete approach was selected to model the reinforcement in this study.

The FEMs developed in this chapter are composed of three main components: concrete pipe, reinforcing steel cage, and bearing strips. Because the bearing strips were only included to mimic the TEBT load distribution, they are assumed to be rigid solid elements. The helical steel cage was approximated as circular rings spaced at a distance equal to the pitch of the corresponding specimen reinforcement. This approximation was found appropriate due to similar total length of steel (less than 1% difference), as well as similar angular orientation of the wires (less than 1° difference) between the helical and circular shapes. The cage was modelled using 2D truss elements with mesh size of l_{eq} = 25-mm. The concrete pipe was modelled as a solid element and meshed into cubes of l_{eq} = 25-mm. Since the algorithms developed in Alfarah *et al.* (2017) yield mesh-insensitive outputs, mesh size was decided based on previous concrete pipe studies, which found similar mesh size of 20-mm to be appropriate (Mohamed & Nehdi, 2016, p. 197; Tehrani, 2016, p. 62).

The concrete pipe structure and rigid bearings were modelled using ABAQUS C38DR hexahedral (8-node) elements in 3D space. The steel-cage was modelled using ABAQUS T3D2 (2-node) truss elements, which were first sketched as a single 2D ring then repeated along the pipe in 3D space. Total element counts were 41,008 for the 825-mm single cage model, 94,009 for the 1200-mm double-cage model, and 207,024 elements for the 1800-mm triple-cage model.

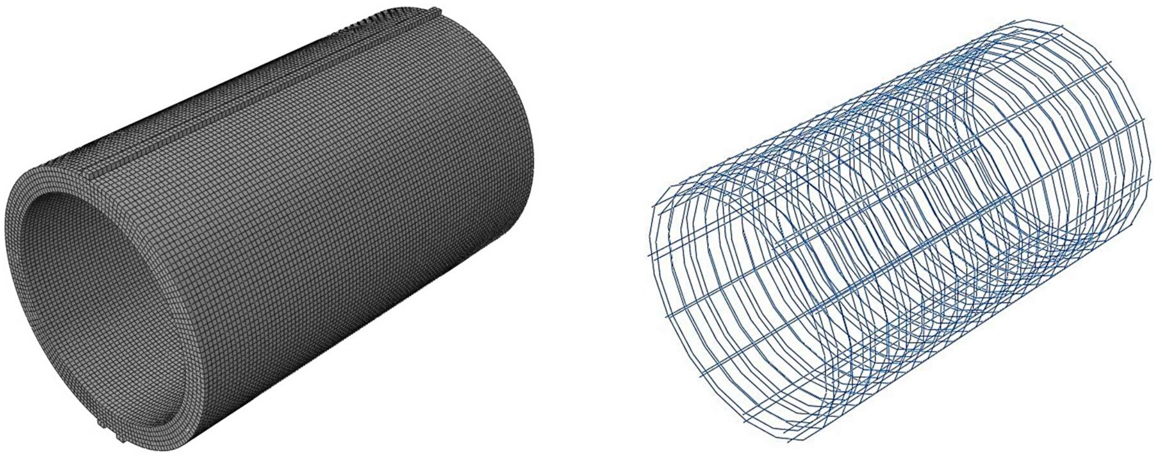

(a) (b)

Figure 4.3: Example of 1200-mm double-cage (a) concrete material solid mesh and (b) steel wire truss used in the FEM.

Figure 4.3 provides an example of the solid and truss element meshes used in FEM. The wire assembly was embedded within the concrete structure using an embedded truss-in-solid constraint between the wire and concrete solid. This constrains the translational degrees of freedom of the truss element nodes to those of the solid element nodes through geometric relationships determined by the ABAQUS program. Three tie constraints were also assigned between each bearing surface and its corresponding concrete contact surface. These constraints tie the movement of the adjacent concrete and bearing surfaces together. The two lower bearings were fully restrained along their lower surface. Loading was then simulated by applying a downward vertical deflection on the upper bearing strip. ABAQUS works on iteratively solving the finite-element equation in small increments of displacement and is then able to generate load-data at each increment. The sum of vertical reaction forces at each node along the lower bearings corresponds to the total load applied on the system. It was extracted from the model to form the load-deflection plots.

4.3 Model Calibration and Validation

Numerical load-deflection output is not expected to agree with the experimental load-deflection output until the models are calibrated. Load-deflection plots in this study present applied load in terms of D-load (N/m/mm), and deflection as a percentage of pipe diameter, δ (see **Fig. 3.6** in Chapter 3). The accuracy of the single-cage models was assessed at two points: D_{ult} and D_{peak}. Because double-cage specimens did not exhibit clear D_{peak}-loads, the load at a specific deflection point (D_{δ}) was used to assess error. Findings in Chapter 3 revealed that the load at a deflection equal to 0.36% of the diameter ($D_{\delta = 0.36\%}$) was a significant indicator of the RCP service capacity. Additionally, D_{peak} and $D_{\delta=0.36\%}$ showed good correlation and agreement with the 0.3-mm crack criterion, $D_{0.3}$.

4.3.1 Calibration of Finite-Element Models

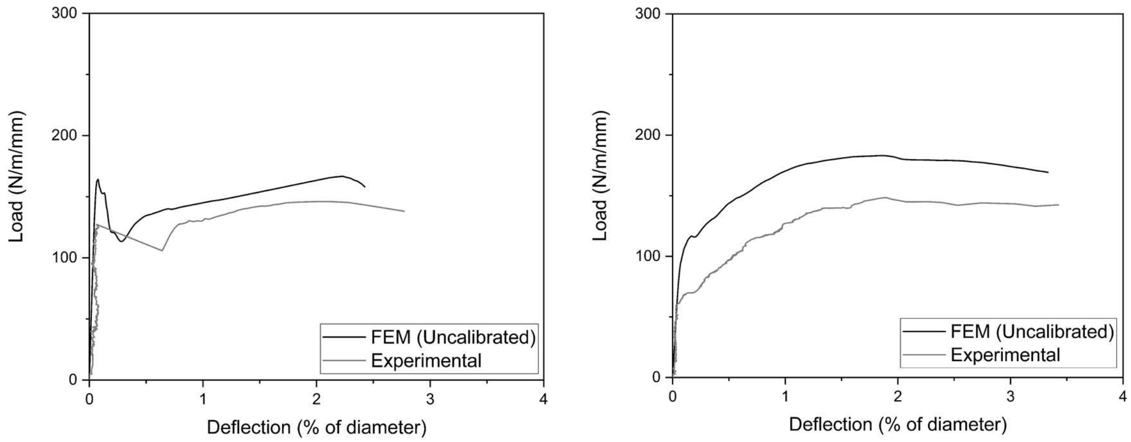

825-mm 65D FEM

1200-mm 65D FEM

Figure 4.4: Load-deflection response of uncalibrated 825-mm 65D (single-cage) and 1200-mm 65D (double-cage) FE models.

Figure 4.4 shows the load-deflection results from the 825-mm 65D and 1200-mm 65D numerical model RCPs compared to their experimental counterparts. Both models showed good agreement with the experimental results, indicating the assumption of Young's modulus = 39 GPa for the concrete material was appropriate. The single-cage results revealed that the model overestimates D_{peak} by 29.0% and D_{ult} by 14.1%, while the double-cage model overestimated $D_{\delta = 0.36\%}$ by 51.3% and D_{ult} by 23.3%. The high percent error for D_{peak} indicates that the estimated tensile strength of concrete was a critical source of error, as D_{peak} is related to the cracking load. As such, the tension stiffening parameter must be calibrated. Tensile strength of the concrete was not measured during the experimental tests and was instead based on standard equations which estimate tensile strength as a function of compressive strength (Alfarah et al., 2017, p. 76). However, the tensile strength of concrete is usually highly variable and can be affected by the testing method, aggregate type, and the environmental conditions, even more so than concrete compressive strength (Comite Euro-International Du Beton, 1993).

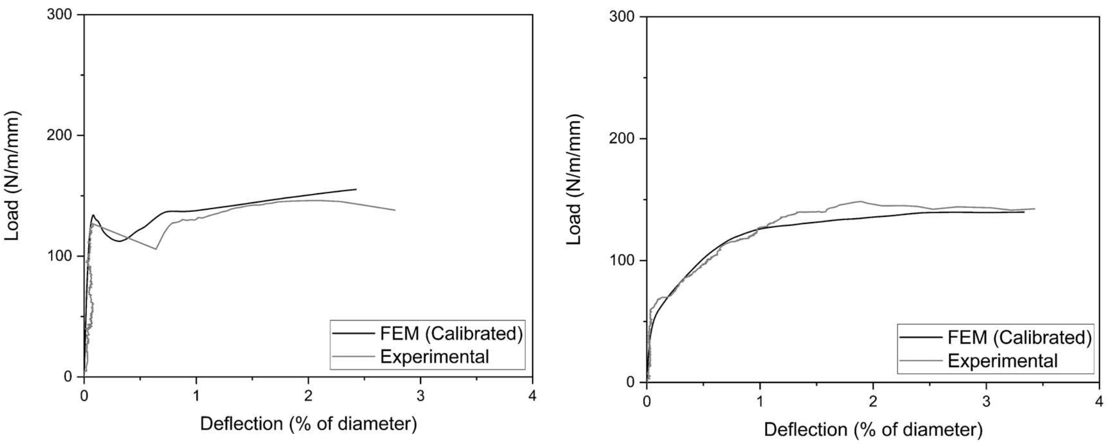

825-mm 65D FEM

1200-mm 65D FEM

Figure 4.5: Load-deflection response of 825-mm 65D (single-cage) and 1200-mm 65D (double-cage) FE models after calibration of tension stiffening parameters.

Figures 4.5 illustrates the load-deflection results from the same numerical models after calibration of the tension stiffening parameter. The latter was found to cause significant changes in the models' behavior. After calibration, single-cage model errors decreased to only 5.3% for D_{peak} and 6.3% for D_{ult}, while the double-cage model errors decreased to 2.7% for $D_{\delta = 0.36\%}$ and 5.9% for D_{ult}.

4.3.2 Validation of Finite-Element Models

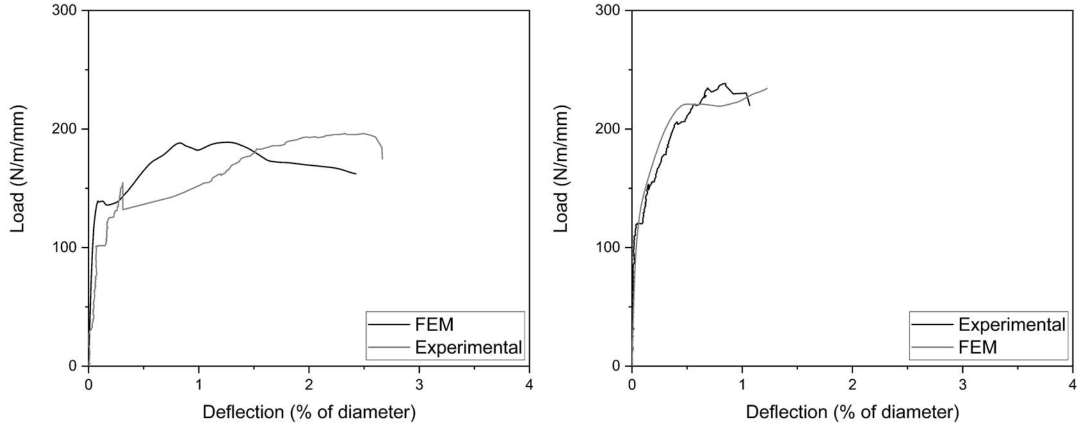

(a) 825-mm 100D (single-cage) (b) 825-mm 140D (double-cage)

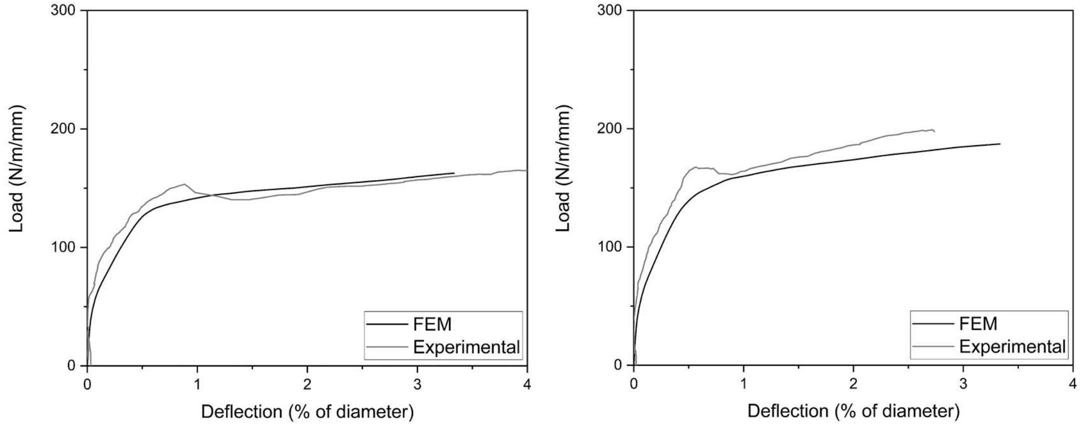

(c) 1200-mm 100D (double-cage) (d) 1200-mm 140D (double-cage)

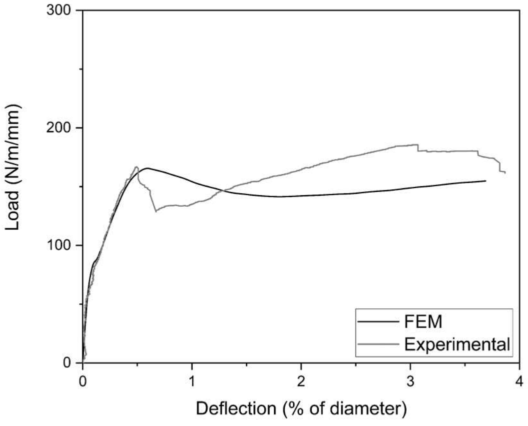

(e) 1800-mm 140D (triple-cage)

Figure 4.6: Load-deflection results of validation FE models.

The tension stiffening calibration of the FE numerical models was validated based on experimental results of RCP with the same diameter size, but different pipe classes. The single-cage calibration model was validated based on results from 825-mm 100D RCP, while the double-cage calibration was validated based on results obtained from 825-mm 140D, 1200-mm 100D, and 1200-mm 140D RCP specimens. **Figure 4.6** shows the load-deflection results obtained from the validation models compared to their experimental counterparts. Overall, good model accuracy can be observed. The error in the 825-mm 100D single-cage model (**Fig. 4.6,** a) was 9.9% based on D_{peak} and 3.7% based on D_{ult}. Error in the 825-mm 140D double-cage model (**Fig. 4.6,** b) was 6.7% for $D_{\delta=0.36\%}$ and 7.9% for D_{ult}. For the 1200-mm double-cage specimens (**Fig. 4.6,** c & d), error in $D_{\delta = 0.36\%}$ was greater than 10% in both cases, specifically 10.4% and 11.5% for the 100D and 140D models, respectively. Since tensile behaviour of the concrete was not measured during experiments, the validation models assume the same tension stiffening parameter values as the calibration models, which may explain the high error in D_{δ}. However, error in D_{ult} was only 4% for both cases, showing great agreement with experimental results when considering ultimate load only. The triple-cage model (**Fig. 4.6,** e) exhibited 0.8% error in D_{peak} and 12.0% in D_{ult}. The models also showed good representation of the experimental load-deflection behavior shape and rigidity, indicating the models are appropriate for use in further parametric studies.

4.3.3 Stresses in FEM Concrete Material

This subsection discusses the stress in the concrete material for three models representing the three common RCP cage configurations. **Figures 4.7** to **4.9** show the distribution of maximum principal stresses in concrete for the single, double, and triple-cage models, respectively. In terms of stress propagation, the models behaved as expected based on the failure modes observed in Chapter 3.

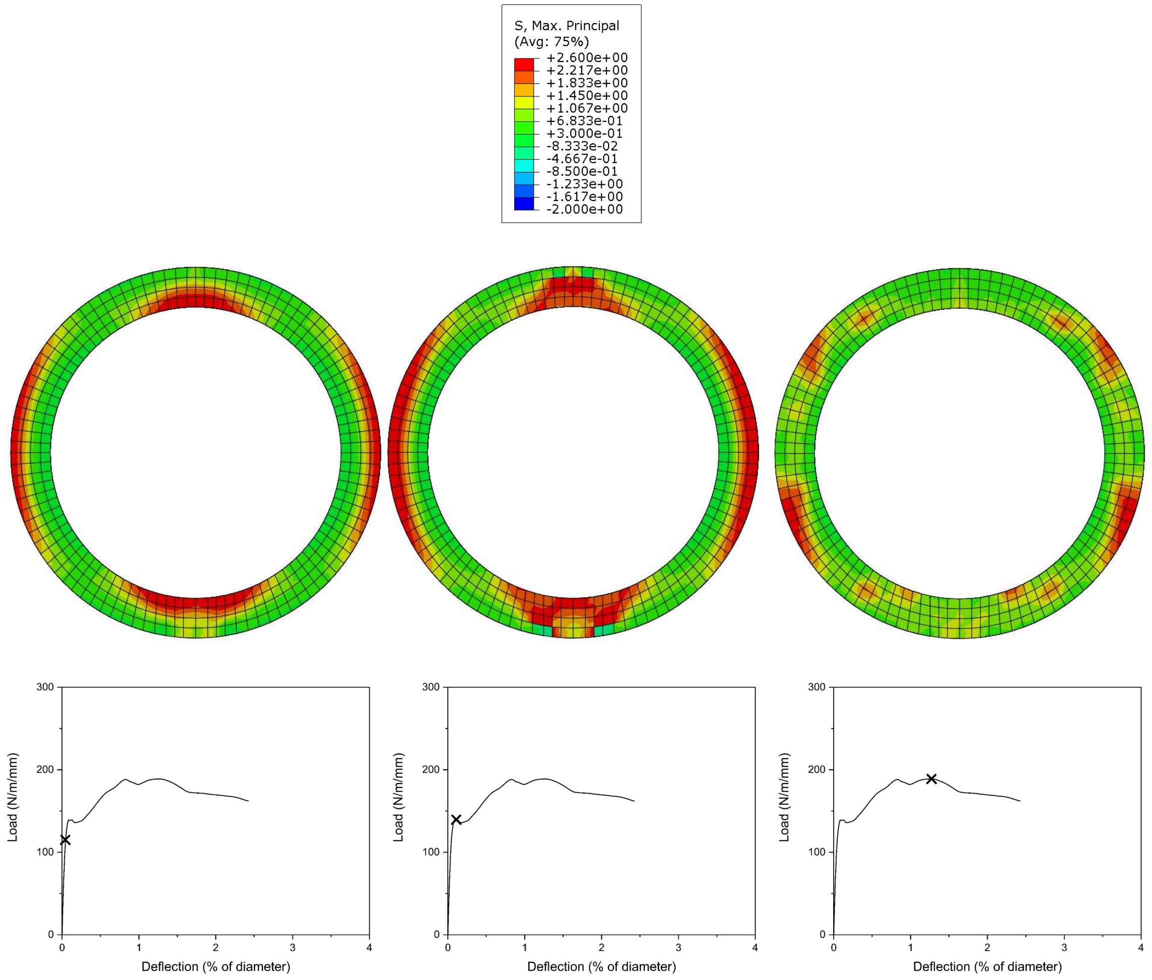

(a) (b) (c)

Figure 4.7: Stress distribution development within concrete material for typical 825-mm single-cage model. Legend values are in MPa. Positive values indicate tension.

In the case of single-cage models (**Fig. 4.7**), stresses initially concentrated at the inner vertical faces of the pipe (obvert & invert), and outer horizontal faces (spring-lines) (**Fig. 4.7,** a). As loading progressed to D_{peak} (**Fig. 4.7,** b), invert and obvert elements began to reach their tensile capacity and exhibit cracking behaviour, causing stresses to shift away from the inner pipe face and towards the bearing supports. This behavior indicates flexural action as the main cause of cracking and eventual failure. As loading progressed to post-crack D_{ult} (**Fig. 4.7,** c), the overall region of stress in the concrete was reduced, indicating the transfer of stresses to the steel reinforcement.

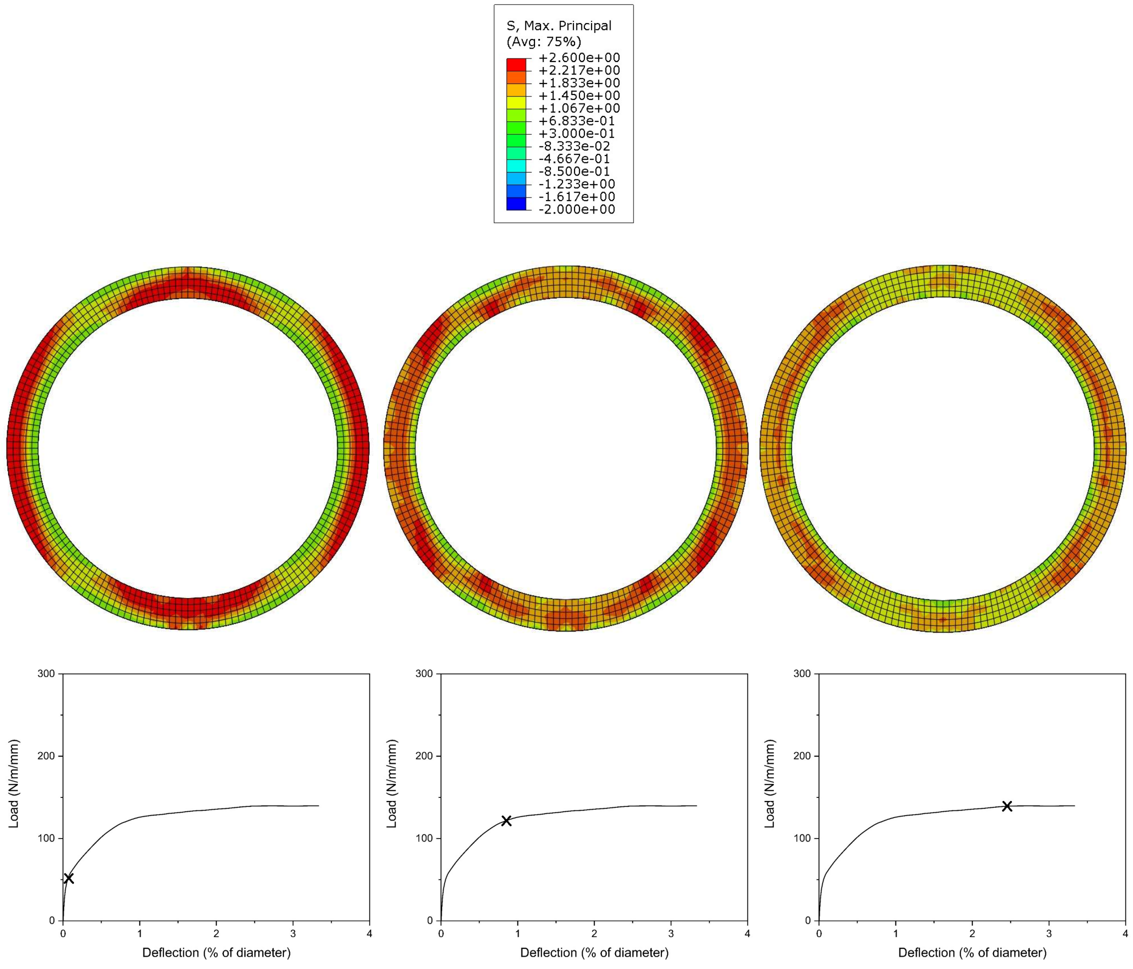

(a) (b) (c)

Figure 4.8: Stress distribution development within concrete material for typical 1200-mm double-cage model. Legend values are in MPa. Positive indicates tension.

Figure 4.8 shows the principal stress distribution of double-cage models during loading. At early stage of TEBT (**Fig. 4.8,** a), the stress distribution in the pipe encouraged the formation of multiple cracks on the invert and obvert faces. As loading progressed towards plasticity (**Fig. 4.8,** b), the distribution of the invert and obvert stresses exhibited formation of diagonal cracks indicative of the shear failure observed in experiments (See **Fig. 3.8,** c, in Chapter 3). As load continued to increase (**Fig. 4.8,** c), the concrete structure deteriorated and load-deflection behavior became entirely plastic. Stress in the concrete material was greatly reduced, suggesting that the steel reinforcement started to govern the load-deflection behavior in the plastic phase.

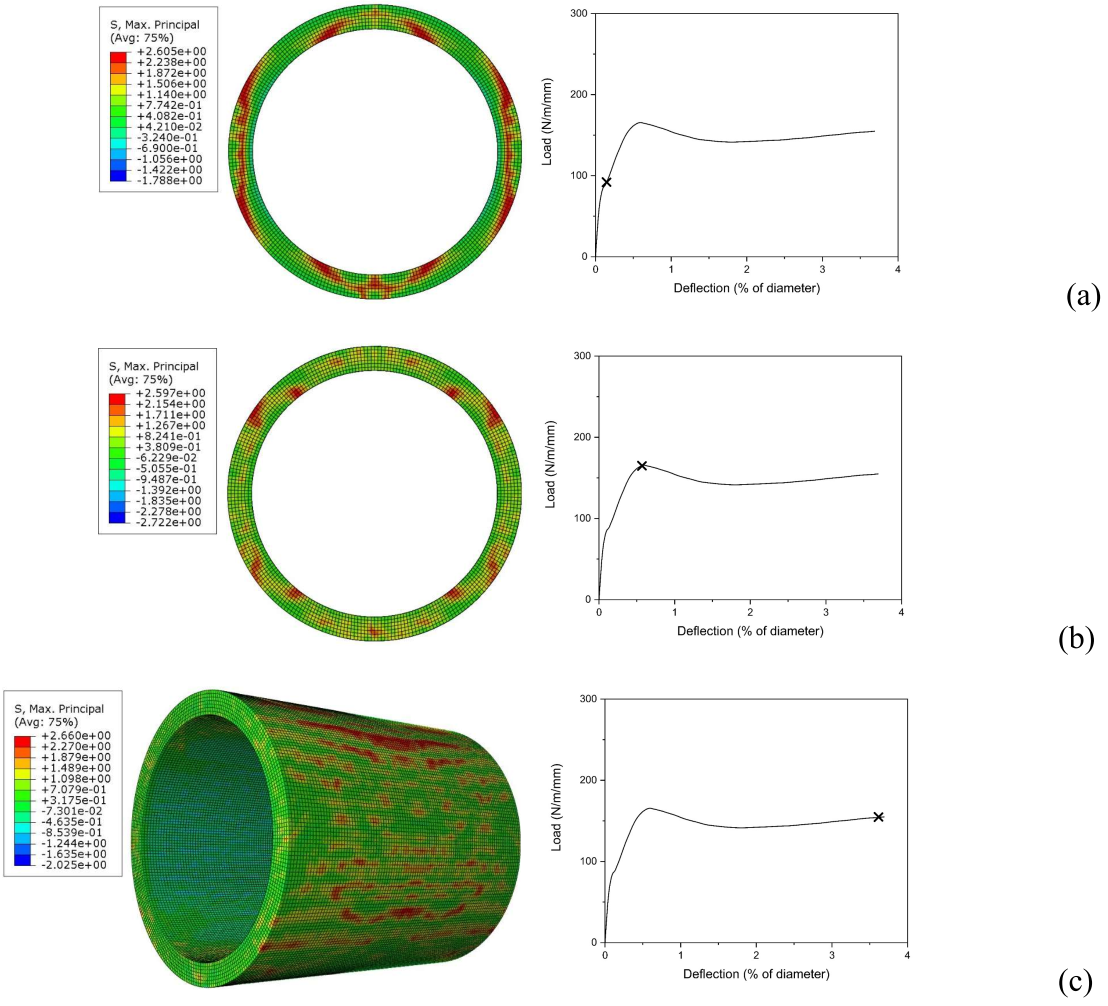

Figure 4.9: Stress distribution development within concrete material for typical 1800-mm triple-cage model. Legend values are in MPa. Positive indicates tension.

Figure 4.9 shows the principal stress distribution of the triple-cage RCP model. During the linear load-deflection phase (**Fig. 4.9,** a), the stress distribution in the model indicated formation of multiple cracks at the invert, obvert, and outer spring-line faces. As loading progressed and reached D_{peak} (**Fig. 4.9,** b), stress localized at the pipe haunches away from the invert, obvert, and spring-lines. This stress distribution was different than the one observed in the case of single-cage RCP reaching D_{peak} (**Fig. 4.7,** b), where stress was still concentrated at the invert, obvert, and spring-lines. During the plastic phase (**Fig. 4.9,** c), stress at the inner concrete face was reduced and instead became dispersed around the outer face. **Figure 4.9** (c) was rotated in order to better display the stress regions on the outer face.

4.3.4 Stresses in FEM Steel Reinforcement

While concrete behavior could be observed based on cracking and crushing during the TEBT, the behavior of steel reinforcement was not easily observed during experimental testing. However, the developed FEMs allow for the state of stress in the full reinforcement cage to be assessed at any point during analysis. This subsection discusses the state of stress in the steel reinforcement for the three models covered in the previous subsection.

Figure 4.10 shows the distribution of maximum principal stresses in the steel reinforcement for an 825-mm single-cage RCP model. The location of the concrete material is also shown. During the elastic phase (**Fig. 4.10,** a), the magnitude of tensile stress in steel was greater at the obvert than the invert. This is due to the invert stress being distributed across a wider length. This was caused by obvert TEBT load being concentrated at one bearing, whereas invert load was spread between two bearings. Although multiple concrete cracks were often observed at the invert, fewer cracks tended to occur at the obvert. Multiple concrete cracks allow for tensile stresses to be developed across a wider length of steel, reducing the maximum stress. At D_{peak}-load (**Fig. 4.10,** b), stresses in the steel reinforcement continued to increase. At this stage, experimental samples exhibited some cracking at the outer spring-lines. The effect of these cracks was evidenced in the model by tensile stresses developing at the reinforcement spring-lines. Since reinforcement was more favorably positioned in the tension zones at the invert and obvert, tensile stresses at reinforcement spring-lines were significantly lower. As the specimen reached D_{ult} (**Fig. 4.10,** c), steel begun yielding at all four critical sections (invert, obvert, and spring-lines). In the model, this was indicated by the steel at those locations reaching its yield strength of 600 MPa. This behavior was in line with experimental observations of flexural failure and necking in some single-cage RCP specimens (See **Fig. 3.8,** a**,** and **3.10,** a, from Chapter 3).

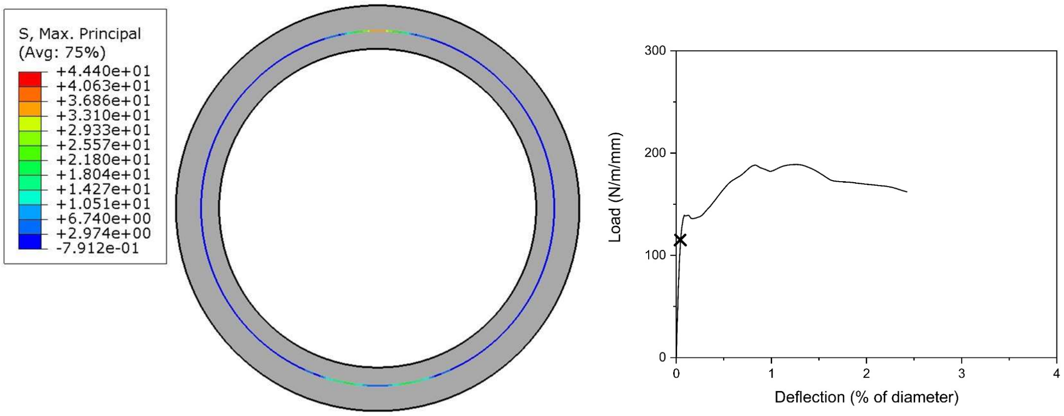

(a) Stress distribution during elastic phase

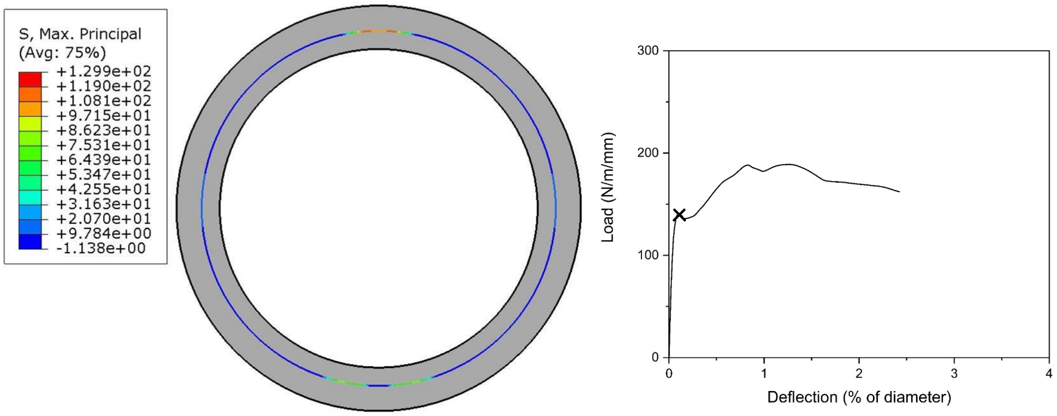

(b) Stress distribution at D_{peak}

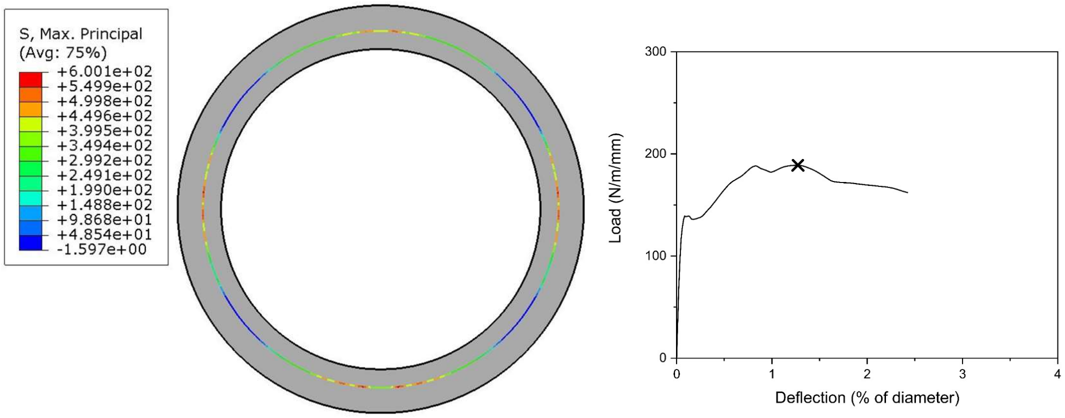

(c) Stress distribution at D_{ult}

Figure 4.10: Stress distribution development within steel reinforcement for typical 825-mm single-cage model. Legend values are in MPa. Positive indicates tension.

Figure 4.11 shows the distribution of maximum principal stresses in the steel reinforcement for a 1200-mm double-cage RCP model. The location of the concrete material is shown for context. As in the single-cage model, tensile stresses during the elastic phase (**Fig. 4.11,** a) were greater in the invert compared to the obvert. However, the difference in magnitude of stress between the two zones was not as significant as in the single-cage model. Tensile stress in the obvert was around 113 MPa compared to 94 MPa in the invert. This is likely due to the larger own-weight of the 1200-mm pipe balancing the stress-reducing effect of the load being distributed across two bearings in the invert section. Another notable difference in this model compared to the single-cage model was the development of stresses in the spring-lines at an early stage, due to the outer-cage already being positioned within the tensile zone of the intact section. As loading continued towards the inelastic phase (**Fig. 4.11,** b), tensile stress continued to increase at the four critical sections. Maximum tensile stresses reached 400 MPa at the inner-cage obvert, 330 MPa at the inner-cage invert, and around 250 MPa at the outer-cage spring-lines. Significant tensile stresses also occurred at the invert and obvert of the outer-cage, indicating reduction of the compression zone caused by increasing crack depth at those locations. Further into the inelastic deflection phase (**Fig. 4.11,** c), stresses became more significant in the outer-cage spring-lines rather than the inner-cage invert and obvert sections. This behavior indicates that the outer-cage provided significant contribution to D_{ult} by influencing late-stage load-deflection behavior. Maximum tensile stress in the steel was 500 MPa at this deflection point, indicating that the yield strength of 600 MPa was not reached even at this stage. This is in agreement with experimental observations in Chapter 3, where yielding of steel was not observed in double-cage RCP specimens. Double-cage specimens tended to fail by diagonal tension (See **Fig. 3.8,** c, from Chapter 3), signifying that shear capacity (rather than flexural capacity) governed failure of most double-cage RCP specimens.

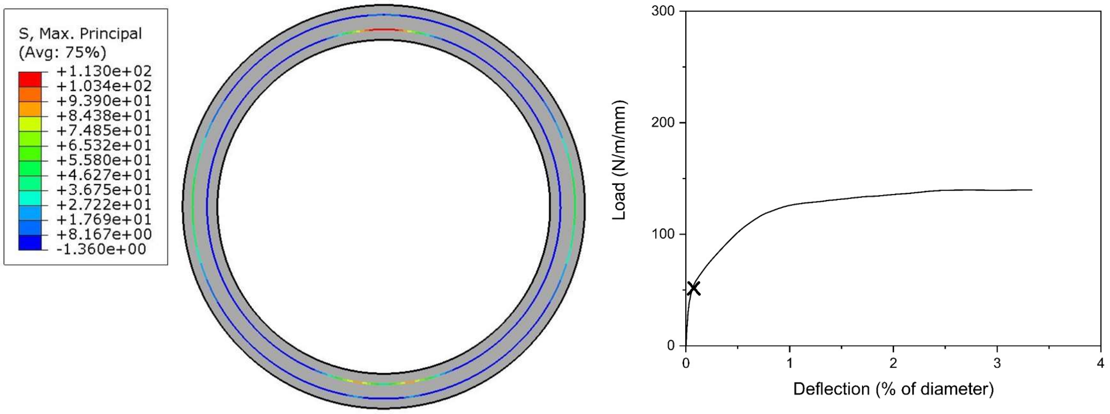

(a) Stress distribution during elastic phase

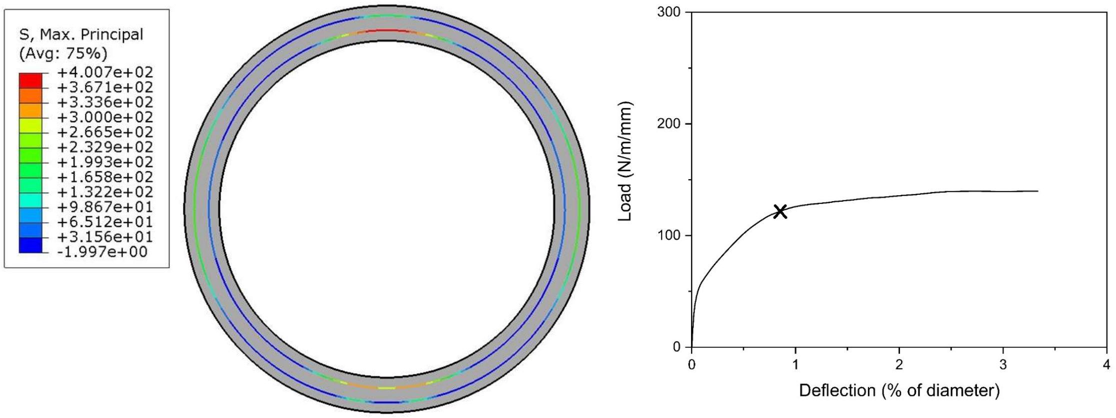

(b) Stress distribution towards inelastic phase

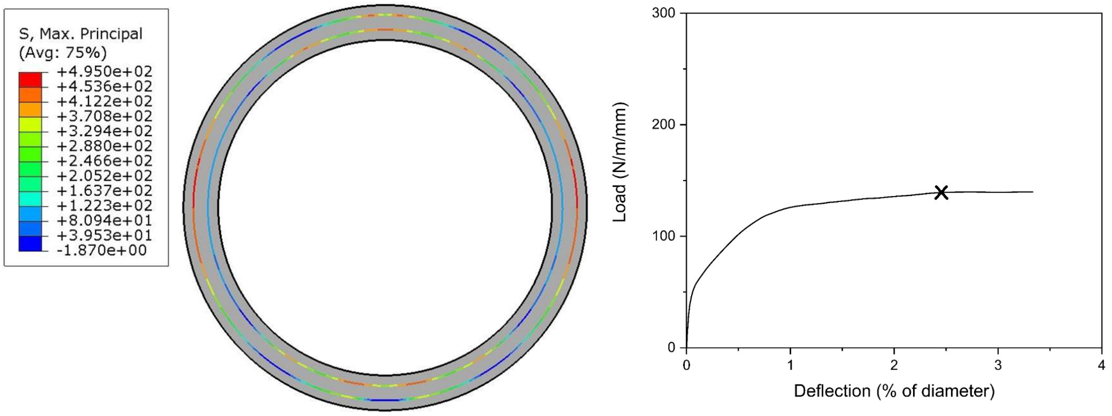

(c) Stress distribution during inelastic phase

Figure 4.11: Stress distribution development within steel reinforcement for typical 1200-mm double-cage model. Legend values are in MPa. Positive indicates tension.

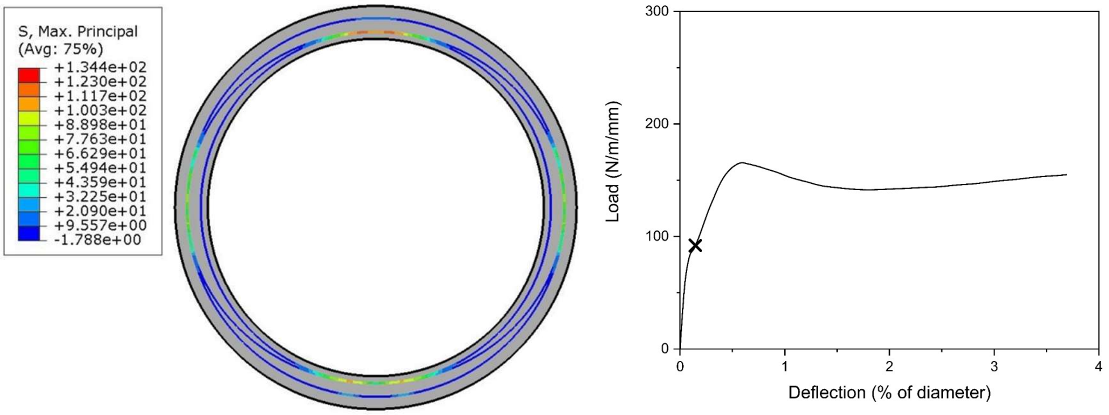

(a) Stress distribution during elastic phase

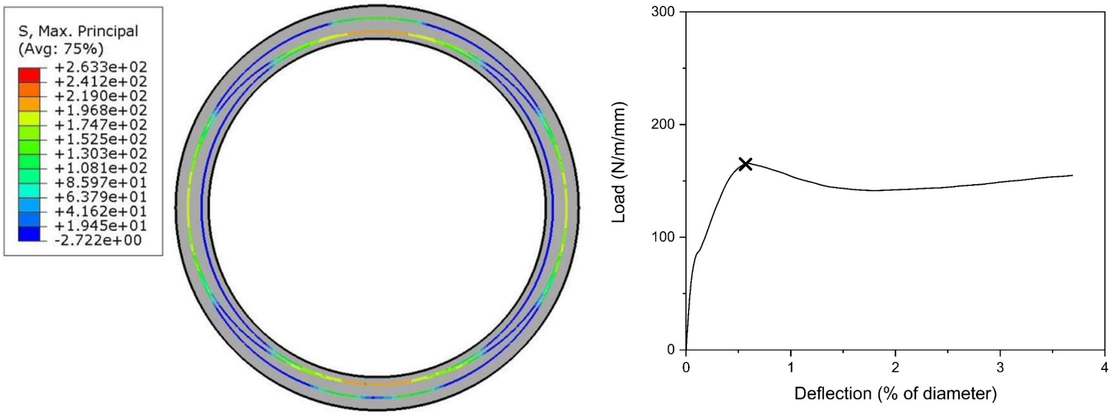

(b) Stress distribution at D_{peak}

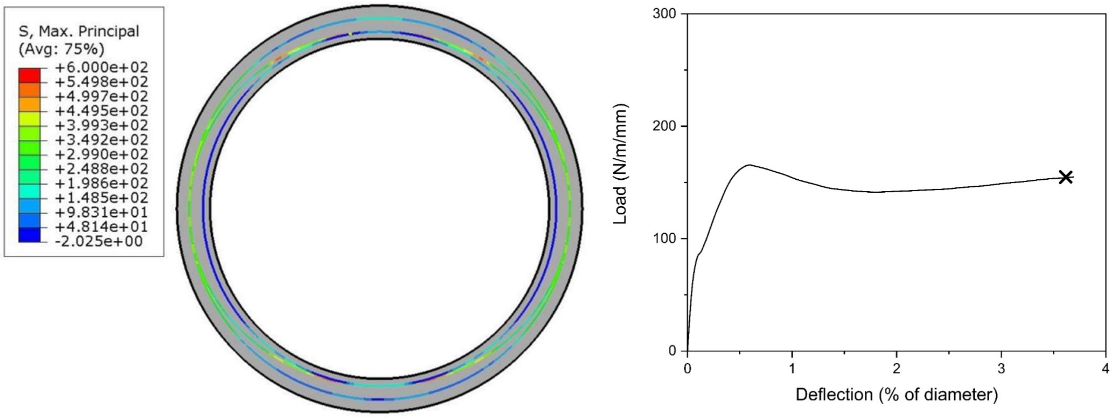

(c) Stress distribution at D_{ult}

Figure 4.12: Stress distribution development within steel reinforcement for typical 1800-mm triple-cage model. Legend values are in MPa. Positive indicates tension.

Figure 4.12 shows the distribution of maximum principal stresses in the steel reinforcement for an 1800-mm triple-cage RCP model. As in the single and double-cage models, invert stresses were greater than obvert stresses during the elastic phase (**Fig. 4.12,** a). Significant tensile stresses were also developed at the spring-lines during this stage, similar to the double-cage model. At D_{peak} (**Fig. 4.12,** b), tensile stresses continued to increase in the inner-cage at the invert and obvert, and outer-cage at the spring-lines. Significant stresses also begun to develop in the outer-cage at the invert and obvert. In contrast, stresses did not develop in the inner-cage at the spring-lines. Late into the plastic phase (**Fig. 4.12,** c), stress developed in nearly all areas of the steel cages, except for the inner cage at the spring-lines. The elliptical cage became fully engaged at this stage, allowing the reinforcement to be more efficient by increasing the cross-sectional area of steel at the tension zones. This is evidenced by the lower stresses at the outer spring-lines in the triple-cage RCP model compared to the double-cage model. Although yielding in triple-cage RCP could not be observed during the experimental program, the model suggests that the elliptical cage begun to yield at the 10 and 2 o'clock positions of the pipe face.

4.4 Parametric Analysis

A reinforcement-based parametric study was performed on the six single-cage and double-cage FEMs developed in the previous section. The study was divided into four subsections investigating the effects of (i) reinforcement steel, (ii) yield strength, (iii) cover, and (iv) position on the load-deflection behavior of the RCP models. In addition to the six developed models, 68 total models were generated to present an in-depth examination of the sensitivity of the four listed parameters.

4.4.1 Effect of Steel Reinforcement Area

Steel reinforcement is a key parameter affecting RCP capacity. While CSA A257.2 (2014) does not specify minimum reinforcement, ASTM C76 (ASTM C76, 2016) specifies a minimum inner cage reinforcement area equivalent to 150 mm^2/m for 140D pipe under 375-mm nominal diameter and 100D & 65D pipe under 525-mm nominal diameter. To investigate the effect of reinforcement area on load-deflection output, the reinforcement area of each model was reduced by 20%, 30%, and 50% from the actual reinforcement area of the corresponding specimen (See **Table 4.1**).

Figures 4.13 (a & b**)** show the load-deflection output of the single-cage models with different reinforcement area reductions. The most notable load-deflection effects of the reinforcing steel area were observed post-D_{peak}, with higher amounts of steel producing higher post-crack load capacity. Load-deflection stiffness before D_{peak} was unchanged. This is corroborated by findings in Massenzio *et al.* (2005) which show that steel reinforcement did not significantly affect the natural frequency (function of stiffness and mass) of uncracked reinforced-concrete sections. Accordingly, altering the amount of steel reinforcement in the models did not significantly affect the stiffness of the pre-crack load-deflection response. Although crack occurrence tended to be governed by the concrete tensile strength, lowering the steel reinforcement decreased D_{peak}. After the initial drop in capacity following D_{peak}, single-cage FEMs regained some capacity in the inelastic phase. However, some 65D variants (**Fig. 4.13,** a) did not surpass their D_{peak}-load. This was also observed with some 825-mm 65D specimens in the experiments of Chapter 3.

Figures 4.13 (c − f) show the load-deflection output of the double-cage RCP models with reduced steel reinforcement areas. Comparable to the single-cage models, initial stiffness was not influenced by altering the steel content. Notable changes in stiffness caused by reduced steel reinforcement occurred past a deflection of approximately δ = 0.2%, indicating that significant cracking occurred in the concrete section for double-cage RCP. The effects of reducing the steel reinforcement were more significant in the inelastic load-deflection region. As cracks increased and the concrete structure deteriorated, stiffness became dependent on the performance of the steel reinforcement. The subsequent figure groups together the load-deflection results of all the FEMs and compares the effect of the different steel reinforcement areas on D_{peak}, $D_{\delta=0.36\%}$, and inelastic post-crack D_{ult}. Inelastic D_{ult} refers specifically to maximum loads obtained in the inelastic phase in order to distinguish it from cases where D_{ult} may equal D_{peak} (for example, 825-mm 65D after reducing steel area).

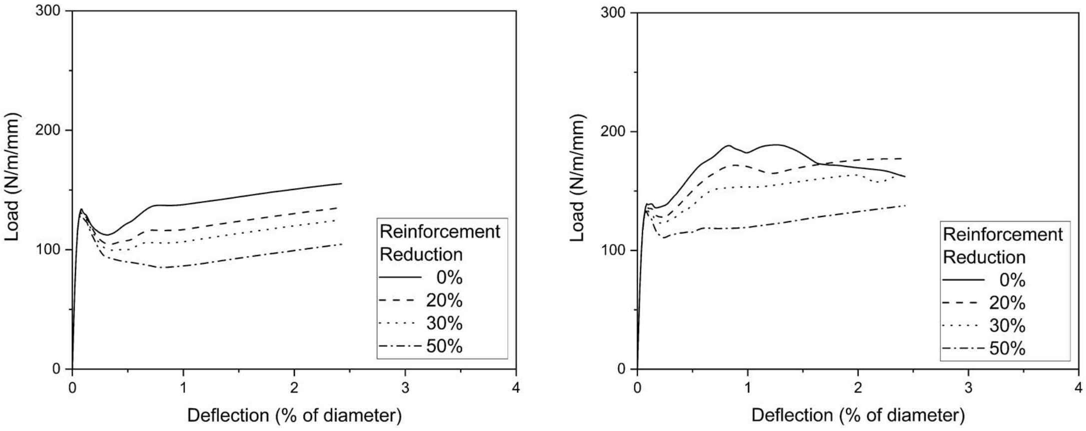

(a) 825-mm 65D

(b) 825-mm 100D

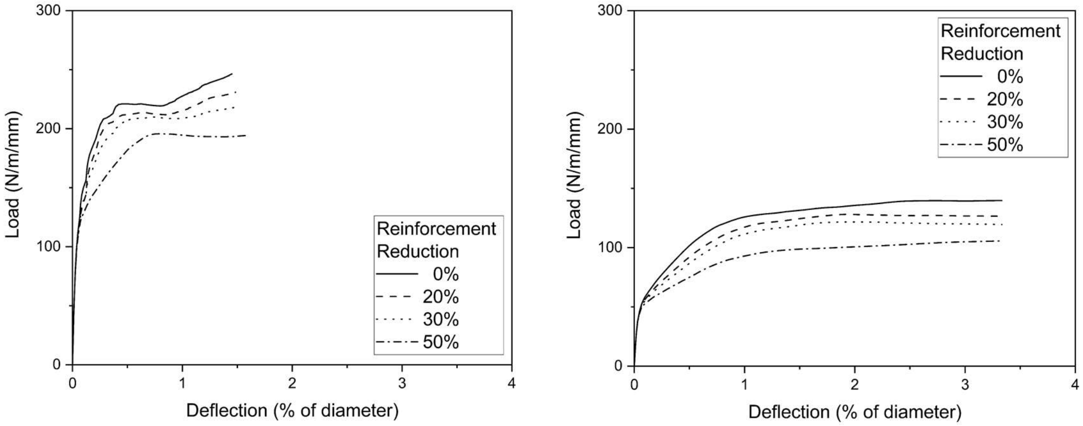

(c) 825-mm 140D

(d) 1200-mm 65D

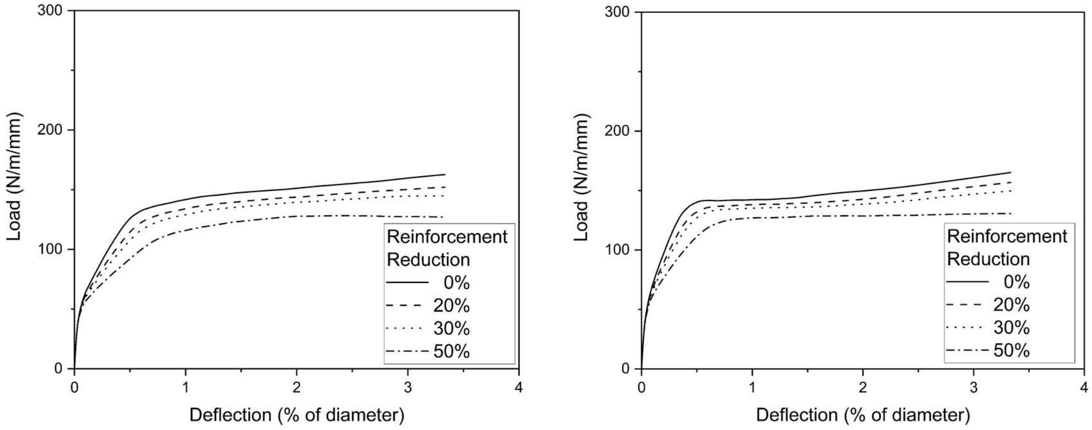

(e) 1200-mm 100D

(f) 1200-mm 140D

Figure 4.13: Effect of reducing steel reinforcement area on load-deflection profiles of all models.

Figures 4.14 (a & b) compare the service-load capacity for each model under different reinforcement areas. Service-load is taken as D_{peak} for single-cage models, and $D_{\delta=0.36\%}$ for double-cage models. D_{peak} increased by 3.1 N/m/mm for every 100 mm^2/m increase in steel reinforcement area between 150 and 500 mm^2/m for the 825-mm single-cage models. The 825-mm double-cage model performed much more efficiently than its single-cage counterpart, with the same increase in reinforcement area increasing the service-load $D_{\delta=0.36\%}$ by 9.5 N/m/mm. Double-cage RCP allowed reinforcement to be positioned more favorably in the pipe tension zones, hence the steel was utilized more efficiently. The double-cage 825-mm model achieved a service capacity of 167-N/m/mm with a reinforcement area of 452-mm^2/m (291-mm^2 inner and 161-mm^2/m outer reinforcement), compared to a service capacity of only 139-N/m/mm with a reinforcement area of 484-mm^2/m in the single-cage model. For the 1200-mm double-cage FEMs, $\mathrm{D}_{\delta=0.36\%}$ increased by 3.9-N/m/mm for every 100-mm^2/m increase in total reinforcement area between 480 and 1800-mm^2/m.

Figure 4.14 (c) compares the maximum post-crack, inelastic D_{ult}-load reached in each model with its corresponding steel reinforcement area. 825-mm 65D & 100D data points were on the same line, as the main difference between the two specimens was the steel area and spacing. For the 825-mm single-cage models, increasing the steel area by 100-mm^2/m led to 25-N/m/mm increase of post-crack D_{ult}. The 825-mm 140D double-cage model increased D_{ult} by 11-N/m/mm for every 100-mm^2/m increase in steel area between 500 and 800 mm^2/m. For the 1200-mm 65D & 100D models, data points were grouped, but separated from the 140D model. The 1200-mm 140D model performed less efficiently, requiring greater (almost 400mm^2/m) total steel reinforcement than its 65D & 100D counterparts to achieve similar D_{ult} capacity. This can be attributed to the reinforcement distribution between the inner and outer cage for the double-cage RCP. Inner reinforcement made up 60% and 56% of total reinforcement for the 65D and 100D model, respectively, whereas for the 140D model, the inner reinforcement was 70% of the total. These results indicate that the outer cage contributed to D_{ult} capacity and an inner-to-outer reinforcement distribution of 60%-to-40% performing more favorably in D_{ult} than a distribution of 70%-to-30%.

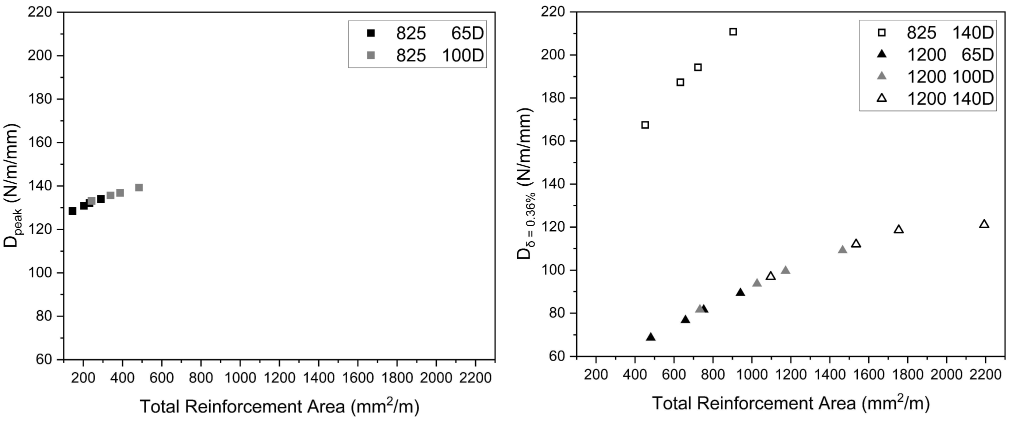

(a) D_{peak}

(b) $D_{\delta = 0.36\%}$

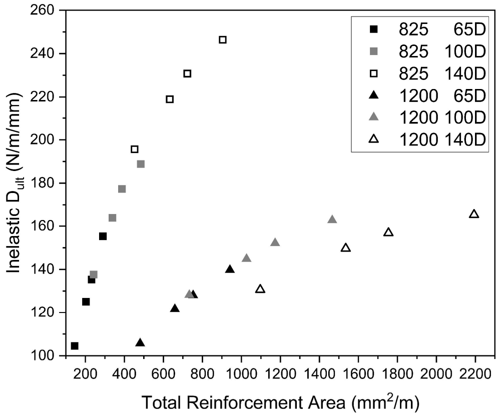

(c) Post-crack D_{ult}

Figure 4.14: Effect of total inner and outer reinforcement area on (a) D_{peak} (single-cage models), (b) $D_{\delta = 0.36\%}$ (double-cage models), and (c) post-crack D_{ult}.

4.4.2 Effect of Steel Yield Strength

CSA A257.2 clause 4.1.4 (2014) and ASTM C76 clause 6.5 (2016) indicate that RCP reinforcement shall conform to ASTM A1064/A1064M (carbon-steel wire), ASTM A615/A615M (carbon-steel bars), or ASTM A706/A706M (low-alloy steel bars). ASTM C76 also allows for the use of reinforcement conforming to ASTM A36/A36M (carbon structural steel). While CSA A257.2 makes no mention of specific grades, ASTM C76 limits the use of A615/A615M bars to Grade 40 or 60 (yield strengths of 280 or 420 MPa) and A706/A706M bars to Grade 60 (yield strength of 420 MPa). Except for ASTM A615/A615M Grade 40 and A36/A36M, minimum yield strengths of the wire and bar specifications mentioned generally lie in the range of 420 to 550 MPa (ASTM A36/A36M,

2019; ASTM A615/A615M, 2018; ASTM A706/706M, 2016; ASTM A1064/A1064M, 2018). To investigate the effects of yield strength on RCP performance, yield was varied for each FEM in the range of 450 to 600 MPa.

Figures 4.15 (a & b) show the effect of altering the steel yield strength on the load-deflection output of single-cage models. Yield strength did not seem to affect D_{peak}, indicating that the cracked section did not develop yield in its elastic phase. In the 825-mm 65D model, higher yield strengths allowed the model to regain significant load capacity after the D_{peak} load drop. Higher yield strengths displayed higher inelastic stiffness, until steel reinforcement begun yielding, at which point stiffness became equal for all yield strengths. Yielding was observed in several single-cage RCP specimens during the experimental phase (See **Fig. 3.10**, a, from Chapter 3). Like the 825-mm 65D model, 825-mm 100D models with higher steel yield strength regained more load capacity post-D_{peak}. However, inelastic behavior was less predictable. 825-mm 100D models with yield strengths of 450 MPa and 500 MPa continued gaining strength towards loads of 175-N/m/mm and 185-N/m/mm, respectively. However, the 825-mm 100D models with yield strengths of 550 MPa and 600 MPa lost significant capacity at a D-load of around 190-N/m/mm. As observed in the experimental program, RCP specimens with high steel reinforcement tended to be governed by diagonal tension (shear) capacity rather than flexural capacity. As such, at higher loads specimens were governed by the shear section capacity rather than steel yield capacity.

Figures 4.15 (c − f) show the effect of altering the steel yield strength on the load-deflection output of double-cage RCP models. Yield strength had no bearing on $D_{\delta = 0.36\%}$ for double-cage models, as with D_{peak} for single-cage. Except for the 1200-mm 65D model with yield strength of 450 MPa, earliest yield did not occur until a deflection of at least $\delta = 1\%$ for the double-cage models. This is in contrast with the single-cage models, where yield occurred within $\delta = 1\%$ for all yield strength values. This is in accordance with the experimental observations in Chapter 3, where double-cage specimens failed through diagonal and radial tension with no evidence of yielding in steel reinforcement. Reinforcement yield strength was therefore less significant in double-cage RCP, as failure was governed by shear rather than flexure.

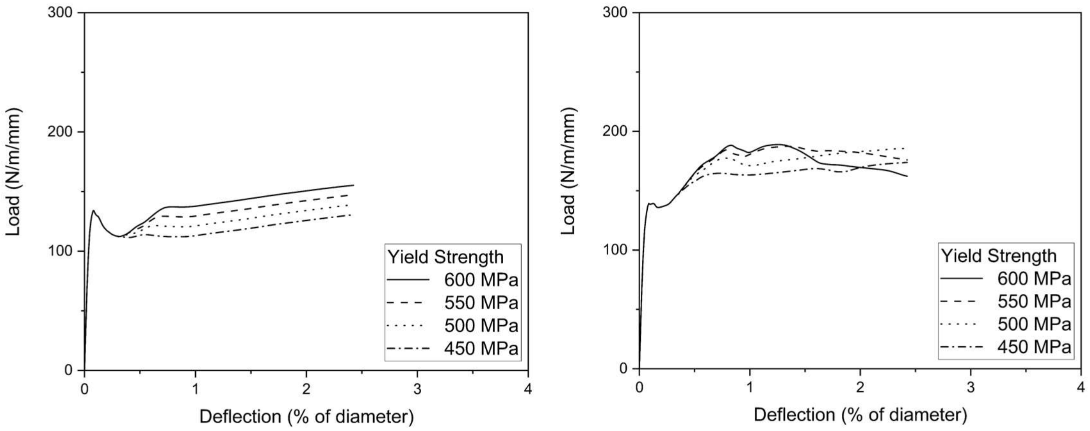

(a) 825-mm 65D

(b) 825-mm 100D

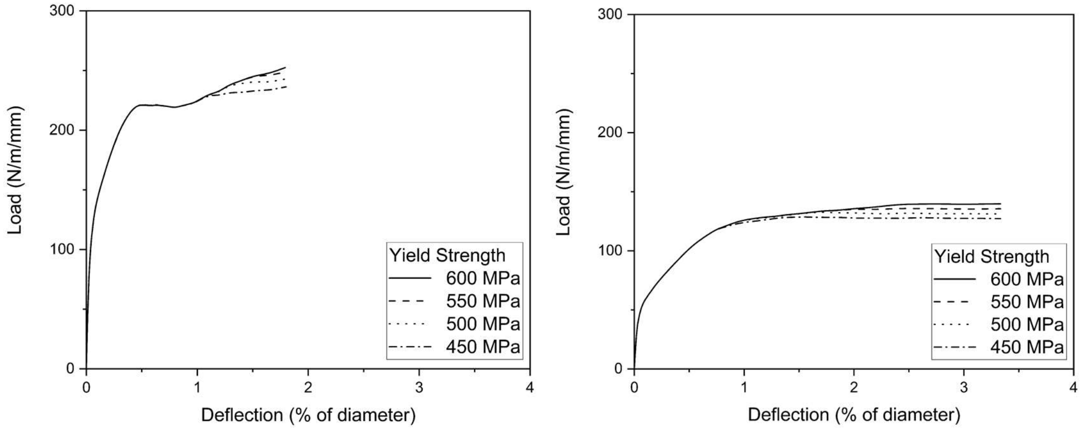

(c) 825-mm 140D

(d) 1200-mm 65D

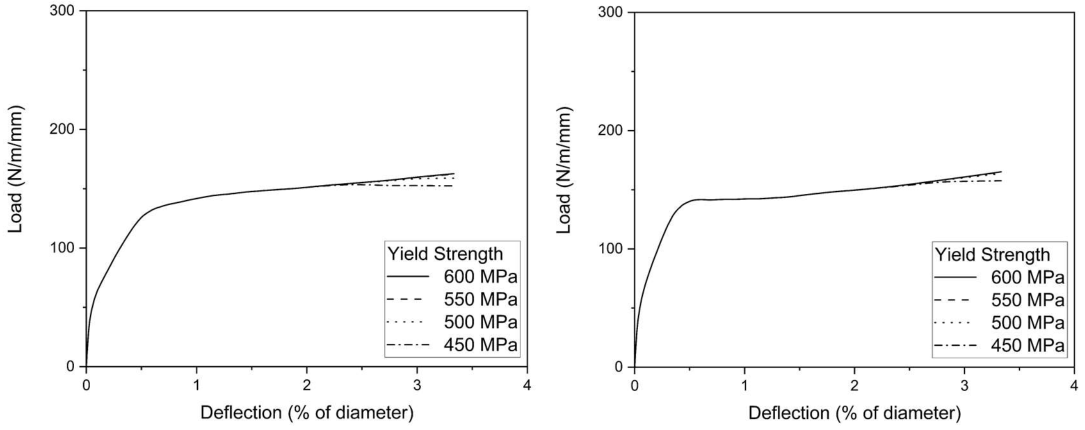

(e) 1200-mm 100D

(f) 1200-mm 140D

Figure 4.15: Effect of reducing reinforcement yield strength on load-deflection profiles of all models.

Figure 4.16 compares the post-crack D_{ult} with the steel yield strength for all RCP models. Both 65D pipe models were highly sensitive to changes in the steel yield strength, while the 100D and 140D classes were considerably less sensitive, apart from the 825-mm 140D double-cage model. For the 825-mm 65D model, inelastic D_{ult} increased steadily with yield strength by 16 N/m/mm per 100 MPa between 450 and 600 MPa. The 1200-mm 65D model also showed steady increase in D_{ult} from 450 to 600 MPa, with each 100 MPa increase in yield strength adding 7 N/m/mm to D_{ult}.

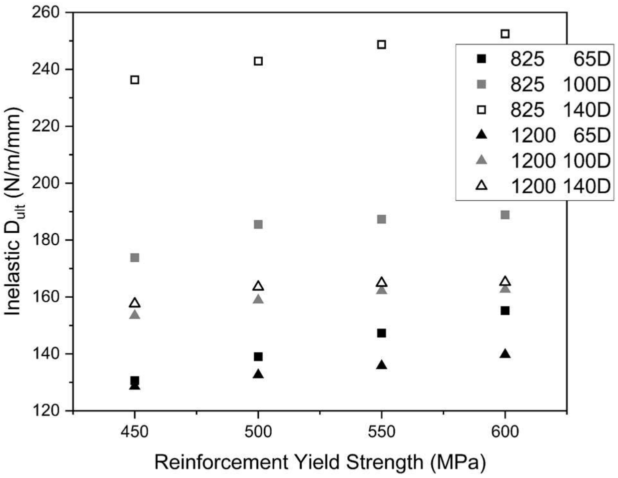

Figure 4.16: Relationship between inelastic D_{ult} and reinforcement yield strength.

In contrast, D_{ult} increase due to reinforcement yield strength was not continuous for 100D and 140D models except for the 825-mm 140D model, suggesting that those models were less susceptible to flexural failure. Although increasing the 825-mm 100D reinforcement yield strength from 450 to 500 MPa initially caused D_{ult} to increase by about 12 N/m/mm, further increasing the yield strength to 600 MPa caused D_{ult} to increase by only 3 N/m/mm. For the 1200-mm 100D double-cage model, D_{ult} initially increased with yield strength at a rate of 9 N/m/mm per 100 MPa between 450 and 550 MPa. This rate decreased to about 0.9 N/m/mm per 100 MPa increase in yield strength above 550 MPa. For 1200-mm 140D, increasing the yield strength by 50 MPa from 450 to 500 MPa increased D_{ult} by 6 N/m/mm. However, further increasing the yield strength by 100 MPa from 500 to 600 MPa only produced a D_{ult} increase of around 1.7 N/m/mm.

4.4.3 Effect of Concrete Cover to Inner Cage

Per CSA A257.2 clause 8.1.1 (2014) and ASTM C76 clause 8.1.2 (2016), RCP reinforced with single layer of steel shall have concrete cover of between 35% to 50% of wall thickness from the inner face. In the case of double layer steel, a minimum concrete cover of 25-mm shall be maintained (given as 1-in. in ASTM) (ASTM C76, 2016; CSA A257, 2014). The modelled specimens had a cover of 47.9-mm (42% of wall thickness) for the single-cage RCP, 36.3-mm (30% of wall thickness) for the 825-mm double-cage RCP, and 37.9-mm (30% of wall thickness) for the 1200-mm RCP from the inside face. To explore the significance and effect of cover distance, the inner steel-cage diameter was altered for single and double-cage RCP models. For single-cage models, cover was set as 40%, 30%, 20%, and 10% of wall thickness. In double-cage models, inner cage cover was set as 30%, 20%, and 10% of wall thickness. Minimum cover of 25-mm corresponds to approximately 20% for both single and double-cage models. **Figure 4.17** provides a reference for the cover positions discussed in this section.

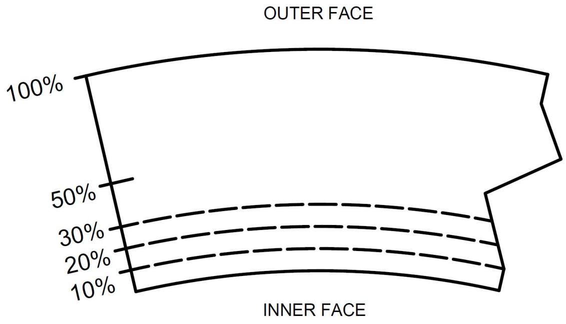

Figure 4.17: Reference drawing for an obvert RCP section indicating location of cover at 10%, 20%, and 30% wall thickness.

Figure 4.18 shows the load-deflection behavior of the FEMs under different inner-cage cover distances. The cover significantly affected D_{peak} for the single-cage RCP models (**Fig. 4.18,** a & b) and stiffness past $\delta = 0.2\%$ for double cage RCP models (**Fig. 4.18,** c – f), as well as overall pipe performance for both types. Load-capacity was improved with decreased cover, as increasing the rebar depth in the tension zone improves the moment resisting capacity of RC structures. This also indicates the importance of maintaining dimensional tolerance of the steel cage during fabrication process.

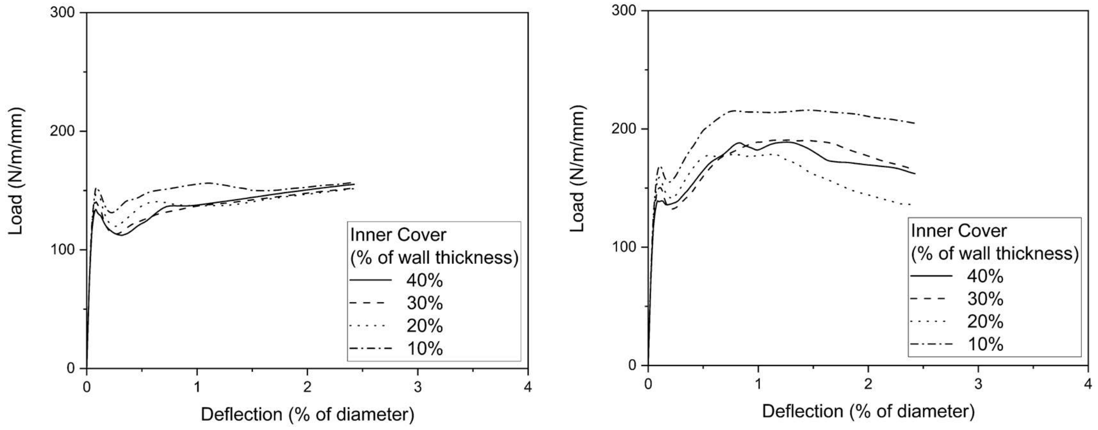

(a) 825-mm 65D

(b) 825-mm 100D

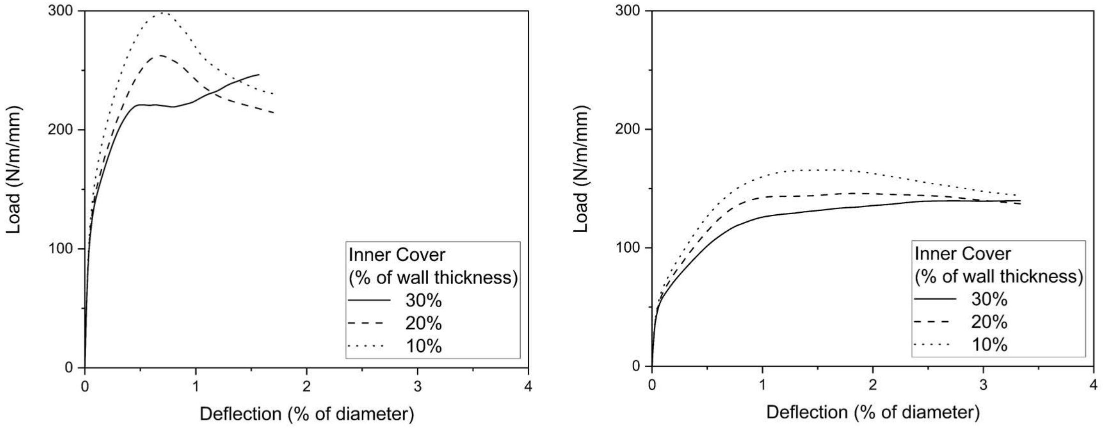

(c) 825-mm 140D

(d) 1200-mm 65D

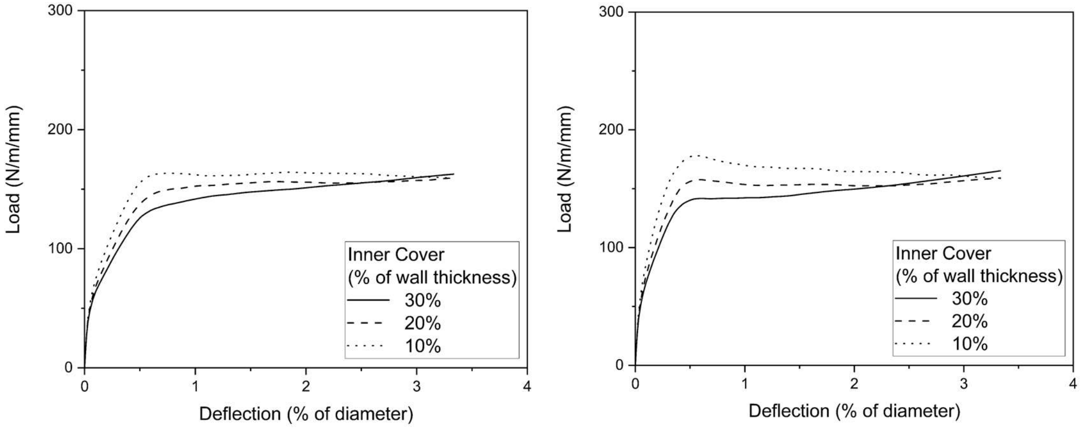

(e) 1200-mm 100D

(f) 1200-mm 140D

Figure 4.18: Effect of reducing steel reinforcement cover on load-deflection profiles of FE models.

Figure 4.19 (a) presents the effects of different cover distances on D_{peak} for single-cage RCP models. Because of the larger steel area, the effect of the cover contributing to D_{peak} capacity was more significant in the 100D model compared to the 65D. As such, D_{peak} was more sensitive to changes in cover for the 100D model compared to the 65D. Increasing the cover from the inner face by 10% of wall thickness decreased D_{peak} by 6.2 N/m/mm and 9.8 N/m/mm for the 65D and 100D models, respectively. **Figure 4.19** (b) presents the effects of different inner cage cover distances on $D_{\delta=0.36\%}$ for double-cage RCP models. Increasing cover from the inner face by 10% of wall thickness decreased $D_{\delta=0.36\%}$ by 10.2 N/m/mm for the 1200-mm 65D, 12.7 N/m/mm for the 1200-mm 100D, and as much as 22.6 N/m/mm for both the 825-mm and 1200-mm 140D models. Again, models of the same diameter with higher steel content were found to be more sensitive to changes in cover.

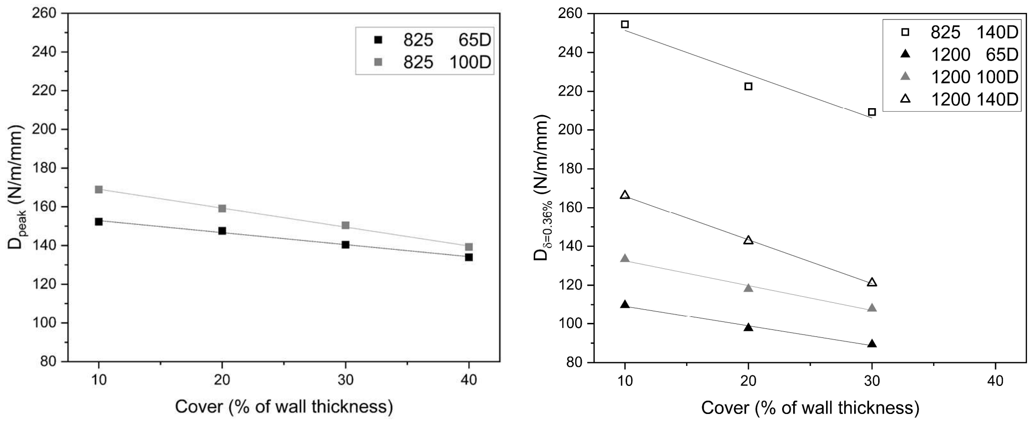

(a) Single-Cage

(b) Double-Cage

Figure 4.19: Effect of increasing cover on (a) D_{peak} and (b) $D_{\delta = 0.36\%}$ for single and double-cage models, respectively.

Although decreasing the cover can significantly improve the service capacity of RCP, insufficient cover can cause durability issues. For example, Meira *et al.* (2010) showed that decreasing the cover can drastically reduce service life of concrete exposed to chloride ion environments, can corrode steel rebar. Larger cover improved durability to chloride attack by increasing the time required for the chloride ions to reach the steel rebar. Since RCP is used in storm and waste-water conveyance, the cover limits specified by CSA and ASTM are necessary for protection against chlorides and other aggressive chemicals (ACPA, 2016).

4.4.4 Effect of Inner Cage Position

During the RCP dry-cast manufacturing process, vibrators are used after pouring concrete to reduce voids. These vibrations often cause the steel-cage to shift within the cast, offsetting the cage from its desired position. CSA A257.2-14 clause 8.3 (CSA A257, 2014) and ASTM C76 clause 12.5.1 (ASTM C76, 2016) allow for a variation in initial cage position of up to 10% of wall thickness or 13-mm, whichever is greater. Further variation is permissible so long as the cover in the final position is no less than 13-mm (0.5-in. per ASTM) and the TEBT strength classification requirements are met. To explore the significance of cage positioning, analysis was carried out on single and double-cage RCP models by shifting the inner steel-cage in the vertical plane. Without changing the cage diameter, inner-cages were shifted vertically along the loading direction at 10%, 15%, and 20% of wall thickness of the corresponding RCP model.

Figure 4.20 presents the load-deflection data for the FEMs after translating the inner steel-cage downwards vertically away from the obvert. According to the numerical models, cage shift had significant effect on the load-deflection output of the 825-mm and 1200-mm 65D RCP models. However, inelastic load-deflection behavior for the remaining models was found to be sensitive to cage positioning. Cage-shift was more influential in higher strength class models, since with larger steel areas, the contribution of the cage to load capacity is more significant. Offsetting the inner steel-cage seemed to improve the load-bearing capacity in some cases, especially for the 140D models (**Fig. 4.20,** c & f).

Figure 4.21 illustrates the effects of cage positioning on D_{ult}-load. As mentioned, cage shift did not significantly influence the behavior of both 65D models. For the 825-mm 140D double-cage model, shifting the inner cage downwards caused D_{ult} to decrease. This contrasts with remaining 100D and 140D models, where offsetting the inner cage downwards by 10% of wall thickness increased D_{ult}, but further offsets caused D_{ult} to decrease.

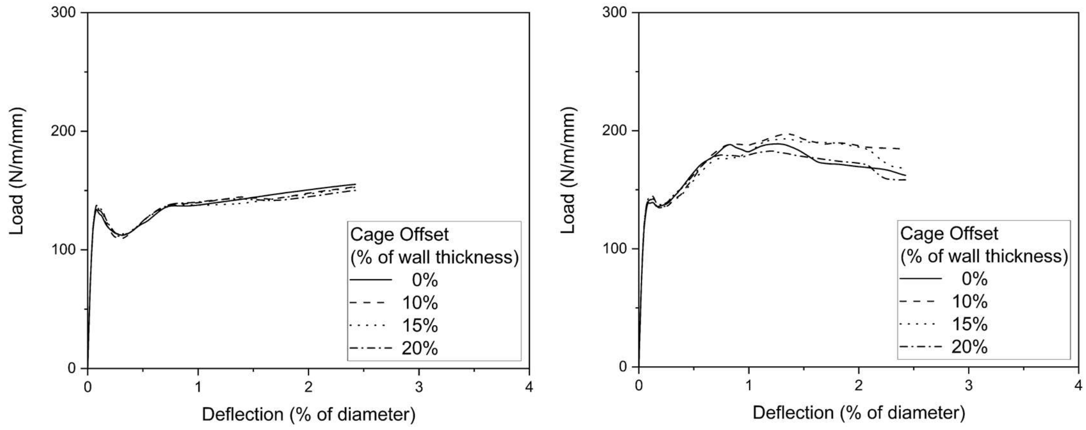

(a) 825-mm 65D

(b) 825-mm 100D

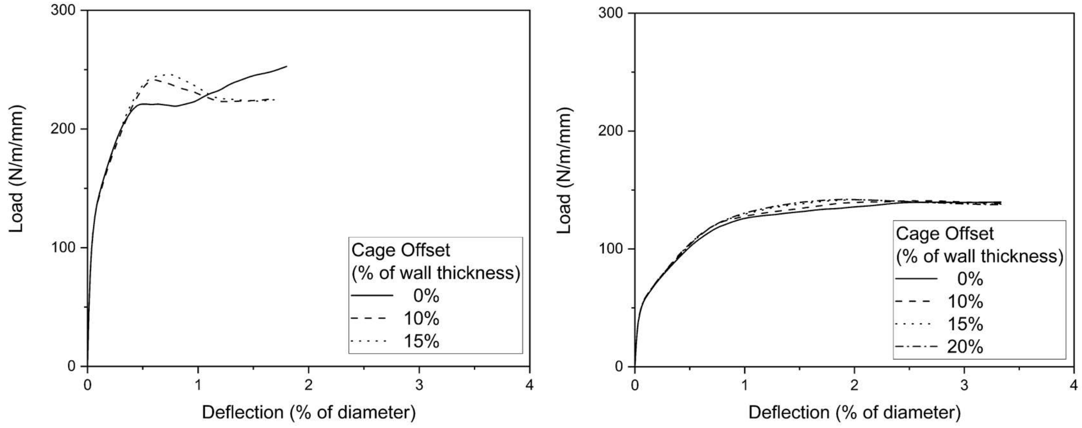

(c) 825-mm 140D

(d) 1200-mm 65D

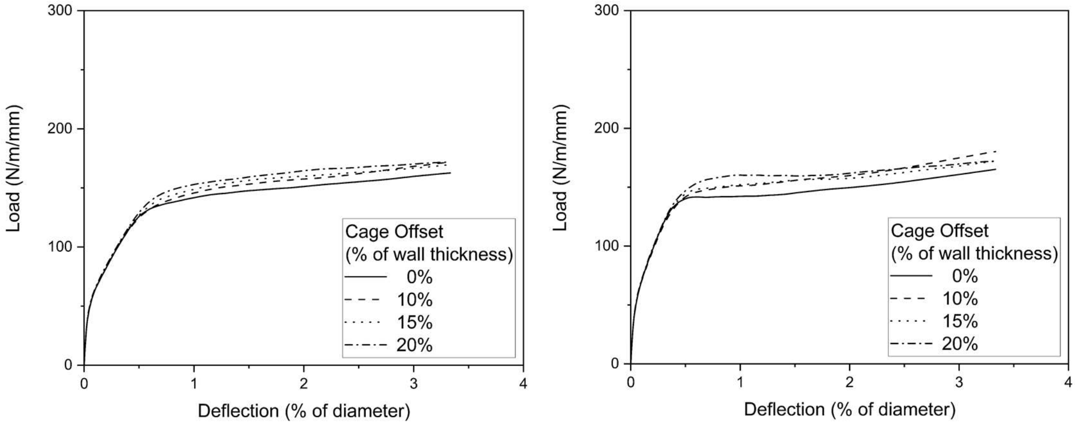

(e) 1200-mm 100D

(f) 1200-mm 140D

Figure 4.20: Effect of vertically offsetting the inner steel cage on load-deflection profiles of all models.

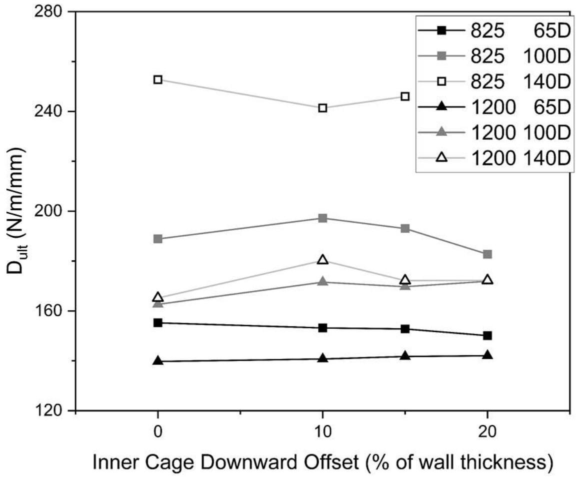

Figure 4.21: Effect of shifting inner cage downwards on D_{ult} for all models.

Lowering the inner cage in the vertical plane caused reinforcement depth to increase at the obvert but decrease at the invert. Since the flexural capacity of RCP is proportional to reinforcement depth (Heger, 1963), this caused the moment-bearing capacity of the obvert-section to increase, while the moment-bearing capacity of the invert-section decreased. In RCP where the invert governs ultimate failure, offsetting the cage decreased D_{ult} due to the lower reinforcement depth at the invert section as observed in the 825-mm 140D double-cage model. During the TEBT, cracking tended to occur on the invert before the obvert due to the invert resisting the pipe own-weight in addition to the TEBT load. However, ultimate failure was not always governed by the invert. In some cases, obvert moments could be more severe than invert moments due to loading being concentrated along a single bearing rather than being distributed between two bearings. In cases where the obvert governed D_{ult}, shifting the steel cage towards the invert could initially improve D_{ult} by increasing obvert moment capacity. However, shifting the cage excessively could lead to invert capacity decreasing to a point where the obvert no longer governed D_{ult}, as in the 1200-mm 100D & 140D models. Generally, model results suggest that the effect of cage-shift during the manufacturing process is unlikely to be a significant cause of concern, so long as the offset is within 10% of wall thickness.

4.5 Conclusions

In this chapter, nonlinear 3D FEMs for RCP undergoing the TEBT were developed using ABAQUS. FEMs were produced representing two 825-mm single-cage, one 825-mm and three 1200-mm double-cage, and one 1800-mm triple-cage RCP specimens of different strength classes. The numerical models were calibrated and validated based on load-deflection results gathered by the authors in previous experimental studies. Load-deflection data extracted from the models closely reproduced the experimental load-deflection results throughout the elastic and inelastic phases. Stress behavior of the concrete suggested good agreement with experimental observations. The models also provided insight into the state of stress in the steel reinforcement, which is not readily observable during the TEBT due to the concrete cover. A parametric study was successfully conducted to quantify the effects of reinforcement area, reinforcement yield strength, reinforcement cover. The following conclusions can be drawn based on the results:

1. Reinforcement area greatly influenced the post-crack RCP load-deflection relationship due to steel reinforcement contributing more significantly to the behavior of cracked sections. Steel reinforcement greatly affected D_{ult} for all models, as well as the service loads D_{peak} (single-cage) and $D_{\delta=0.36\%}$ (double-cage). In double-cage RCP models, the outer steel cage contributed to D_{ult}, and the 1200-mm RCP with an inner/outer reinforcement ratio of 60%/40% performed more efficiently than that with inner/outer reinforcement ratio of 70%/30%.
2. Reinforcement yield strength affected the post-crack behavior rather than the pre-crack behavior, as steel reinforcement is unlikely to yield before substantial cracking in concrete. The effect of steel yield was less pronounced in RCP models with higher reinforcement where yielding is unlikely to occur before shear failure. While increasing the steel yield from 450 MPa initially caused significant increase in D_{ult}, this became less significant past steel yields of 550 MPa for most models.
3. Concrete cover to the inner steel cage greatly influenced the service performance of the models. By reducing the cover distance to the inner face, the steel reinforcement

was more favorably placed in the tension zone. This finding also indicates the importance maintaining the cage dimensional tolerance during RCP fabrication.

4. Results suggest that translating the inner reinforcement cage downwards along the vertical by 10% of the RCP wall thickness would increase the ultimate load capacity of some 100D and 140D models, although further offsets reduced capacity. This is likely due to the increased moment-bearing capacity of the obvert after cage-shift initially improving performance. Change in capacity was not significant to warrant concern over cage-shift caused by manufacturing processes, assuming the CSA & ASTM guidelines on permissible deviation of cage positioning are met.

4.6 References

Abaqus Analysis User's Guide (6.13). (2013). Dassault Systèmes Simulia Corp. http://dsk.ippt.pan.pl/docs/abaqus/v6.13/books/usb/default.htm?startat=pt05ch23s06.html

ACPA. (2016). *Precast Concrete Pipe Durability* (Resource No. 02–712; Concrete Pipe Information). American Concrete Pipe Association. http://www.concretepipe.org

Alfarah, B., López-Almansa, F., & Oller, S. (2017). New methodology for calculating damage variables evolution in Plastic Damage Model for RC structures. *Engineering Structures*, *132*, 70–86. https://doi.org/10.1016/j.engstruct.2016.11.022

ASTM A36/A36M. (2019). *Specification for Carbon Structural Steel*. ASTM International. https://doi.org/10.1520/A0036_A0036M-19

ASTM A615/A615M. (2018). *Specification for Deformed and Plain Carbon-Steel Bars for Concrete Reinforcement*. ASTM International. https://doi.org/10.1520/A0615_A0615M-18E01

ASTM A706/706M. (2016). *Specification for Deformed and Plain Low-Alloy Steel Bars for Concrete Reinforcement*. ASTM International. https://doi.org/10.1520/A0706_A0706M-16

ASTM A1064/A1064M. (2018). *Specification for Carbon-Steel Wire and Welded Wire Reinforcement, Plain and Deformed, for Concrete*. ASTM International. https://doi.org/10.1520/A1064_A1064M-18A

ASTM C76. (2016). *Specification for Reinforced Concrete Culvert, Storm Drain, and Sewer Pipe*. ASTM International. https://doi.org/10.1520/C0076-16

Comite Euro-International Du Beton. (1993). *CEB-FIP MODEL CODE 1990*. Thomas Telford Publishing. https://doi.org/10.1680/ceb-fipmc1990.35430

CSA A257. (2014). *Standards for Concrete Pipe and Manhole Sections* (p. 92). CSA Group.

de la Fuente, A., Escariz, R. C., de Figueiredo, A. D., Molins, C., & Aguado, A. (2012). A new design method for steel fibre reinforced concrete pipes. *Construction and Building Materials*, *30*, 547–555. https://doi.org/10.1016/j.conbuildmat.2011.12.015

de la Fuente, A., Figueiredo, A. D. de, Aguado, A., Molins, C., & Chama Neto, P. J. (2012). Steel fiber reinforced concrete pipes. Part 2: Numerical model to simulate the crushing test. *Revista IBRACON de Estruturas e Materiais*, *5*(1), 12–25. https://doi.org/10.1590/S1983-41952012000100003

Dahmani, L. & Khennane, A. (2010). Crack identification in reinforced concrete beams using ANSYS software. *Strength of Materials*, *42*(2), 232-240.

Demir, A., Ozturk, H., & Dok, G. (2016). 3D Numerical Modeling of RC Deep Beam Behavior by Nonlinear Finite Element Analysis. *Disaster Science and Engineering*, *2*(1), 13–18.

Ferrado, F. L., Escalante, M. R., & Rougier, V. C. (2016). Numerical Simulation of the Three Edge Bearing Test of Steel Fiber Reinforced Concrete Pipes. *Mecánica Computacional*, *34*, 2329–2341.

Hamedani, R. N., & Esfahani, M. S. (2012). *Numerical Evaluation of Structural Behavior of the Simply Supported FRP-RC Beams*.

Heger, F. (1963). Structural Behavior of Circular Reinforced Concrete Pipe-Development of Theory. *ACI Journal Proceedings*, *60*(11). https://doi.org/10.14359/7905

Kataoka, M. N., da Silva, J. L., de Oliveira, L. M. F., & El Debs, M. K. (2017). FE analysis of RC pipes under three-edge-bearing test: Pocket and diameter influence. *Computers and Concrete*, *20*(4), 483–490. https://doi.org/10.12989/CAC.2017.20.4.483

Kmiecik, P., & Kamiński, M. (2011). Modelling of reinforced concrete structures and composite structures with concrete strength degradation taken into consideration. *Archives of Civil and Mechanical Engineering*, *11*(3), 623–636. https://doi.org/10.1016/S1644-9665(12)60105-8

Massenzio, M., Jacquelin, E., & Ovigne, P. A. (2005). Natural frequency evaluation of a cracked RC beam with or without composite strengthening for a damage assessment. *Materials and Structures*, 11.

Meira, G. R., Andrade, C., Alonso, C., Borba, J. C., & Padilha, M. (2010). Durability of concrete structures in marine atmosphere zones – The use of chloride deposition rate on the wet candle as an environmental indicator. *Cement and Concrete Composites*, *32*(6), 427–435. https://doi.org/10.1016/j.cemconcomp.2010.03.002

Michał, S., & Andrzej, W. (2015, August 25). *Calibration of the CDP model parameters in Abaqus*. Advances in Structural Engineering and Mechanics (ASEM15), Incheon, Korea.

Mohamed, N., & Nehdi, M. L. (2016). Rational finite element assisted design of precast steel fibre reinforced concrete pipes. *Engineering Structures*, *124*, 196–206. https://doi.org/10.1016/j.engstruct.2016.06.014

Riahi, E. (2016). *Evaluation of Structural Capacity of Epoxy-Coated Concrete Pipes and its Interaction with Soil*. University of Texas Arlinton.

Tehrani, A. D. (2016). *Finite Element Analysis for ASTM C-76 Reinforced Concrete Pipes with Reduced Steel Cage*. University of Texas Arlington.

Chapter 5

Conclusions and Recommendations

5.1 Summary and Conclusions

The present thesis is a compilation of three studies conducted to advance industry and academic knowledge in the subject of reinforced concrete pipe (RCP) load-deflection behaviour under Three-Edge Bearing Test (TEBT) loading, with the goal of assessing whether this behaviour can be used to define RCP class.

In Chapter 2, a review was conducted on the history of reinforced concrete pipe strength tests, the origins of the TEBT crack measurement criterion, and the state-of-the-art TEBT developments. Among preliminary pipe strength tests, the TEBT was found to be superior due to its ease of operation when compared to the sand-bearing and two-edge bearing tests. For that reason, the TEBT has seen widespread use in concrete pipe industries on a global scale for the past hundred years and is expected to endure for the foreseeable future. However, a major limitation of the TEBT is the reliance on human judgement in identifying the load at which a 0.3-mm-wide, 300-mm-long crack occurs. This criterion induces subjectivity and error, preventing reliable comparison of TEBT results between separate test operators or RCP manufacturers. Furthermore, this criterion was found to have been arbitrarily selected, without definite implications on structural capacity or performance. The existing literature has seen an increasing use of deflection sensors with the TEBT to assess pipe performance based on load-deflection behaviour. However, the current research tends to emphasize steel-fibre RCP (SFRCP) rather than the more commonly used cage RCP. There is a lack of research exploring the possibility of replacing the TEBT crack measurement criterion with load-deflection based criteria for RCP, especially for triple-cage RCP.

In Chapter 3, an extensive experimental study was conducted in which over 40 full-scale RCP specimens instrumented with precision displacement sensors were subjected to the TEBT. Specimens were selected to cover a wide range of standard RCP industry sizes, with diameters ranging from just 450-mm to upwards of 2000-mm. Depending on size and strength class, RCP specimens were manufactured with single, double, or triple-cage steel reinforcement configuration, which are the most commonly used in RCP industry. Load-deflection behaviour patterns were found to be largely similar for RCP specimens of the same cage configuration, regardless of the specimen size. Single and triple-cage load-deflection patterns formed easily discernible peaks signaling the end of elastic deformation, after which the applied load momentarily drops and begins to regain strength in the plastic phase. Based on these peak-loads, a new capacity-driven criterion termed D_{peak} is suggested as an alternative to the arbitrary crack-based $D_{0.3}$ criterion of the TEBT. In the case of double-cage RCP, load-deflection patterns did not form clear peaks, suggesting a more ductile transition from elastic to inelastic behaviour. Instead, the possibility of using a deflection-limit based criterion, referred to as D_{δ}, was investigated. Different deflection limits were considered and compared to $D_{0.3}$. Ultimately, for double-cage RCP it was found that the load at a deflection of 0.36% of total diameter ($D_{\delta = 0.36\%}$) yields the highest correlation with $D_{0.3}$. Based on these results, $D_{\delta = 0.36\%}$ is suggested as a non-disruptive alternative for $D_{0.3}$ for double-cage RCP. The two D-load criteria suggested in this study can vastly improve current TEBT testing by providing both industry and academia with specific measurements that eliminate any uncertainty caused by human measurement.

In Chapter 4, nonlinear 3D finite-element models (FEMs) were developed for single, double, and triple-cage representative RCP. Up-to-date concrete damaged plasticity (CDP) theory was used to generate the constitutive material model for the concrete elements. Using CDP algorithms enabled the modelling of elastic as well as plastic behaviour. After calibrating the tension stiffening parameters, the FEMs showed high agreement with Chapter 3 load-deflection results. The models also provided insight into the state of stresses in the concrete material and steel reinforcement during TEBT loading, supporting some experimental observations. Using the single and double-cage models, a thorough reinforcement-based parametric study was conducted to investigate the effects of certain reinforcement parameters on the D-load criteria suggested in the previous chapter. The reinforcement area and cover were found to significantly influence D_{peak} and $D_{\delta = 0.36\%}$, while the effect of yield strength and cage position was instead more pronounced on D_{ult}.

5.2 Recommendations for Future Work

The studies performed in this thesis indicate a need for additional experimental and numerical analysis in the following topics:

1) Chapter 3 suggested modified *D*-load criteria for unlined RCP undergoing the TEBT based on a sample size of around 40 specimens. Further studies should seek to increase that sample size to validate the suggested *D*-load criteria.
2) There is a lack of consideration of triple-cage RCP with/without stirrups in existing research. Future work should seek to further examine the behaviour of triple-cage RCP, as well as investigate the effect of different levels of stirrup reinforcement on the load-deflection behaviour of triple-cage RCP.
3) A key advantage of eliminating the crack-measurement criteria is enabling the testing of lined RCP without requiring the lining to be stripped. Future experimental studies should explore the load-deflection behaviour of lined RCP and assess the possibility of applying the suggested *D*-load measures.
4) In Chapter 4, a triple-cage RCP model was developed for an 1800-mm pipe, and the state of stress in concrete and steel was discussed. It is recommended that a similar model be developed for a triple-cage RCP with stirrups to investigate the effect of stirrups on stress distribution in the concrete and steel material.
5) The FEMs developed in Chapter 4 and the subsequent parametric study offer a good basis for future numerical work involving RCP. Future work should seek to expand the range of diameters considered in the parametric study. Triple-cage RCP with/without stirrups should also be included in parametric studies.
6) In Chapter 4, the ratio of reinforcement between the inner and outer cages in double-cage RCP was found to significantly influence the ultimate load capacity of the pipe. Future studies should investigate the effect of different inner-to-outer reinforcement ratios for double and triple-cage RCP.

Appendices

Appendix A: Load-deflection TEBT reports of single-cage RCP specimens

THREE-EDGE BEARING TEST REPORT

Test Date	07/09/2018		**Mfg. Date**	28/08/2018		**Test ID**	1
Pipe Size	450		**Class**	140D		**Length**	2.44 m
Actual Size	457.2					**Wall**	83 mm
Cage Design:			**RFT Area**				
Inner:	W4.5	**@** 100	290 mm2			**As Inner:**	290 mm2
Outer:		**@**	0 mm2			**As Outer:**	0 mm2
Elliptical:		**@**	0 mm2				
						Age:	9 days
Hairline:	kN	0.0 N/m/mm	(Obsv.)			**Cover:**	mm
M. Hairline:	kN	0.0 N/m/mm	(Obsv.)			**f'c:**	40 MPa (design)
0.3-mm DL:	254 kN	227.9 N/m/mm	(Obsv.)			**Equivalent Class:**	227.9 D
Ultimate:	416.5 kN	373.6 N/m/mm	**UL/0.3DL:**	164%			

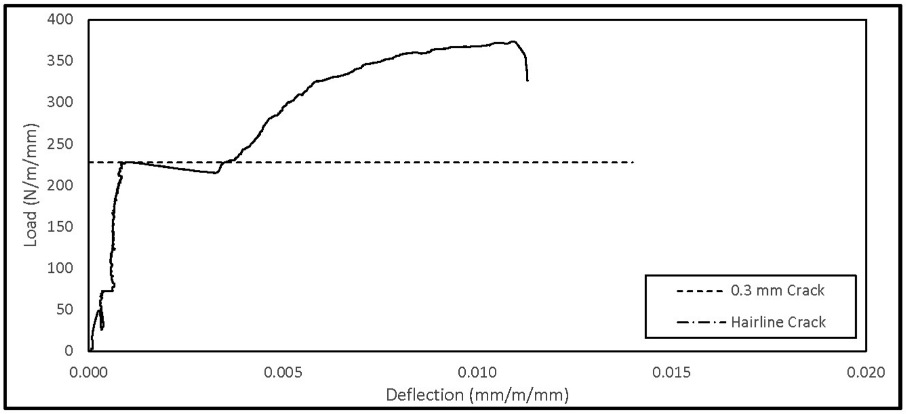

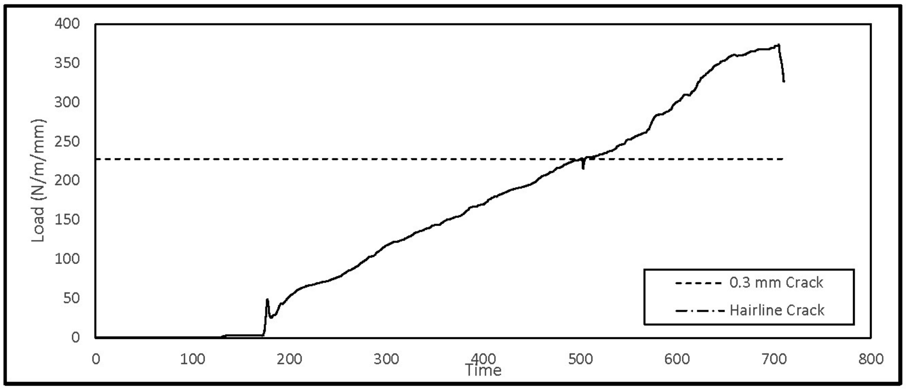

THREE-EDGE BEARING TEST REPORT

Test Date	07/09/2018	**Mfg. Date**	30/08/2018	**Test ID**	2
Pipe Size	525	**Class**	140D	**Length**	2.44 m
Actual Size	533.4			**Wall**	89 mm

Cage Design: **RFT Area**

Inner:	W4.5 @ 100	290 mm2	**As Inner:**	290	mm2
Outer:	@	0 mm2	**As Outer:**	0	mm2
Elliptical:	@	0 mm2			

Age: 7 days

Hairline:	kN	0.0 N/m/mm	(Obsv.)	**Cover:**	mm
M. Hairline:	kN	0.0 N/m/mm	(Obsv.)	**f'c:**	40 MPa (design)
0.3-mm DL:	244 kN	187.6 N/m/mm	(Obsv.)	**Equivalent Class:**	187.6 D
Ultimate:	340.4 kN	261.7 N/m/mm	**UL/0.3DL:**	140%	

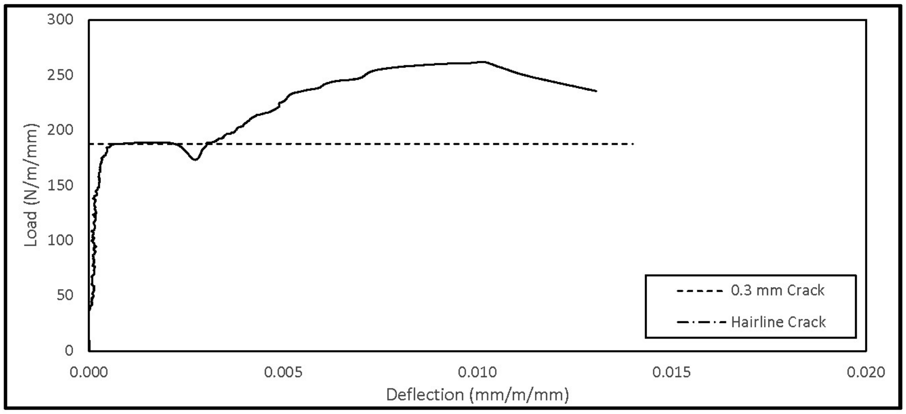

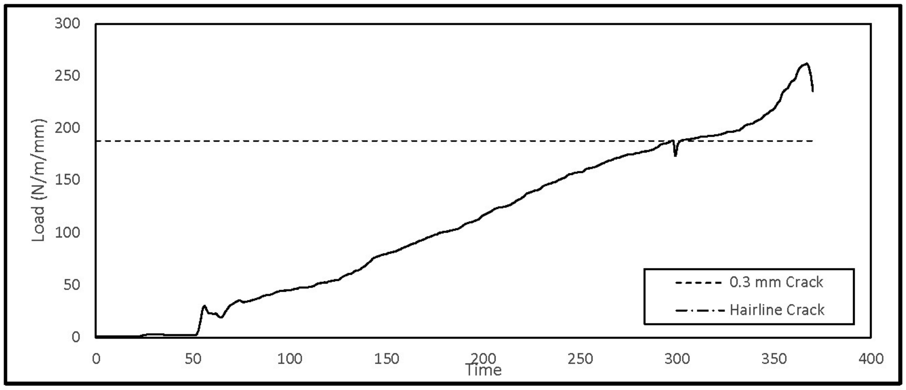

THREE-EDGE BEARING TEST REPORT

Test Date	07/09/2018	**Mfg. Date**	18/11/2016	**Test ID**	3	
Pipe Size	675	**Class**	140D	**Length**	2.44	m
Actual Size	685.8			**Wall**	102	mm

Cage Design: **RFT Area**

Inner:	W4.5	**@**	45	645 mm2	**As Inner:**	645	mm2
Outer:		**@**		0 mm2	**As Outer:**	0	mm2
Elliptical:		**@**		0 mm2			

Age: 658 days

Hairline:	213 kN	127.4 N/m/mm	(Obsv.)	**Cover:**		mm
M. Hairline:	kN	0.0 N/m/mm	(Obsv.)	**f'c:**	40	MPa (design)
0.3-mm DL:	247 kN	147.7 N/m/mm	(Obsv.)	**Equivalent Class:**	147.7 D	
Ultimate:	360.4 kN	215.6 N/m/mm	**UL/0.3DL:**	146%		

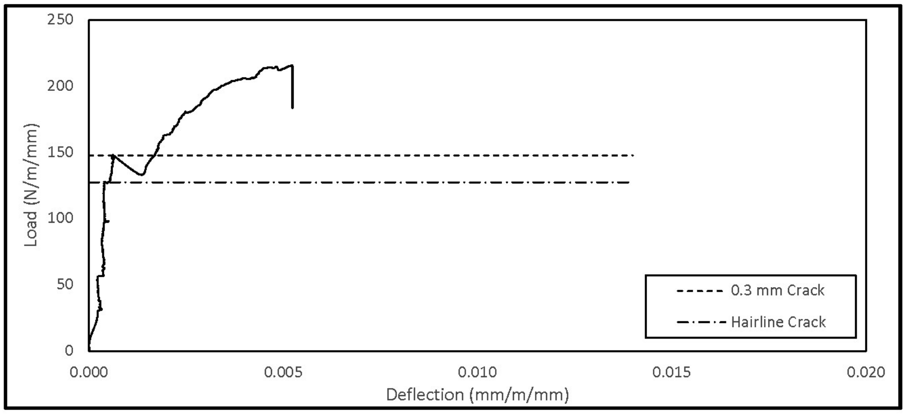

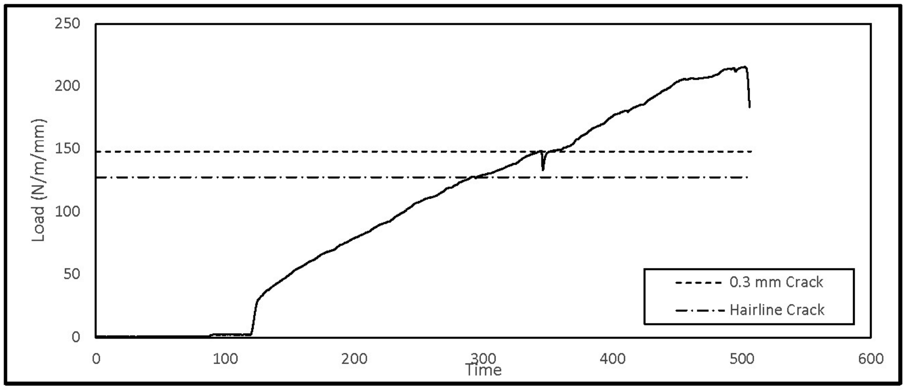

THREE-EDGE BEARING TEST REPORT

Test Date 11/09/2018 **Mfg. Date** 14/09/2016 **Test ID** 5
Pipe Size 600 **Class** 140D **Length** 2.44 m
Actual Size 609.6 **Wall** 95 mm

Cage Design: **RFT Area**
Inner: W4.5 **@** 60 484 mm2 **As Inner:** 484 mm2
Outer: **@** 0 mm2 **As Outer:** 0 mm2
Elliptical: **@** 0 mm2
Age: 727 days

Hairline: kN 0.0 N/m/mm (Obsv.) **Cover:** mm
M. Hairline: kN 0.0 N/m/mm (Obsv.) **f'c:** 40 MPa (design)
0.3-mm DL: 247 kN 166.2 N/m/mm (Obsv.) **Equivalent Class:** 166.2 D
Ultimate: 341.3 kN 229.6 N/m/mm **UL/0.3DL:** 138%

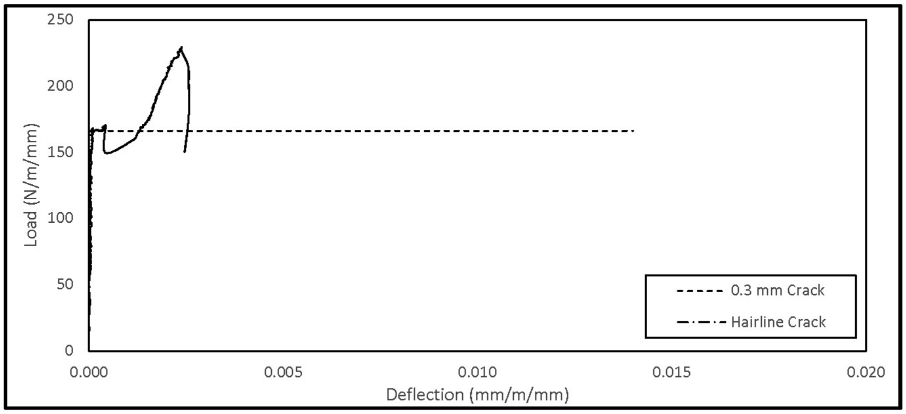

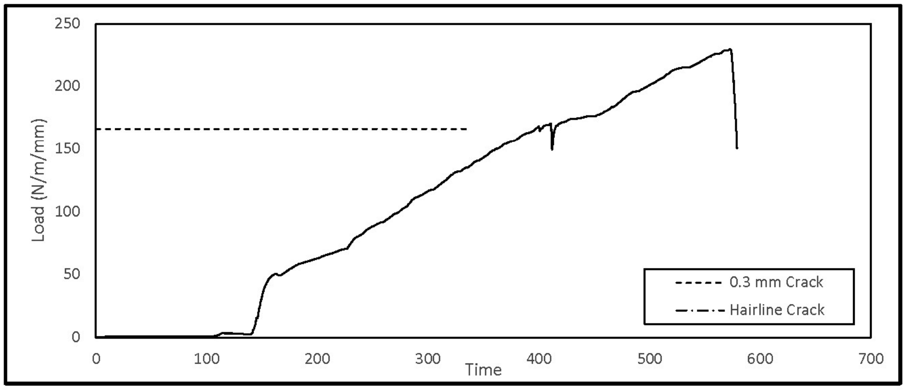

THREE-EDGE BEARING TEST REPORT

Test Date	11/09/2018	**Mfg. Date**	14/09/2016	**Test ID**	6
Pipe Size	600	**Class**	140D	**Length**	2.44 m
Actual Size	609.6			**Wall**	95 mm

Cage Design:

			RFT Area			
Inner:	W4.5	@ 60	484 mm2	**As Inner:**	484	mm2
Outer:		@	0 mm2	**As Outer:**	0	mm2
Elliptical:		@	0 mm2			

Age: 727 days

Hairline:	kN	0.0 N/m/mm	(Obsv.)	**Cover:**	mm
M. Hairline:	kN	0.0 N/m/mm	(Obsv.)	**f'c:**	40 MPa (design)
0.3-mm DL:	290 kN	195.1 N/m/mm	(Obsv.)	**Equivalent Class:**	181.4 D
Ultimate:	337.1 kN	226.8 N/m/mm	**UL/0.3DL:**	116%	

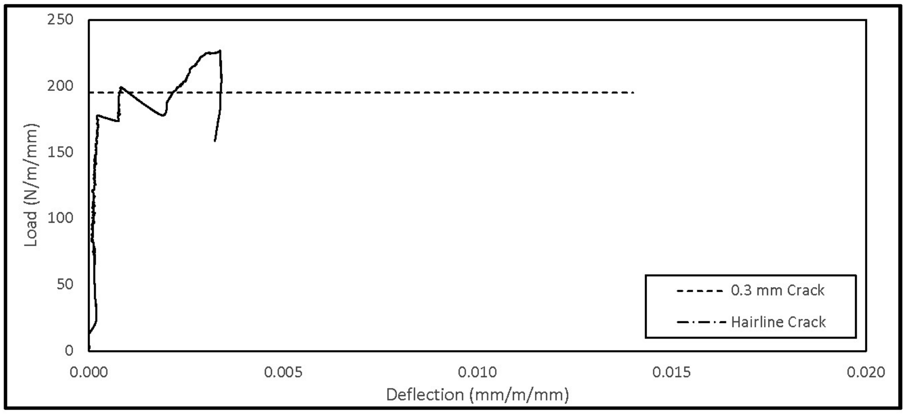

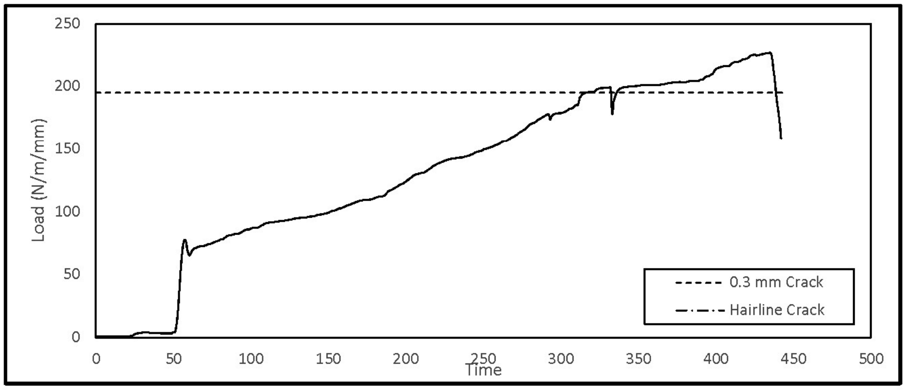

THREE-EDGE BEARING TEST REPORT

Test Date 11/09/2018 **Mfg. Date** 18/11/2016 **Test ID** 7

Pipe Size 675 **Class** 140D **Length** 2.44 m

Actual Size 685.8 **Wall** 102 mm

Cage Design: **RFT Area**

Inner: W4.5 **@** 45 645 mm2 **As Inner:** 645 mm2

Outer: **@** 0 mm2 **As Outer:** 0 mm2

Elliptical: **@** 0 mm2

Age: 662 days

Hairline: 221 kN 132.2 N/m/mm (Obsv.) **Cover:** mm

M. Hairline: kN 0.0 N/m/mm (Obsv.) **f'c:** 40 MPa (design)

0.3-mm DL: 270 kN 161.5 N/m/mm (Obsv.) **Equivalent Class:** 161.5 D

Ultimate: 390.4 kN 233.5 N/m/mm **UL/0.3DL:** 145%

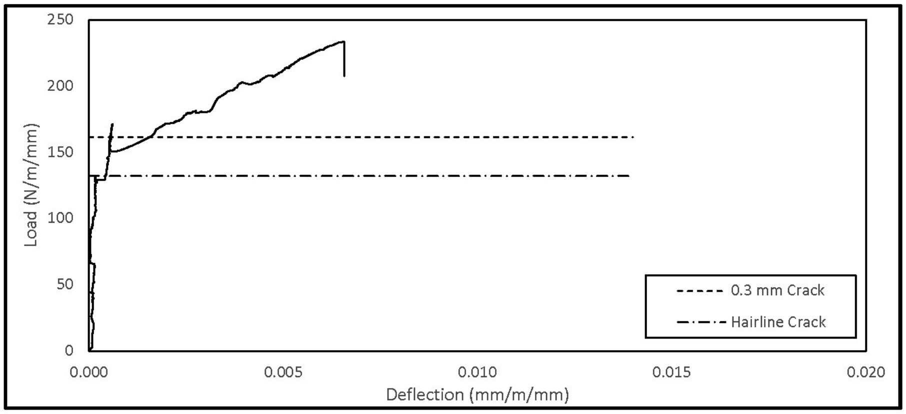

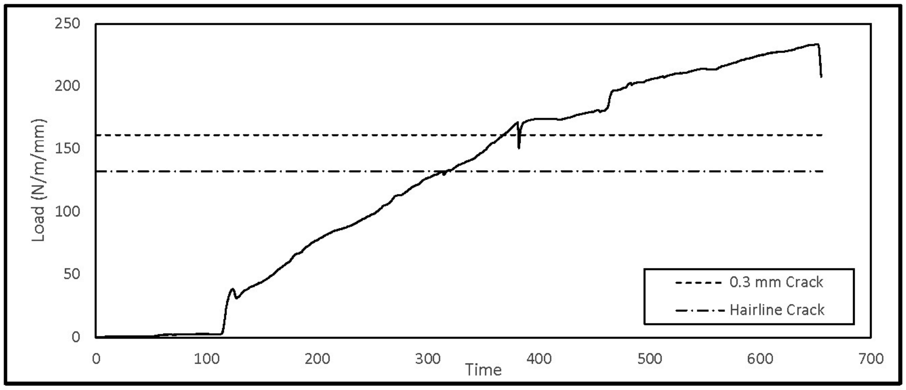

THREE-EDGE BEARING TEST REPORT

Test Date 13/09/2018 **Mfg. Date** 30/08/2018 **Test ID** 9
Pipe Size 525 **Class** 140D **Length** 2.44 m
Actual Size 533.4 **Wall** 89 mm

Cage Design: **RFT Area**
Inner: W4.5 **@** 100 290 mm2 **As Inner:** 290 mm2
Outer: **@** 0 mm2 **As Outer:** 0 mm2
Elliptical: **@** 0 mm2

Age: 13 days

Hairline: kN 0.0 N/m/mm (Obsv.) **Cover:** mm
M. Hairline: kN 0.0 N/m/mm (Obsv.) **f'c:** 40 MPa (design)
0.3-mm DL: 279 kN 214.5 N/m/mm (Obsv.) **Equivalent Class:** 207.9 D
Ultimate: 338 kN 259.9 N/m/mm **UL/0.3DL:** 121%

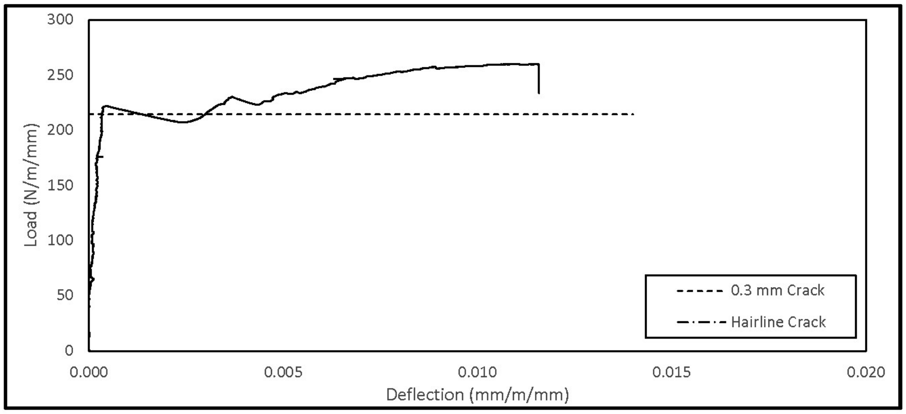

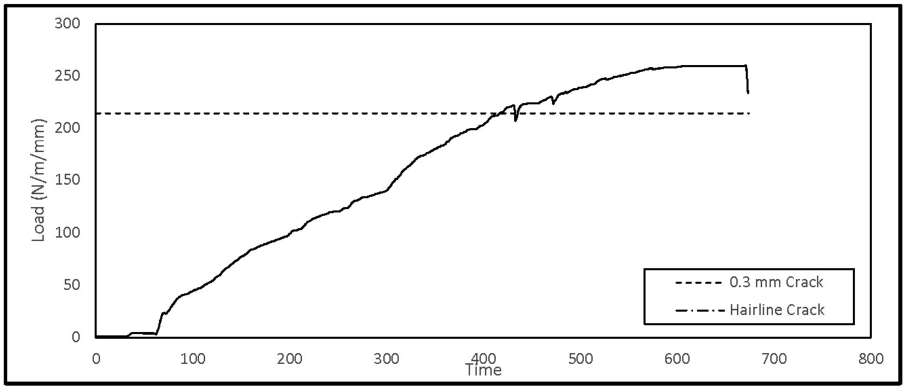

THREE-EDGE BEARING TEST REPORT

Test Date	13/09/2018	**Mfg. Date**	07/07/2018	**Test ID**	11
Pipe Size	750	**Class**	100D	**Length**	2.44 m
Actual Size	762.0			**Wall**	108 mm

Cage Design: **RFT Area**

Inner:	W4.5	@	70	415 mm2	**As Inner:** 415	mm2
Outer:		@		0 mm2	**As Outer:** 0	mm2
Elliptical:		@		0 mm2		

Age: 68 days

Hairline:	188 kN	101.2 N/m/mm	(Obsv.)	**Cover:**	mm
M. Hairline:	kN	0.0 N/m/mm	(Obsv.)	**f'c:**	30 MPa (design)
0.3-mm DL:	250 kN	134.6 N/m/mm	(Obsv.)	**Equivalent Class:**	129.3 D
Ultimate:	360.4 kN	194.0 N/m/mm	**UL/0.3DL:** 144%		

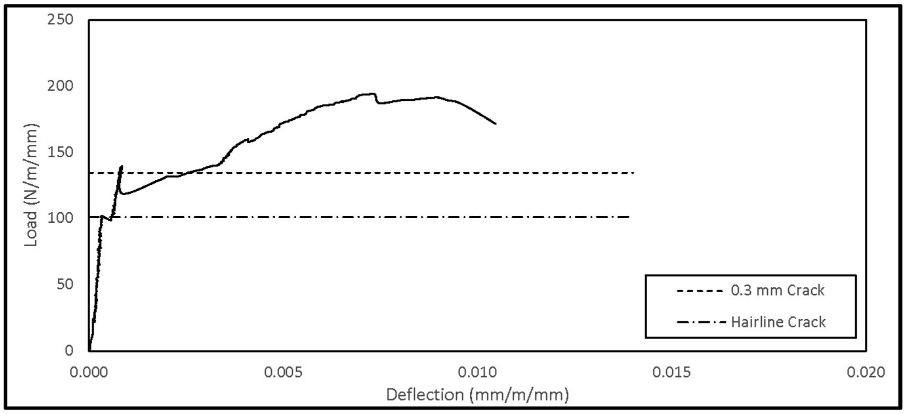

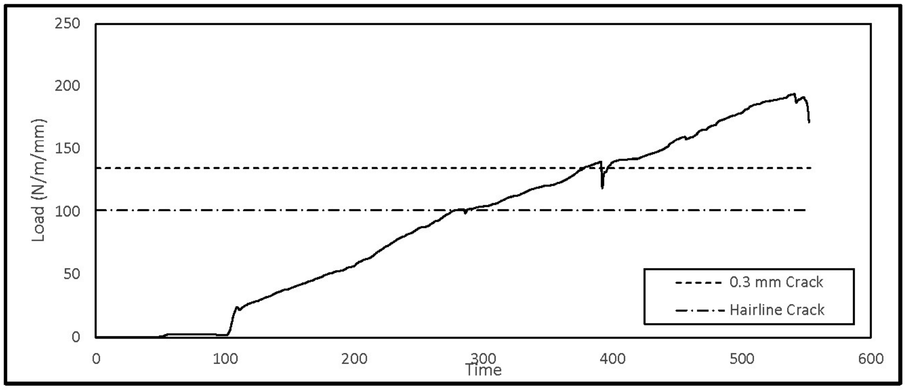

THREE-EDGE BEARING TEST REPORT

Test Date	13/09/2018	**Mfg. Date**	06/06/2018	**Test ID**	11
Pipe Size	825	**Class**	100D	**Length**	2.44 m
Actual Size	838.2			**Wall**	114 mm

Cage Design:			**RFT Area**		
Inner:	W4.5	**@** 60	484 mm2	**As Inner:**	484 mm2
Outer:		**@**	0 mm2	**As Outer:**	0 mm2
Elliptical:		**@**	0 mm2		
				Age:	99 days

Hairline:	204 kN	99.8 N/m/mm	(Obsv.)	**Cover:**	mm
M. Hairline:	kN	0.0 N/m/mm	(Obsv.)	**f'c:**	30 MPa (design)
0.3-mm DL:	259 kN	126.7 N/m/mm	(Obsv.)	**Equivalent Class:**	126.7 D
Ultimate:	394.6 kN	193.1 N/m/mm	**UL/0.3DL:** 152%		

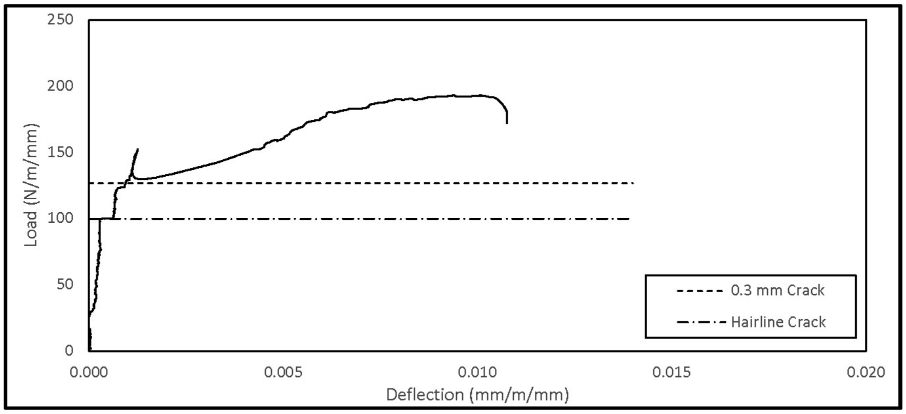

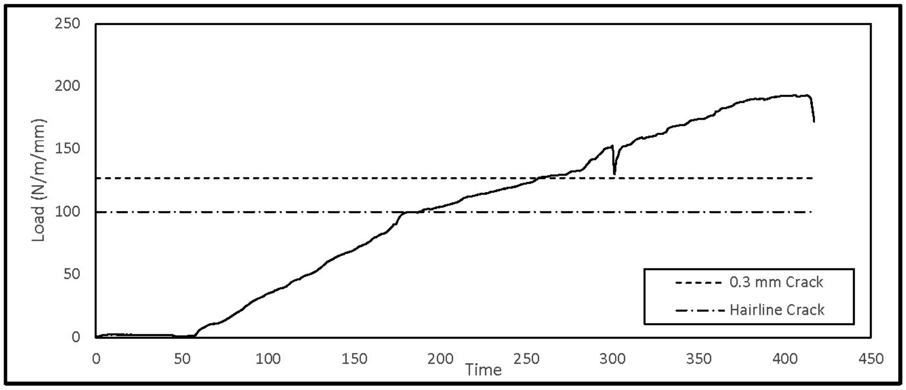

THREE-EDGE BEARING TEST REPORT

Test Date	24/06/2019	**Mfg. Date**	18/04/2019	**Test ID**	41
Pipe Size	750	**Class**	100D	**Length**	2.44 m
Actual Size	762.0			**Wall**	108 mm

Cage Design:			**RFT Area**		
Inner:	W4.5	**@** 70	415 mm2	**As Inner:**	415 mm2
Outer:		**@**	0 mm2	**As Outer:**	0 mm2
Elliptical:		**@**	0 mm2		
				Age:	67 days

Hairline:	195 kN	105.0 N/m/mm	(Obsv.)	**Cover:**	36.1 mm
M. Hairline:	kN	0.0 N/m/mm	(Obsv.)	**f'c:**	52.2 MPa (SH)
0.3-mm DL:	230 kN	123.8 N/m/mm	(Obsv.)	**Equivalent Class:**	123.8 D
Ultimate:	373.9 kN	201.3 N/m/mm	**UL/0.3DL:** 163%		F failure

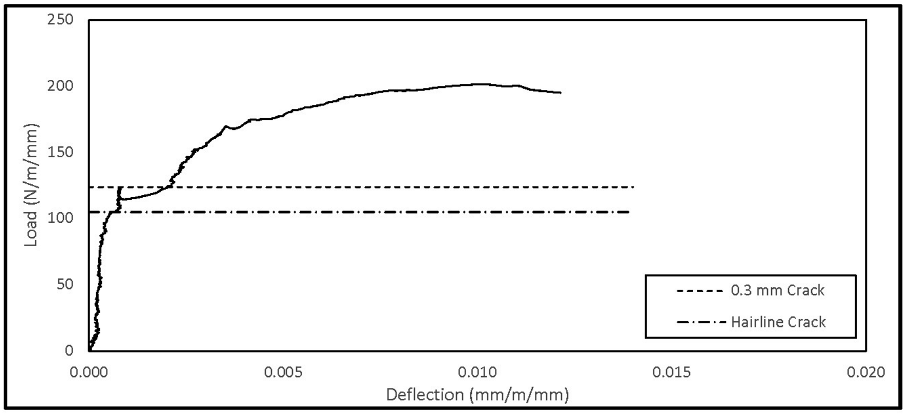

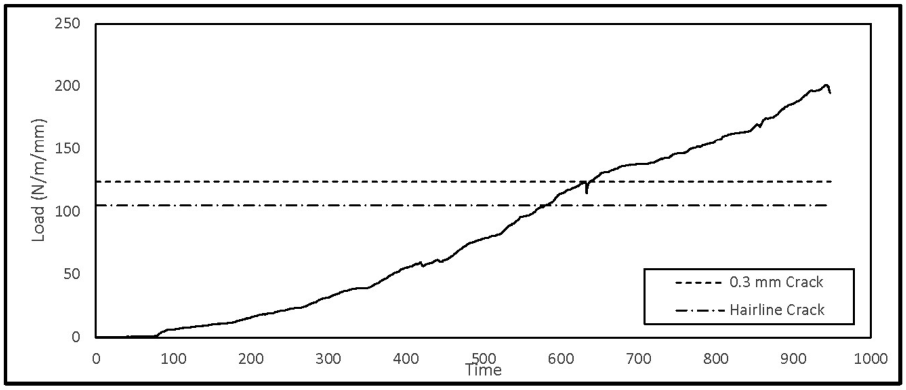

THREE-EDGE BEARING TEST REPORT

Test Date 24/6/2019 **Mfg. Date** 23/10/2018 **Test ID** 42
Pipe Size 825 **Class** 100D **Length** 2.44 m
Actual Size 838.2 **Wall** 114 mm

Cage Design: **RFT Area**
Inner: W4.5 @ 60 484 mm2 **As Inner:** 484 mm2
Outer: @ 0 mm2 **As Outer:** 0 mm2
Elliptical: @ 0 mm2

Age: 244 days

Hairline: 116 kN 56.8 N/m/mm (Obsv.) **Cover:** 39 mm
M. Hairline: 180 kN 88.1 N/m/mm (Obsv.) **f'c:** 51.9 MPa (SH)
0.3-mm DL: 218 kN 106.7 N/m/mm (Obsv.) **Equivalent Class:** 106.7 D
Ultimate: 378.4 kN 185.2 N/m/mm **UL/0.3DL:** 174% F fail

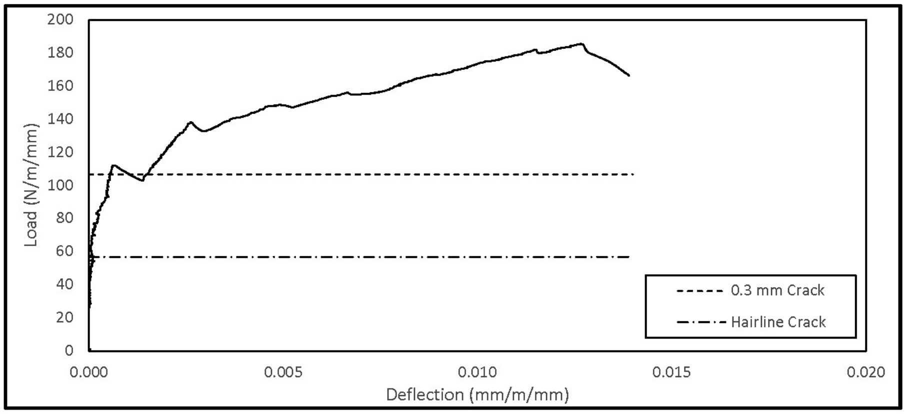

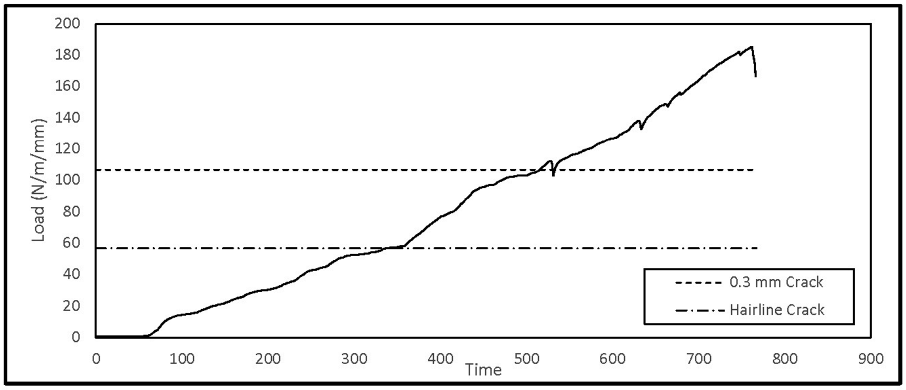

THREE-EDGE BEARING TEST REPORT

Test Date 12/08/2019 **Mfg. Date** 01/08/2019 **Test ID** 48
Pipe Size 825 **Class** 65D **Length** 2.44 m
Actual Size 838.2 **Wall** 114 mm

Cage Design: **RFT Area**
Inner: W4.5 @ 100 290 mm2 **As Inner:** 290 mm2
Outer: @ 0 mm2 **As Outer:** 0 mm2
Elliptical: @ 0 mm2

Age: 11 days

Hairline: kN 0.0 N/m/mm (Obsv.) **Cover:** 46.4 mm
M. Hairline: kN 0.0 N/m/mm (Obsv.) **f'c:** 42.2 MPa (SH)
0.3-mm DL: 275 kN 134.6 N/m/mm (Obsv.) **Equivalent Class:** 91.9 D
Ultimate: 281.7 kN 137.8 N/m/mm **UL/0.3DL:** 102% F fail

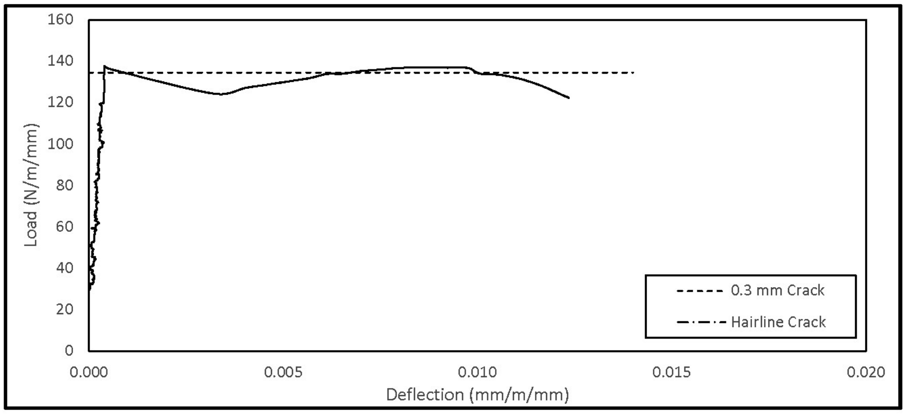

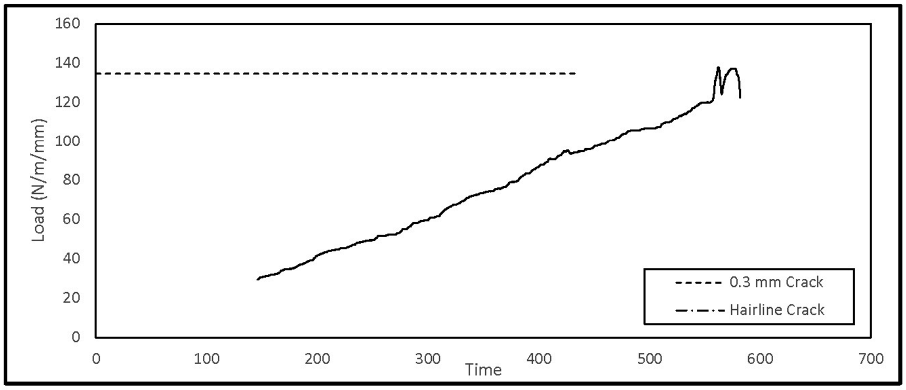

THREE-EDGE BEARING TEST REPORT

Test Date	12/08/2019	**Mfg. Date**	01/08/2019	**Test ID**	48
Pipe Size	825	**Class**	65D	**Length**	2.44 m
Actual Size	838.2			**Wall**	114 mm

Cage Design:				**RFT Area**		
Inner:	W4.5	@	100	290 mm2	**As Inner:**	290 mm2
Outer:		@		0 mm2	**As Outer:**	0 mm2
Elliptical:		@		0 mm2		

Age: 11 days

Hairline:	kN	0.0 N/m/mm	(Obsv.)	**Cover:**	45.3 mm
M. Hairline:	kN	0.0 N/m/mm	(Obsv.)	**f'c:**	41 MPa (SH)
0.3-mm DL:	261 kN	127.7 N/m/mm	(Obsv.)	**Equivalent Class:**	95.8 D
Ultimate:	293.7 kN	143.7 N/m/mm	**UL/0.3DL:** 113%		F fail, sudden DL no HL

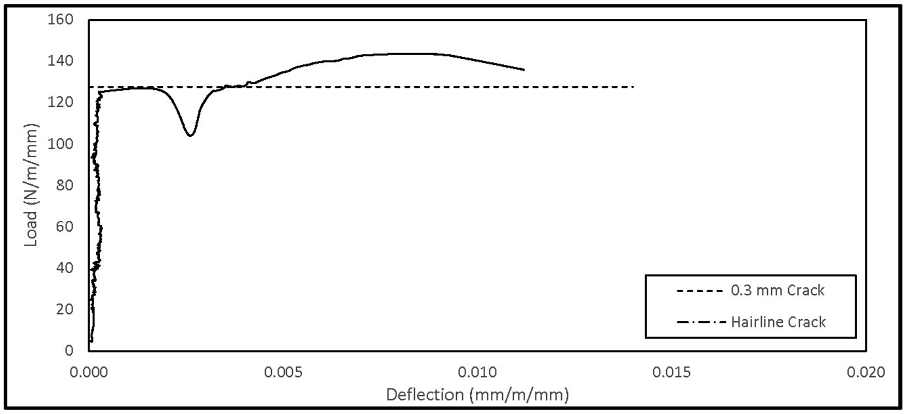

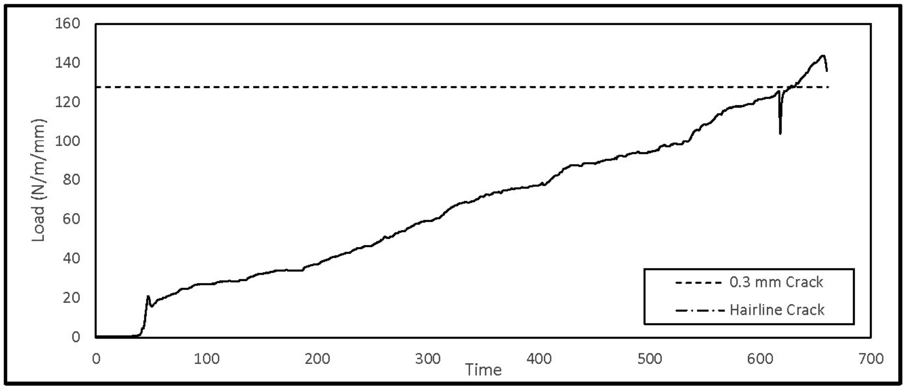

Appendix B: Load-deflection TEBT reports of double-cage RCP specimens

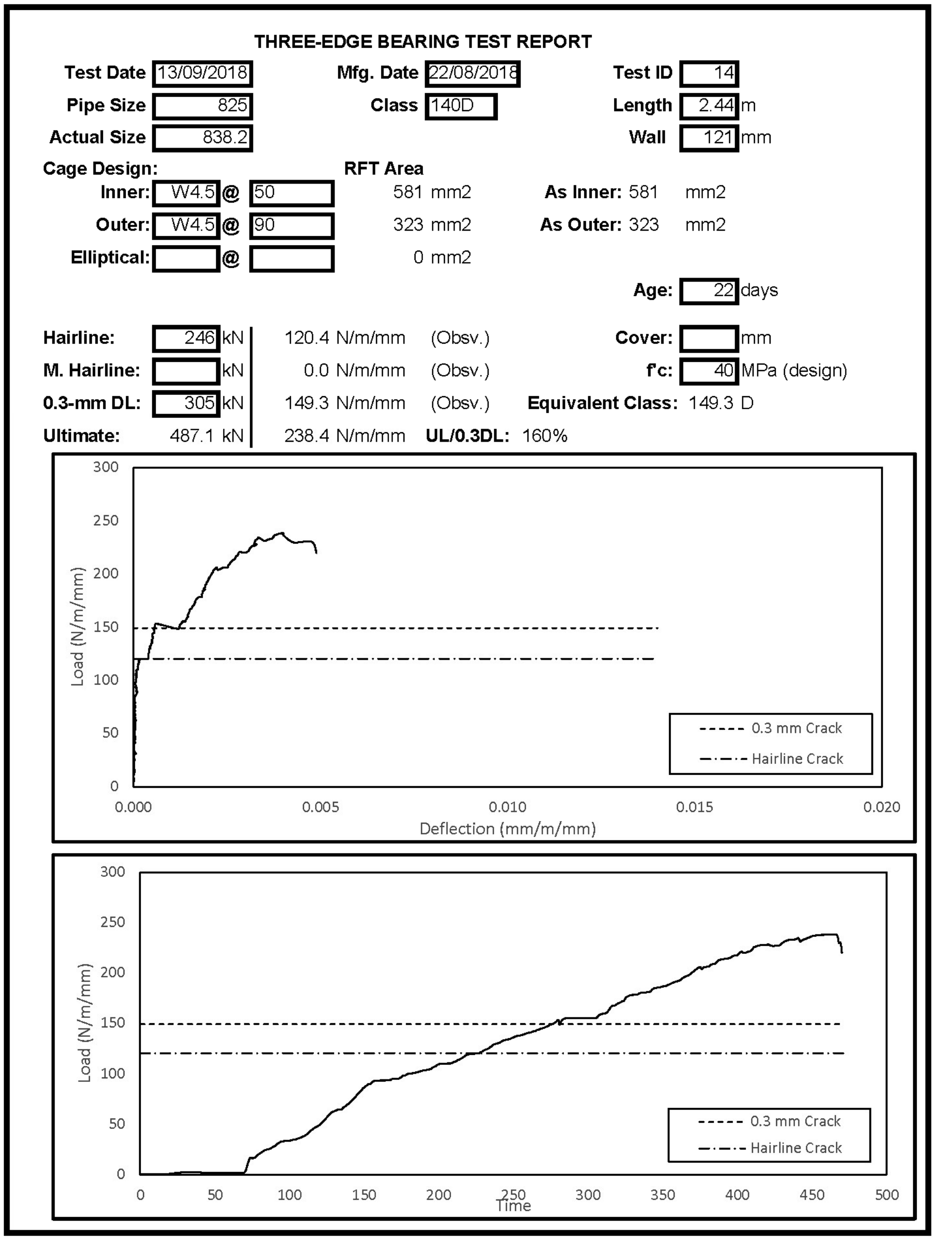

THREE-EDGE BEARING TEST REPORT

Test Date	13/09/2018	**Mfg. Date**	22/08/2018	**Test ID**	14
Pipe Size	825	**Class**	140D	**Length**	2.44 m
Actual Size	838.2			**Wall**	121 mm

Cage Design:		**RFT Area**		
Inner:	W4.5 **@** 50	581 mm2	**As Inner:** 581	mm2
Outer:	W4.5 **@** 90	323 mm2	**As Outer:** 323	mm2
Elliptical:	**@**	0 mm2		
			Age:	22 days

Hairline:	246 kN	120.4 N/m/mm	(Obsv.)	**Cover:**	mm
M. Hairline:	kN	0.0 N/m/mm	(Obsv.)	**f'c:**	40 MPa (design)
0.3-mm DL:	305 kN	149.3 N/m/mm	(Obsv.)	**Equivalent Class:**	149.3 D
Ultimate:	487.1 kN	238.4 N/m/mm	**UL/0.3DL:** 160%		

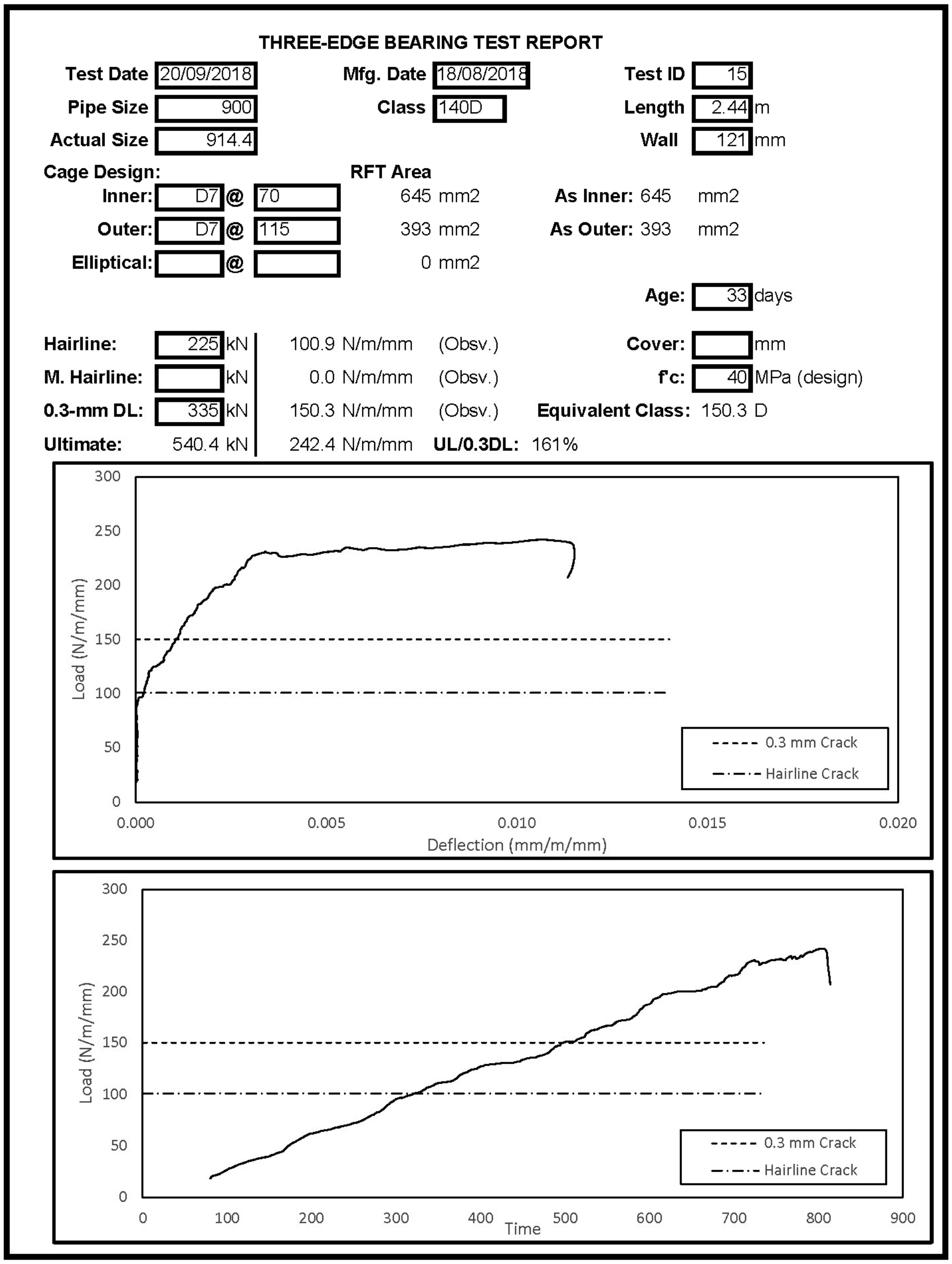

THREE-EDGE BEARING TEST REPORT

Test Date	20/09/2018	**Mfg. Date**	18/08/2018	**Test ID**	15
Pipe Size	900	**Class**	140D	**Length**	2.44 m
Actual Size	914.4			**Wall**	121 mm
Cage Design:		**RFT Area**			
Inner:	D7 @ 70	645 mm2		**As Inner:**	645 mm2
Outer:	D7 @ 115	393 mm2		**As Outer:**	393 mm2
Elliptical:	@	0 mm2			
				Age:	33 days
Hairline:	225 kN	100.9 N/m/mm	(Obsv.)	**Cover:**	mm
M. Hairline:	kN	0.0 N/m/mm	(Obsv.)	**f'c:**	40 MPa (design)
0.3-mm DL:	335 kN	150.3 N/m/mm	(Obsv.)	**Equivalent Class:**	150.3 D
Ultimate:	540.4 kN	242.4 N/m/mm	**UL/0.3DL:**	161%	

THREE-EDGE BEARING TEST REPORT

Test Date	20/09/2018	**Mfg. Date**	18/08/2018	**Test ID**	16
Pipe Size	900	**Class**	140D	**Length**	2.44 m
Actual Size	914.4			**Wall**	121 mm

Cage Design: **RFT Area**

Inner:	D7 @ 70	645 mm2	**As Inner:**	645	mm2
Outer:	D7 @ 115	393 mm2	**As Outer:**	393	mm2
Elliptical:	@	0 mm2			

Age: 33 days

Hairline:	225 kN	100.9 N/m/mm	(Obsv.)	**Cover:**	mm
M. Hairline:	kN	0.0 N/m/mm	(Obsv.)	**f'c:**	40 MPa (design)
0.3-mm DL:	341 kN	153.0 N/m/mm	(Obsv.)	**Equivalent Class:**	153.0 D
Ultimate:	557.2 kN	250.0 N/m/mm	**UL/0.3DL:**	163%	

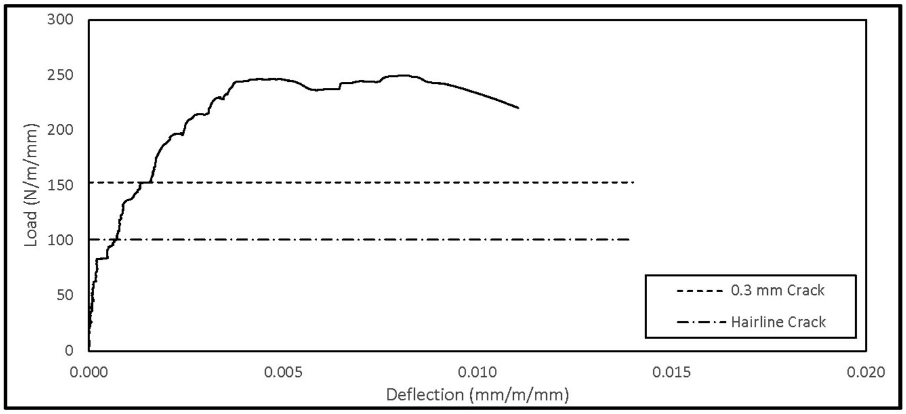

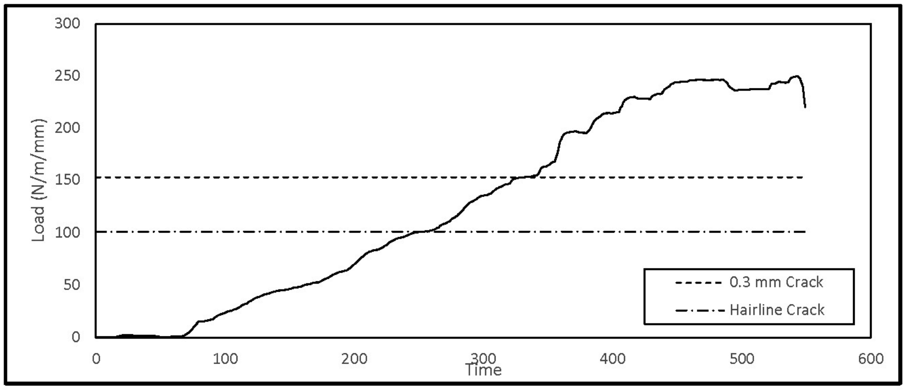

THREE-EDGE BEARING TEST REPORT

Test Date	17/10/2018	**Mfg. Date**	20/09/2018	**Test ID**	17
Pipe Size	975	**Class**	140D	**Length**	2.44 m
Actual Size	990.6			**Wall**	127 mm

Cage Design: **RFT Area**

Inner:	D7	**@**	60	753 mm2	**As Inner:**	753 mm2
Outer:	D7	**@**	100	452 mm2	**As Outer:**	452 mm2
Elliptical:		**@**		0 mm2		

Age: 38 days

Hairline:	249 kN	103.1 N/m/mm	(Obsv.)	**Cover:**	mm
M. Hairline:	kN	0.0 N/m/mm	(Obsv.)	**f'c:**	40 MPa (design)
0.3-mm DL:	396 kN	164.0 N/m/mm	(Obsv.)	**Equivalent Class:**	164.0 D
Ultimate:	567.7 kN	235.1 N/m/mm	**UL/0.3DL:**	143%	

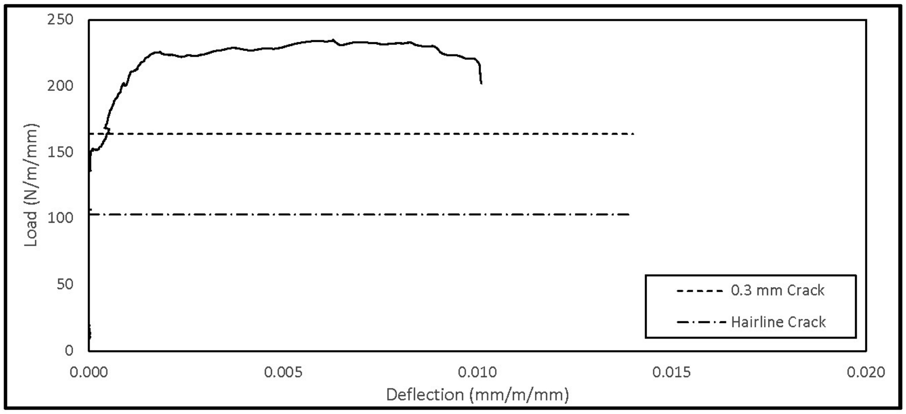

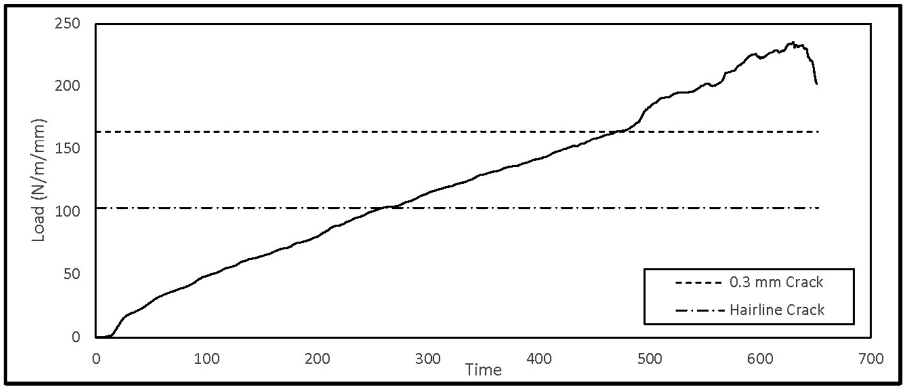

THREE-EDGE BEARING TEST REPORT

Test Date	03/12/2018	**Mfg. Date**	27/11/2018	**Test ID**	22
Pipe Size	1200	**Class**	140D	**Length**	2.44 m
Actual Size	1219.2			**Wall**	127 mm

Cage Design: **RFT Area**

Inner:	D12 @ 50	1548 mm2	**As Inner:**	1548	mm2
Outer:	D7 @ 70	645 mm2	**As Outer:**	645	mm2
Elliptical:	@	0 mm2			

Age: 6 days

Hairline:	239 kN	80.4 N/m/mm	(Obsv.)	**Cover:**	mm
M. Hairline:	318 kN	107.0 N/m/mm	(Obsv.)	**f'c:**	40 MPa (design)
0.3-mm DL:	485 kN	163.2 N/m/mm	(Obsv.)	**Equivalent Class:**	156.7 D
Ultimate:	582.4 kN	195.9 N/m/mm	**UL/0.3DL:**	120%	

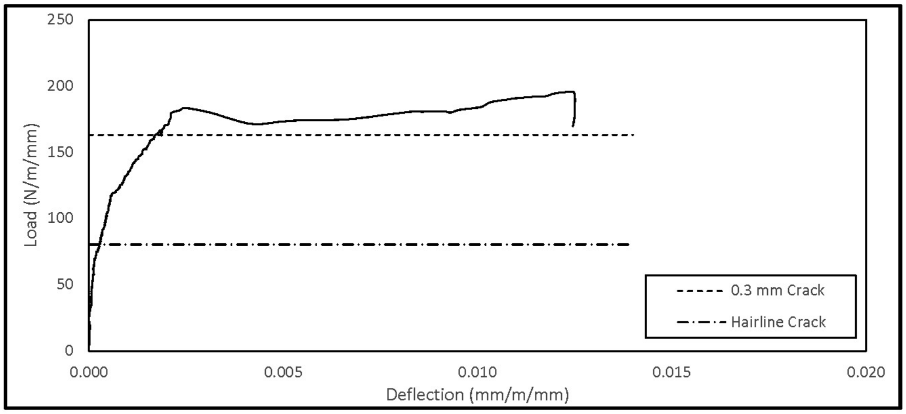

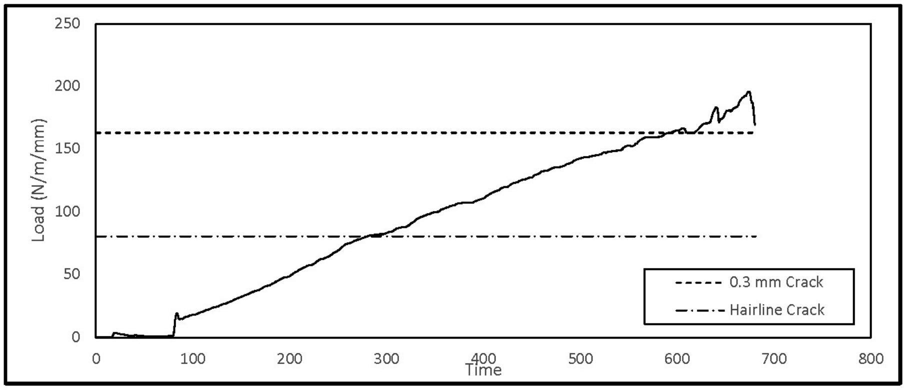

THREE-EDGE BEARING TEST REPORT

Test Date	04/12/2018	**Mfg. Date**	27/11/2018	**Test ID**	23
Pipe Size	1200	**Class**	100D	**Length**	2.44 m
Actual Size	1219.2			**Wall**	127 mm

Cage Design:			**RFT Area**		
Inner:	D7	**@** 55	821 mm2	**As Inner:**	821 mm2
Outer:	D7	**@** 70	645 mm2	**As Outer:**	645 mm2
Elliptical:		**@**	0 mm2		
				Age:	7 days

Hairline:	194 kN	65.3 N/m/mm	(Obsv.)	**Cover:**	mm
M. Hairline:	220 kN	74.0 N/m/mm	(Obsv.)	**f'c:**	30 MPa (design)
0.3-mm DL:	341 kN	114.7 N/m/mm	(Obsv.)	**Equivalent Class:**	111.3 D
Ultimate:	496.4 kN	167.0 N/m/mm	**UL/0.3DL:**	146%	

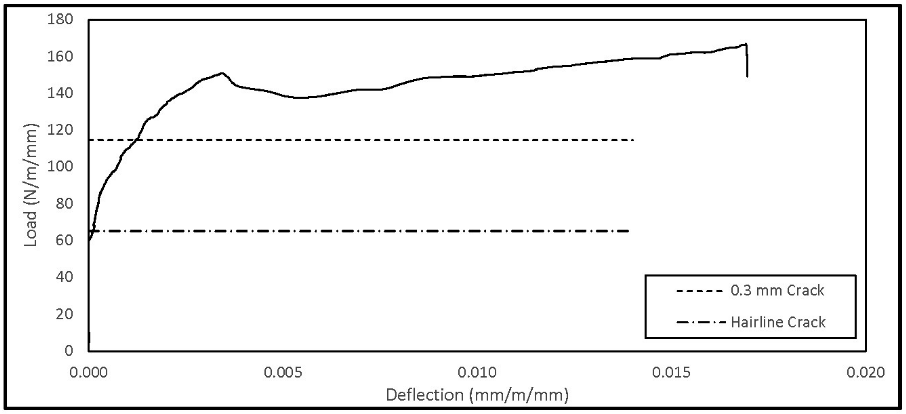

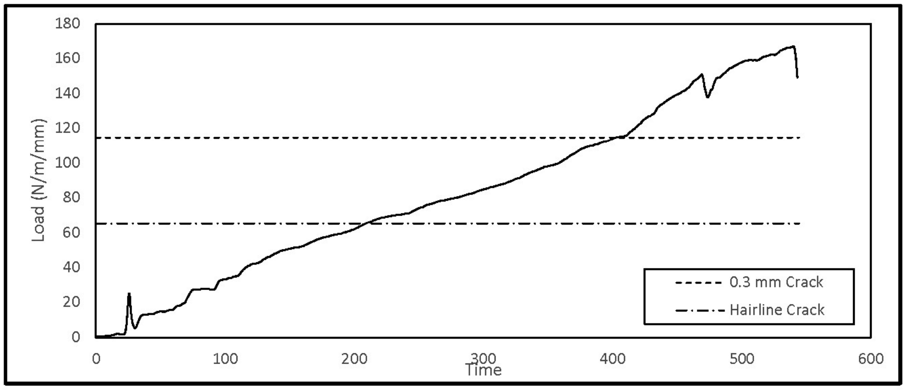

THREE-EDGE BEARING TEST REPORT

Test Date	20/03/2019	**Mfg. Date**	11/03/2019	**Test ID**	35
Pipe Size	1950	**Class**	100D	**Length**	2.44 m
Actual Size	1981.2			**Wall**	191 mm

Cage Design: **RFT Area**

Inner:	D12 @ 45	1721 mm2	**As Inner:**	1721	mm2
Outer:	D12 @ 80	968 mm2	**As Outer:**	968	mm2
Elliptical:	@	0 mm2			

Age: 9 days

Hairline:	403 kN	83.4 N/m/mm	(Obsv.)	**Cover:**	mm
M. Hairline:	466 kN	96.5 N/m/mm	(Obsv.)	**f'c:**	40 MPa (design)
0.3-mm DL:	621 kN	128.6 N/m/mm	(Obsv.)	**Equivalent Class:**	85.7 D
Ultimate:	621.1 kN	128.6 N/m/mm	**UL/0.3DL:**	100%	

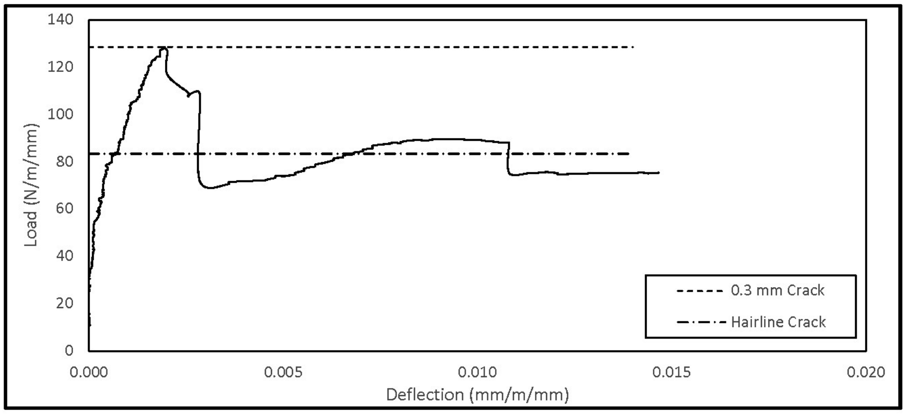

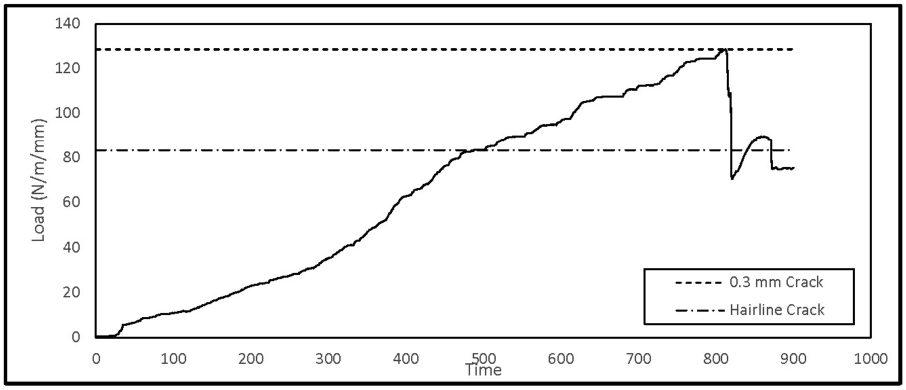

THREE-EDGE BEARING TEST REPORT

Test Date	20/03/2019	**Mfg. Date**	11/03/2019	**Test ID**	36
Pipe Size	1950	**Class**	100D	**Length**	2.44 m
Actual Size	1981.2			**Wall**	191 mm

Cage Design:		**RFT Area**		
Inner:	D12 **@** 45	1721 mm2	**As Inner:**	1721 mm2
Outer:	D12 **@** 80	968 mm2	**As Outer:**	968 mm2
Elliptical:	**@**	0 mm2		
			Age:	9 days

Hairline:	408 kN	84.5 N/m/mm	(Obsv.)	**Cover:**	mm
M. Hairline:	471 kN	97.5 N/m/mm	(Obsv.)	**f'c:**	40 MPa (design)
0.3-mm DL:	600 kN	124.2 N/m/mm	(Obsv.)	**Equivalent Class:**	83.5 D
Ultimate:	604.7 kN	125.2 N/m/mm	**UL/0.3DL:**	101%	

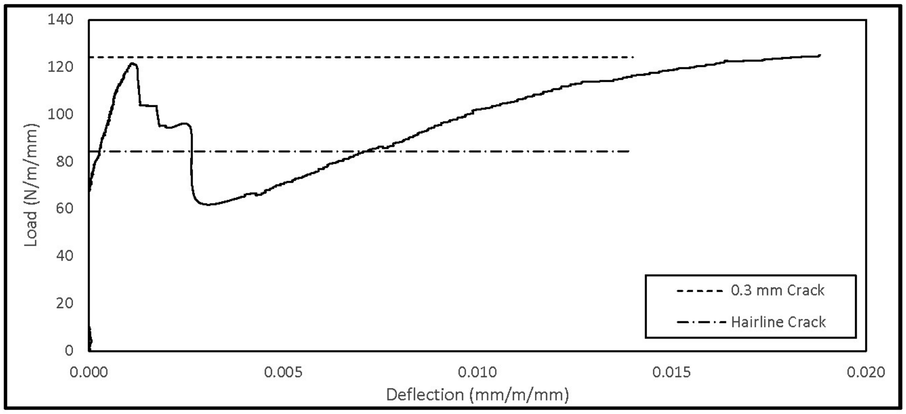

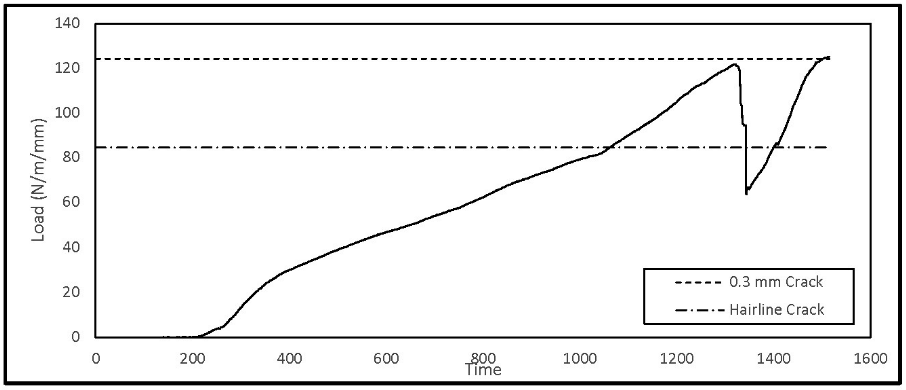

THREE-EDGE BEARING TEST REPORT

Test Date	31/08/2018	**Mfg. Date**	20/08/2018	**Test ID**	37
Pipe Size	975	**Class**	100D	**Length**	2.44 m
Actual Size	990.6			**Wall**	121 mm

Cage Design:				**RFT Area**		
Inner:	W4.5	@	75	387 mm2	**As Inner:**	387 mm2
Outer:	W4.5	@	100	290 mm2	**As Outer:**	290 mm2
Elliptical:		@		0 mm2		
					Age:	11 days

Hairline:	225 kN	93.2 N/m/mm	(Obsv.)	**Cover:**	mm
M. Hairline:	kN	0.0 N/m/mm	(Obsv.)	**f'c:**	30 MPa (design)
0.3-mm DL:	261 kN	108.1 N/m/mm	(Obsv.)	**Equivalent Class:**	108.1 D
Ultimate:	399.4 kN	165.4 N/m/mm	**UL/0.3DL:** 153%		

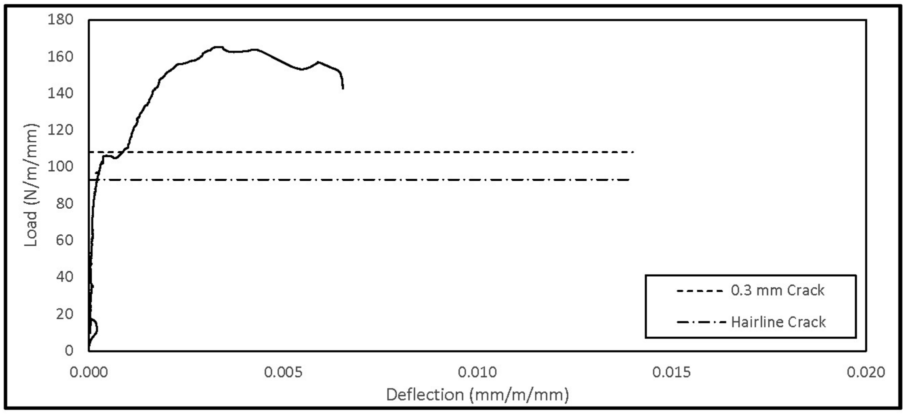

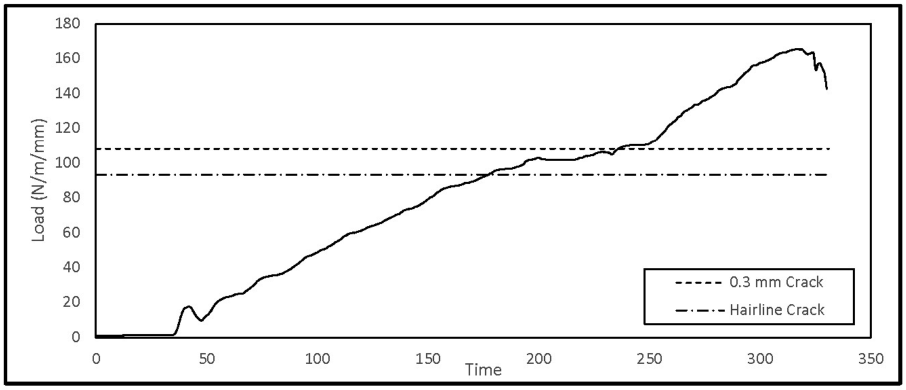

THREE-EDGE BEARING TEST REPORT

Test Date 24/06/2019 **Mfg. Date** 04/05/2017 **Test ID** 43

Pipe Size 1050 **Class** 140D **Length** 2.44 m

Actual Size 1066.8 **Wall** 133 mm

Cage Design: **RFT Area**

Inner: D7 @ 40 1129 mm2 **As Inner:** 1129 mm2

Outer: D7 @ 100 452 mm2 **As Outer:** 452 mm2

Elliptical: @ 0 mm2

Age: 782 days

Hairline: 218 kN 83.8 N/m/mm (Obsv.) **Cover:** 25.9 mm

M. Hairline: 361 kN 138.8 N/m/mm (Obsv.) **f'c:** 54.3 MPa (SH)

0.3-mm DL: 425 kN 163.4 N/m/mm (Obsv.) **Equivalent Class:** 163.4 D

Ultimate: 532.4 kN 204.7 N/m/mm **UL/0.3DL:** 125% RT fail, yielding

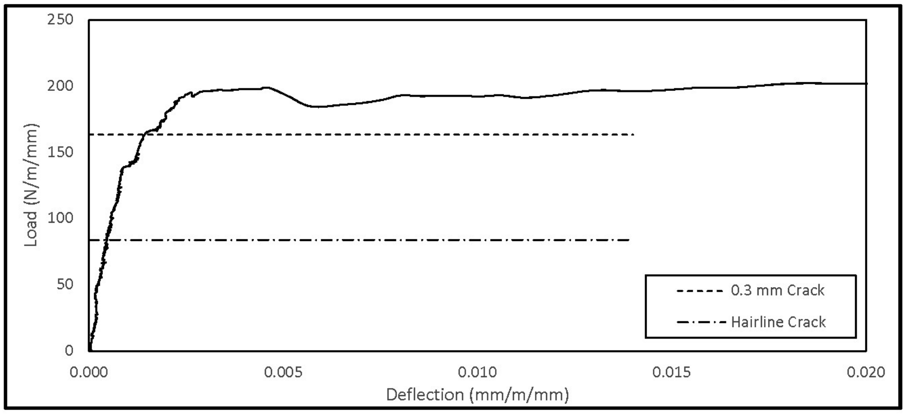

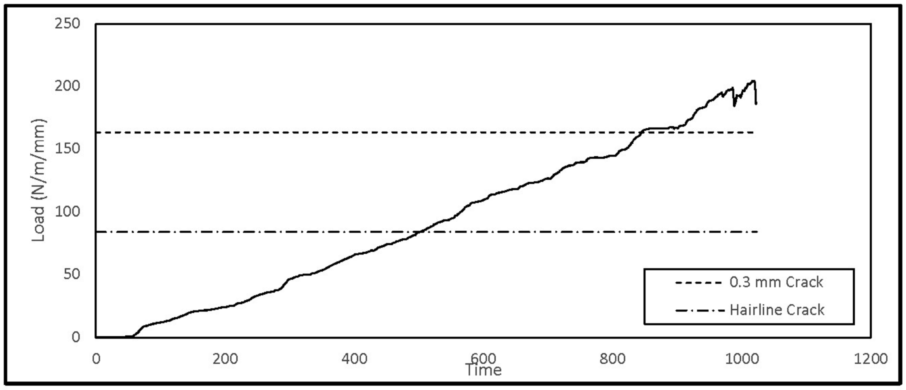

THREE-EDGE BEARING TEST REPORT

Test Date	25/06/2019	**Mfg. Date**	14/06/2019	**Test ID**	44
Pipe Size	1050	**Class**	140D	**Length**	2.44 m
Actual Size	1066.8			**Wall**	133 mm

Cage Design: **RFT Area**

Inner:	W4.5	**@**	50	581 mm2	**As Inner:**	581 mm2
Outer:	W4.5	**@**	100	290 mm2	**As Outer:**	290 mm2
Elliptical:		**@**		0 mm2		

Age: 11 days

Hairline:	189 kN	72.7 N/m/mm	(Obsv.)	**Cover:**	25.9 mm
M. Hairline:	kN	0.0 N/m/mm	(Obsv.)	**f'c:**	41.3 MPa (SH)
0.3-mm DL:	297 kN	114.2 N/m/mm	(Obsv.)	**Equivalent Class:**	114.2 D
Ultimate:	419.2 kN	161.2 N/m/mm	**UL/0.3DL:** 141%		DT fail

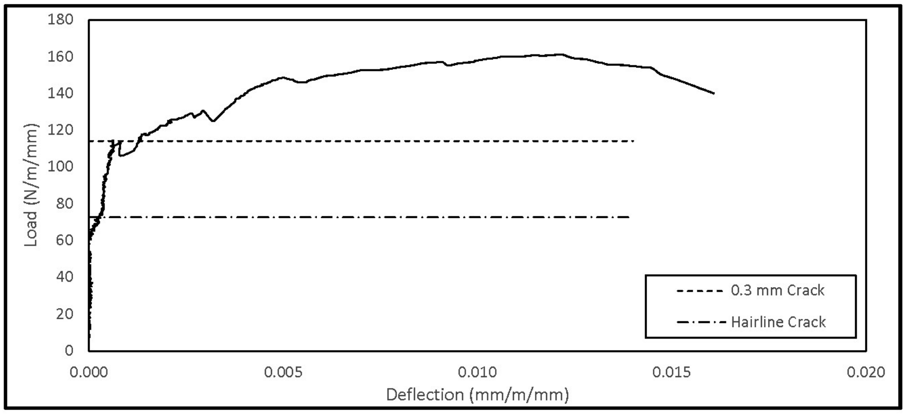

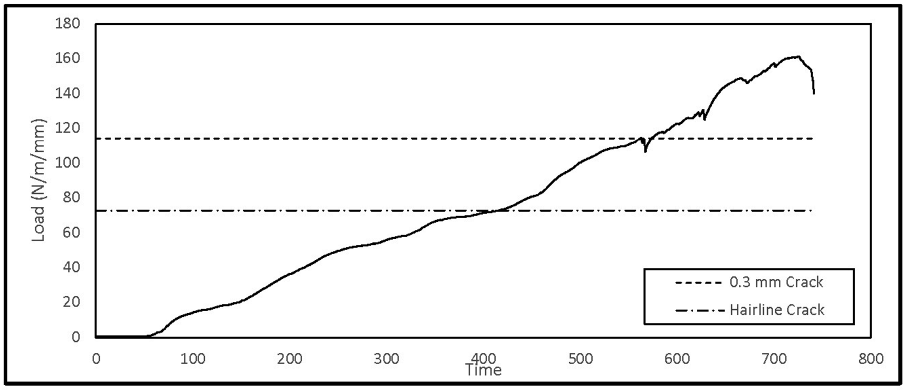

THREE-EDGE BEARING TEST REPORT

Test Date 12/08/2019 **Mfg. Date** 02/08/2019 **Test ID** 51
Pipe Size 1200 **Class** 65D **Length** 2.44 m
Actual Size 1219.2 **Wall** 127 mm

Cage Design: **RFT Area**
Inner: D7 **@** 80 565 mm2 **As Inner:** 565 mm2
Outer: D7 **@** 120 376 mm2 **As Outer:** 376 mm2
Elliptical: **@** 0 mm2

Age: 10 days

Hairline: 179 kN 60.2 N/m/mm (Obsv.) **Cover:** 40.8 mm
M. Hairline: 205 kN 69.0 N/m/mm (Obsv.) **f'c:** 44.7 MPa (SH)
0.3-mm DL: 213 kN 71.7 N/m/mm (Obsv.) **Equivalent Class:** 71.7 D
Ultimate: 434.4 kN 146.2 N/m/mm **UL/0.3DL:** 204% F & DT fail

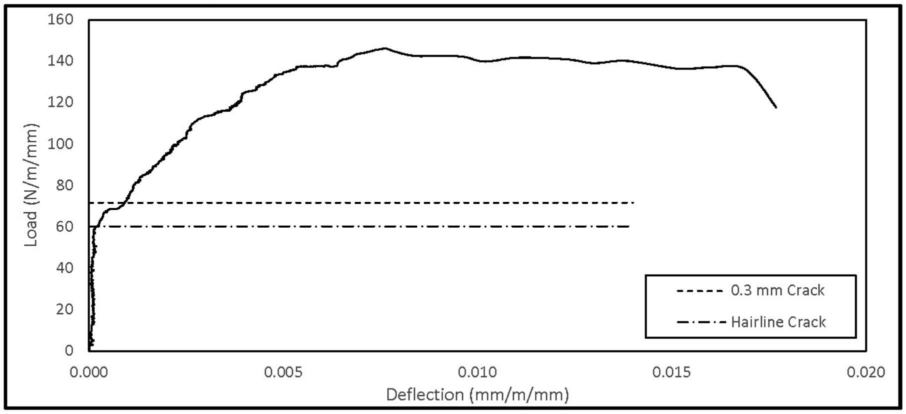

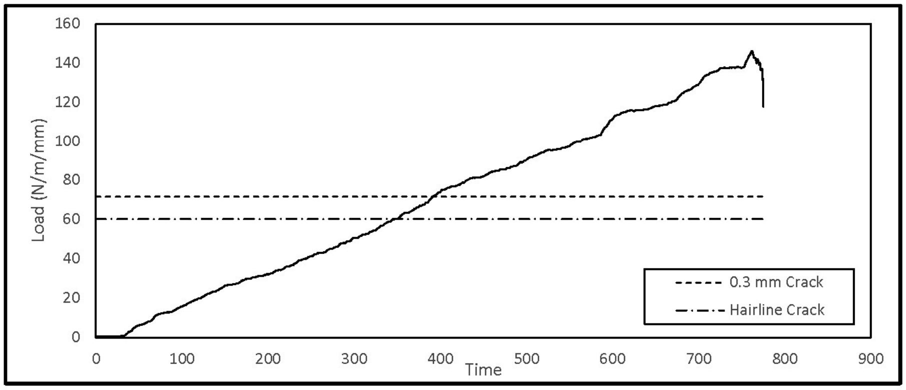

THREE-EDGE BEARING TEST REPORT

Test Date	12/08/2019	**Mfg. Date**	02/08/2019	**Test ID**	52
Pipe Size	1200	**Class**	65D	**Length**	2.44 m
Actual Size	1219.2			**Wall**	127 mm

Cage Design:			**RFT Area**		
Inner:	D7 @	80	565 mm2	**As Inner:**	565 mm2
Outer:	D7 @	120	376 mm2	**As Outer:**	376 mm2
Elliptical:	@		0 mm2		

Age: 10 days

Hairline:	104 kN	35.0 N/m/mm	(Obsv.)	**Cover:**	37.9 mm
M. Hairline:	kN	0.0 N/m/mm	(Obsv.)	**f'c:**	40.2 MPa (SH)
0.3-mm DL:	219 kN	73.7 N/m/mm	(Obsv.)	**Equivalent Class:**	73.7 D
Ultimate:	394.3 kN	132.7 N/m/mm	**UL/0.3DL:** 180%		DT fail

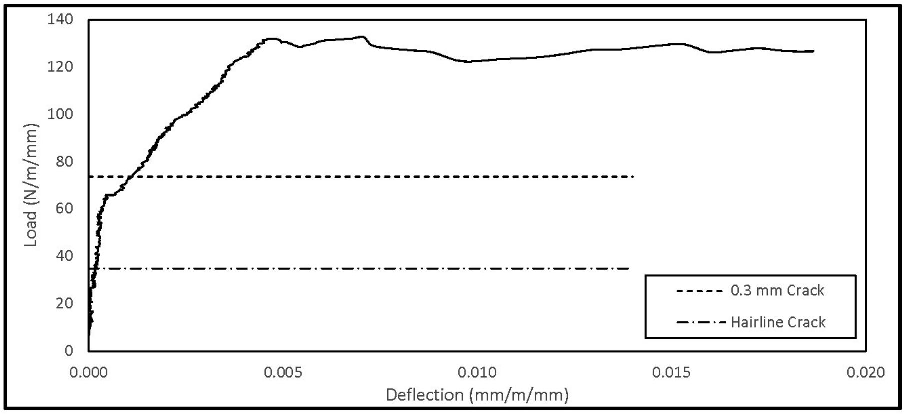

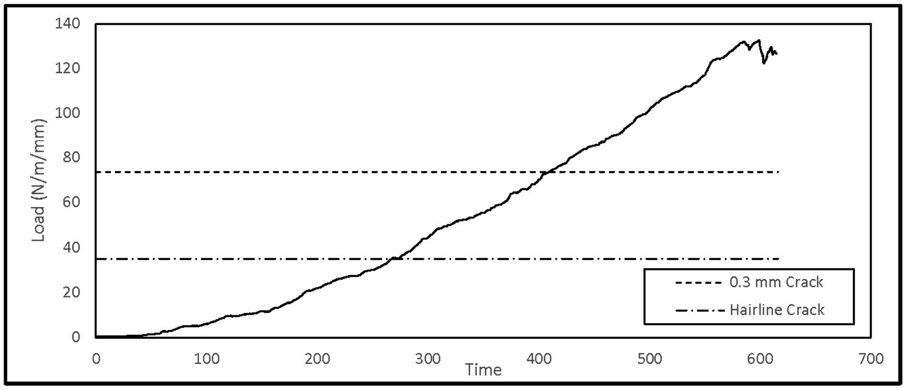

THREE-EDGE BEARING TEST REPORT

Test Date	12/08/2019	**Mfg. Date**	02/08/2019	**Test ID**	53
Pipe Size	1200	**Class**	65D	**Length**	2.44 m
Actual Size	1219.2			**Wall**	127 mm

Cage Design:				**RFT Area**		
Inner:	D7	@	80	565 mm2	**As Inner:** 565	mm2
Outer:	D7	@	120	376 mm2	**As Outer:** 376	mm2
Elliptical:		@		0 mm2		

Age: 10 days

Hairline:	179 kN	60.2 N/m/mm	(Obsv.)	**Cover:**	29.4 mm
M. Hairline:	222 kN	74.7 N/m/mm	(Obsv.)	**f'c:**	40.9 MPa (SH)
0.3-mm DL:	266 kN	89.5 N/m/mm	(Obsv.)	**Equivalent Class:**	89.5 D
Ultimate:	415.6 kN	139.8 N/m/mm	**UL/0.3DL:** 156%		DT fail

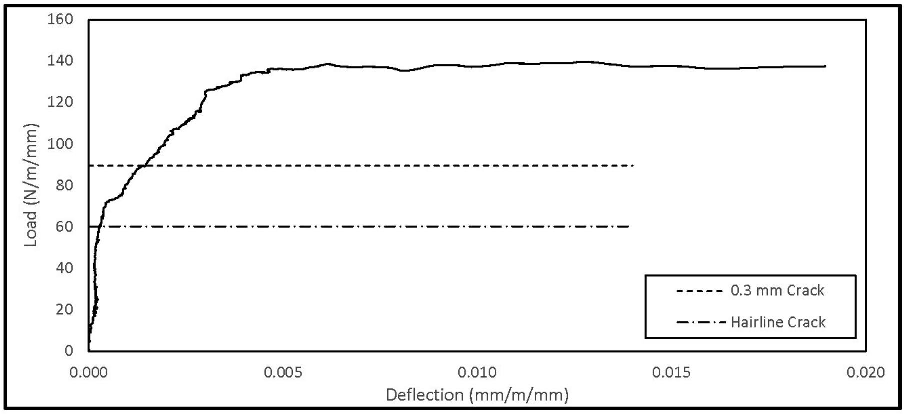

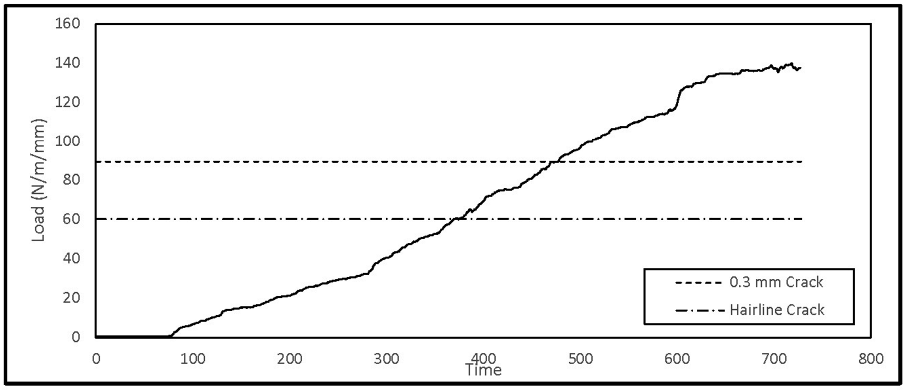

Appendix C: Load-deflection TEBT reports of triple-cage RCP specimens

THREE-EDGE BEARING TEST REPORT

Test Date	21/12/2018	**Mfg. Date**	14/12/2018	**Test ID**	25
Pipe Size	2250	**Class**	140D	**Length**	2.44 m
Actual Size	2286.0			**Wall**	216 mm

Cage Design: **RFT Area**

Inner:	D16 @ 45	2294 mm2	**As Inner:**	3882 mm2
Outer:	D16 @ 100	1032 mm2	**As Outer:**	2621 mm2
Elliptical:	D16 @ 65	1588 mm2		

Age: 7 days

Hairline:	531 kN	95.3 N/m/mm	(Obsv.)	**Cover:**	mm
M. Hairline:	740 kN	132.8 N/m/mm	(Obsv.)	**f'c:**	40 MPa (design)
0.3-mm DL:	970 kN	174.0 N/m/mm	(Obsv.)	**Equivalent Class:**	140.5 D
Ultimate:	978.9 kN	175.6 N/m/mm	**UL/0.3DL:**	101%	

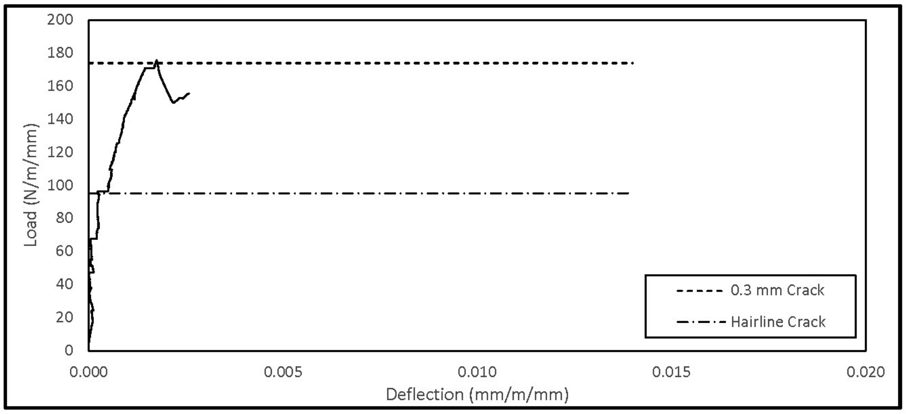

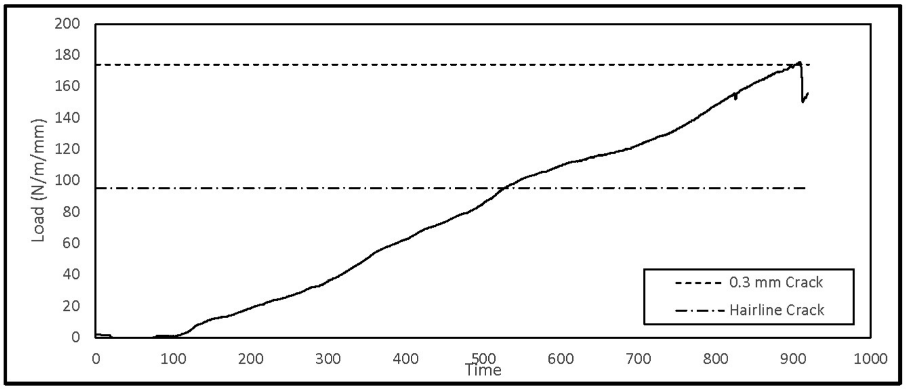

THREE-EDGE BEARING TEST REPORT

Test Date	13/03/2019	**Mfg. Date**	05/03/2019	**Test ID**	27
Pipe Size	2250	**Class**	140D	**Length**	2.44 m
Actual Size	2286.0			**Wall**	216 mm

Cage Design:			**RFT Area**		
Inner:	D16	@ 40	2581 mm2	**As Inner:**	3484 mm2
Outer:	D16	@ 100	1032 mm2	**As Outer:**	1936 mm2
Elliptical:	D14	@ 100	903 mm2		
				Age:	8 days

Hairline:	501 kN	89.9 N/m/mm	(Obsv.)	**Cover:**	mm
M. Hairline:	580 kN	104.1 N/m/mm	(Obsv.)	**f'c:**	40 MPa (design)
0.3-mm DL:	858 kN	153.9 N/m/mm	(Obsv.)	**Equivalent Class:**	140.5 D
Ultimate:	978.9 kN	175.6 N/m/mm	**UL/0.3DL:**	114%	

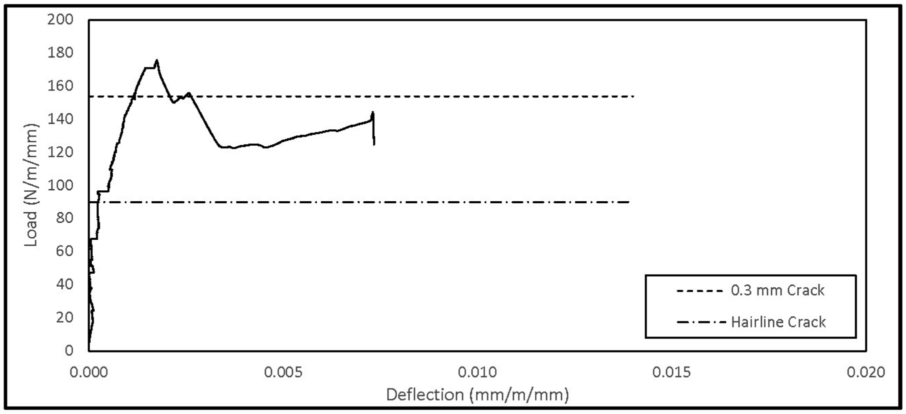

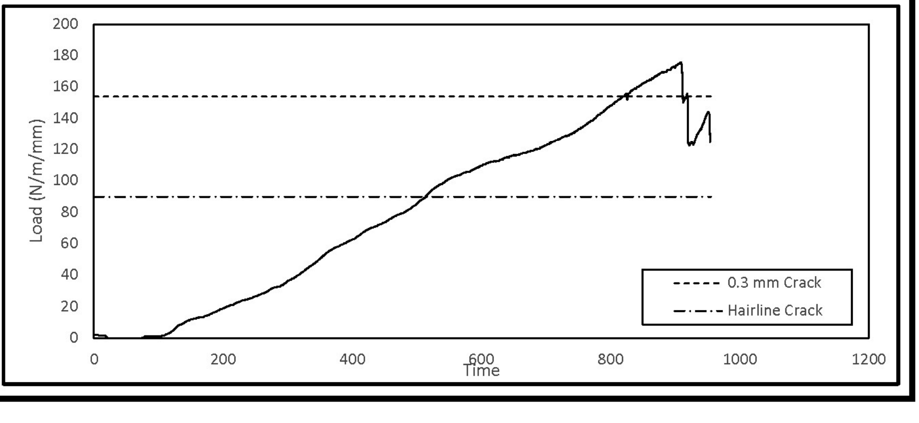

THREE-EDGE BEARING TEST REPORT

Test Date 13/03/2019 **Mfg. Date** 05/03/2019 **Test ID** 28

Pipe Size 2250 **Class** 140D **Length** 2.44 m

Actual Size 2286.0 **Wall** 216 mm

Cage Design: **RFT Area**

Inner: D16 @ 40 2581 mm2 **As Inner:** 3484 mm2

Outer: D16 @ 100 1032 mm2 **As Outer:** 1936 mm2

Elliptical: D14 @ 100 903 mm2

Age: 8 days

Hairline: 513 kN | 92.0 N/m/mm (Obsv.) **Cover:** mm

M. Hairline: 624 kN | 112.0 N/m/mm (Obsv.) **f'c:** 40 MPa (design)

0.3-mm DL: 909 kN | 163.1 N/m/mm (Obsv.) **Equivalent Class:** 145.3 D

Ultimate: 1013 kN | 181.7 N/m/mm **UL/0.3DL:** 111%

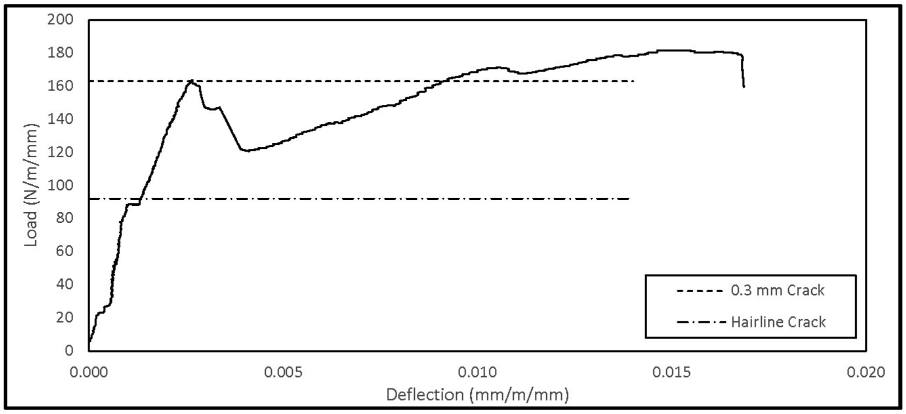

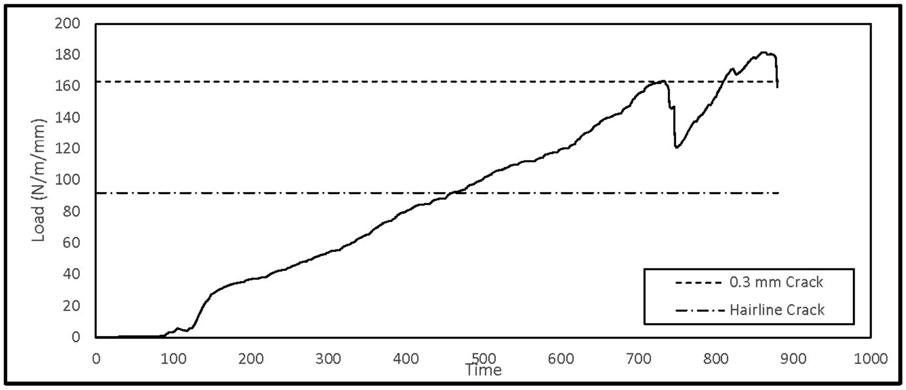

THREE-EDGE BEARING TEST REPORT

Test Date	13/03/2019	**Mfg. Date**	06/03/2019	**Test ID**	29
Pipe Size	2100	**Class**	100D	**Length**	2.44 m
Actual Size	2133.6			**Wall**	203 mm

Cage Design: **RFT Area**

Inner:	D12 @ 50	1548 mm2	**As Inner:**	2624	mm2
Outer:	D10 @ 100	645 mm2	**As Outer:**	1721	mm2
Elliptical:	D10 @ 60	1075 mm2			

Age: 7 days

Hairline:	571 kN	109.8 N/m/mm	(Obsv.)	**Cover:**	mm
M. Hairline:	817 kN	157.1 N/m/mm	(Obsv.)	**f'c:**	40 MPa (design)
0.3-mm DL:	817 kN	157.1 N/m/mm	(Obsv.)	**Equivalent Class:**	108.1 D
Ultimate:	843.5 kN	162.2 N/m/mm	**UL/0.3DL:**	103%	

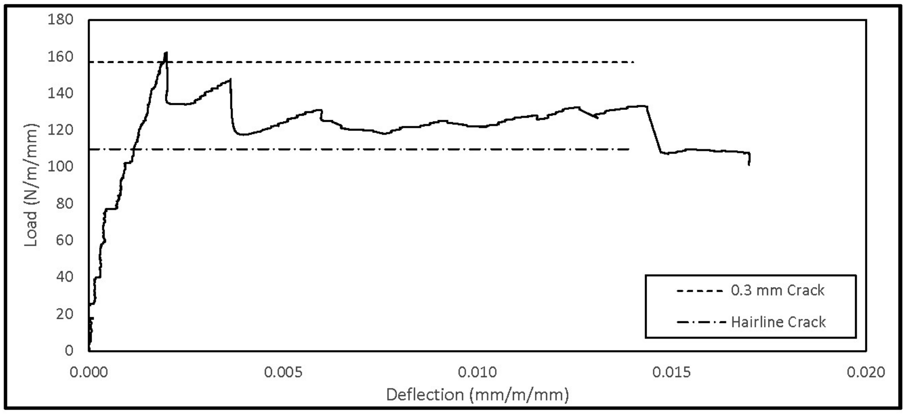

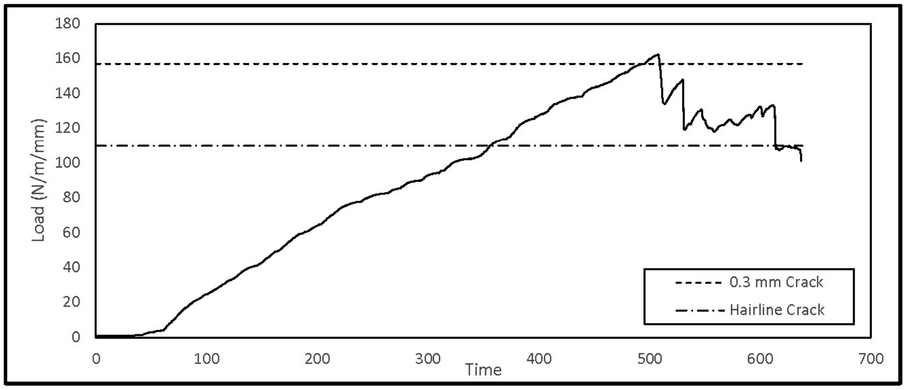

THREE-EDGE BEARING TEST REPORT

Test Date	15/03/2019	**Mfg. Date**	08/03/2019	**Test ID**	30
Pipe Size	1800	**Class**	100D	**Length**	2.44 m
Actual Size	1828.8			**Wall**	178 mm

Cage Design:		**RFT Area**		
Inner:	D7 @ 55	821 mm2	**As Inner:**	2112 mm2
Outer:	D7 @ 100	452 mm2	**As Outer:**	1742 mm2
Elliptical:	D10 @ 50	1290 mm2		
			Age:	7 days

Hairline:	294 kN	65.9 N/m/mm	(Obsv.)	**Cover:**	mm
M. Hairline:	404 kN	90.6 N/m/mm	(Obsv.)	**f'c:**	44 MPa (actual)
0.3-mm DL:	552 kN	123.8 N/m/mm	(Obsv.)	**Equivalent Class:**	104.5 D
Ultimate:	698.7 kN	156.7 N/m/mm	**UL/0.3DL:**	127%	

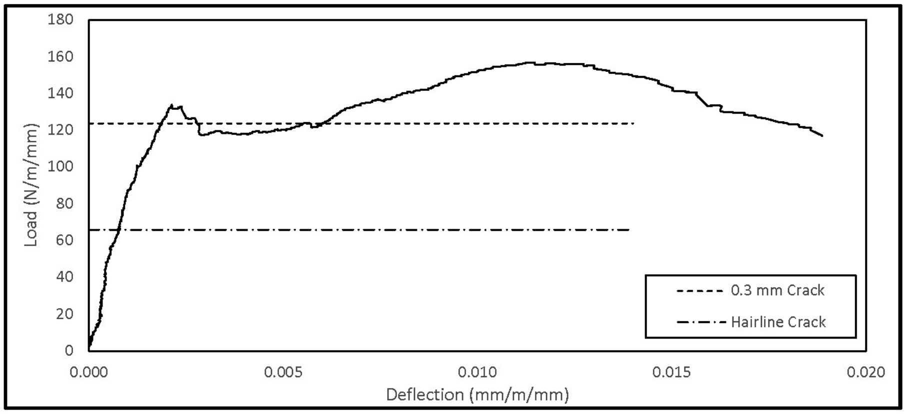

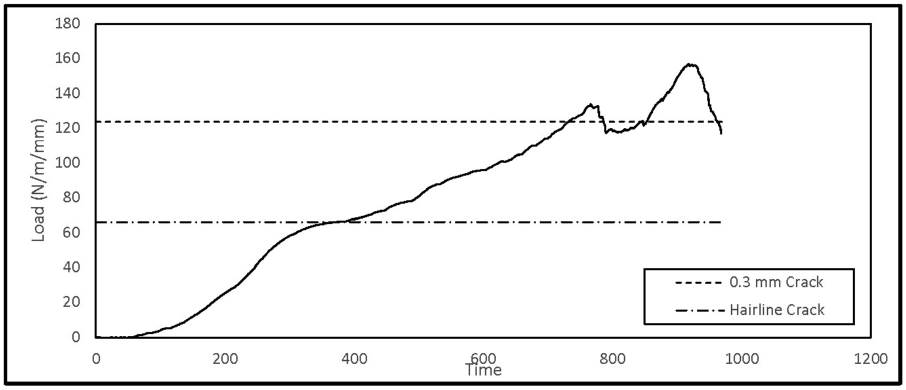

THREE-EDGE BEARING TEST REPORT

Test Date	15/03/2019	**Mfg. Date**	11/03/2019	**Test ID**	31
Pipe Size	1800	**Class**	140D	**Length**	2.44 m
Actual Size	1828.8			**Wall**	178 mm

Cage Design:

			RFT Area		
Inner:	D14 @	50	1807 mm2	**As Inner:**	3097 mm2
Outer:	D12 @	100	774 mm2	**As Outer:**	2065 mm2
Elliptical:	D12 @	60	1290 mm2		

Age: 4 days

Hairline:	373 kN	83.7 N/m/mm	(Obsv.)	**Cover:**	mm
M. Hairline:	430 kN	96.4 N/m/mm	(Obsv.)	**f'c:**	45.5 MPa (actual)
0.3-mm DL:	711 kN	159.5 N/m/mm	(Obsv.)	**Equivalent Class:**	146.1 D
Ultimate:	814.2 kN	182.6 N/m/mm	**UL/0.3DL:**	115%	

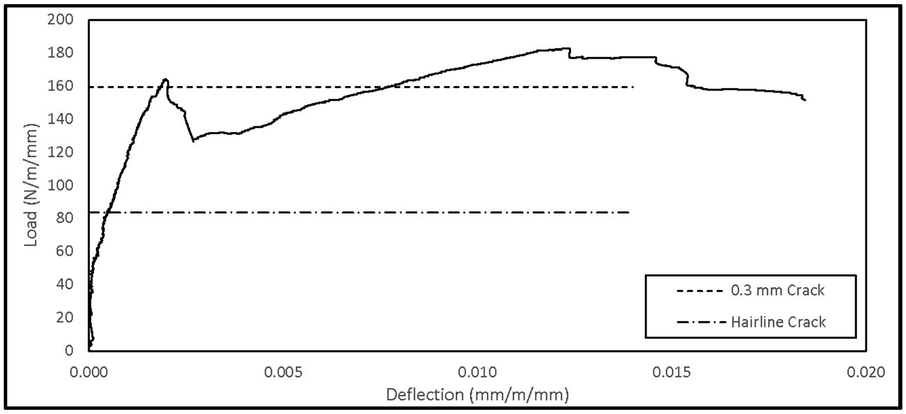

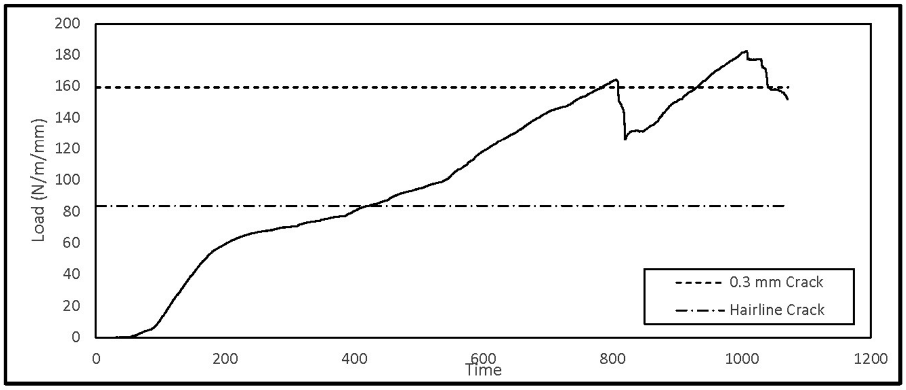

THREE-EDGE BEARING TEST REPORT

Test Date	15/03/2019	**Mfg. Date**	11/03/2019	**Test ID**	32
Pipe Size	1800	**Class**	140D	**Length**	2.44 m
Actual Size	1828.8			**Wall**	178 mm

Cage Design: **RFT Area**

Inner:	D14 @ 50	1807 mm2	**As Inner:**	3097	mm2
Outer:	D12 @ 100	774 mm2	**As Outer:**	2065	mm2
Elliptical:	D12 @ 60	1290 mm2			

Age: 4 days

Hairline:	360 kN	80.7 N/m/mm	(Obsv.)	**Cover:**	mm
M. Hairline:	409 kN	91.7 N/m/mm	(Obsv.)	**f'c:**	47 MPa (actual)
0.3-mm DL:	682 kN	153.0 N/m/mm	(Obsv.)	**Equivalent Class:**	132.5 D
Ultimate:	738.3 kN	165.6 N/m/mm	**UL/0.3DL:**	108%	

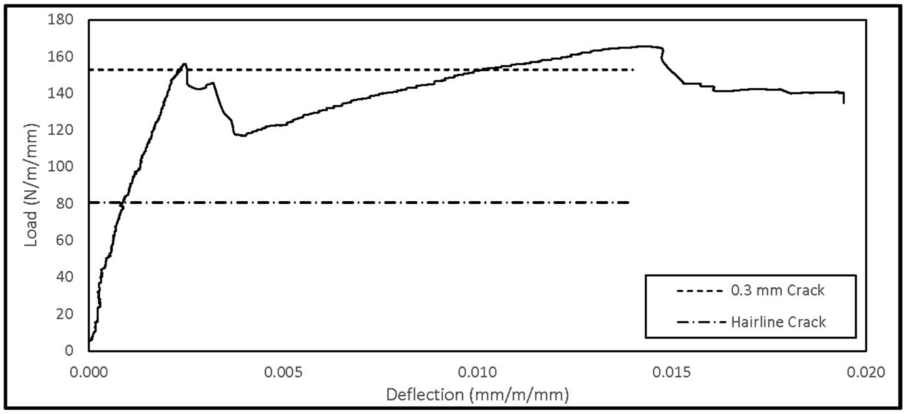

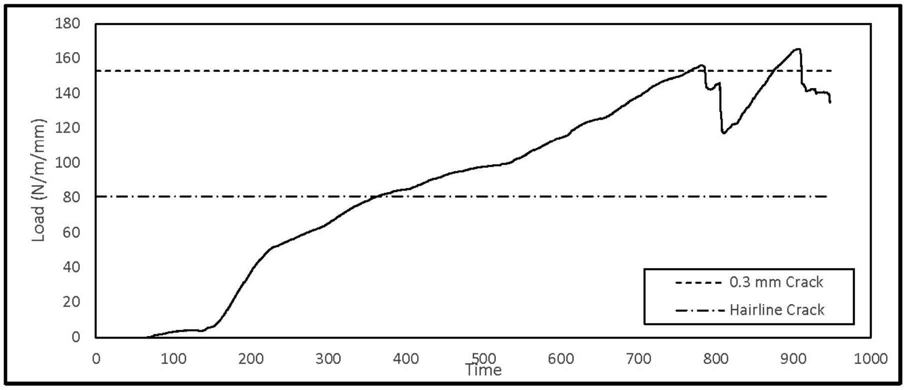

THREE-EDGE BEARING TEST REPORT

Test Date	15/03/2019	**Mfg. Date**	11/03/2019	**Test ID**	33
Pipe Size	1800	**Class**	140D	**Length**	2.44 m
Actual Size	1828.8			**Wall**	178 mm

Cage Design: **RFT Area**

Inner:	D14 @ 50	1807 mm2	**As Inner:**	3097 mm2
Outer:	D12 @ 100	774 mm2	**As Outer:**	2065 mm2
Elliptical:	D12 @ 60	1290 mm2		

Age: 4 days

Hairline:	400 kN	89.7 N/m/mm	(Obsv.)	**Cover:**	mm
M. Hairline:	480 kN	107.7 N/m/mm	(Obsv.)	**f'c:**	43.5 MPa (actual)
0.3-mm DL:	705 kN	158.1 N/m/mm	(Obsv.)	**Equivalent Class:**	147.6 D
Ultimate:	822.8 kN	184.5 N/m/mm	**UL/0.3DL:**	117%	

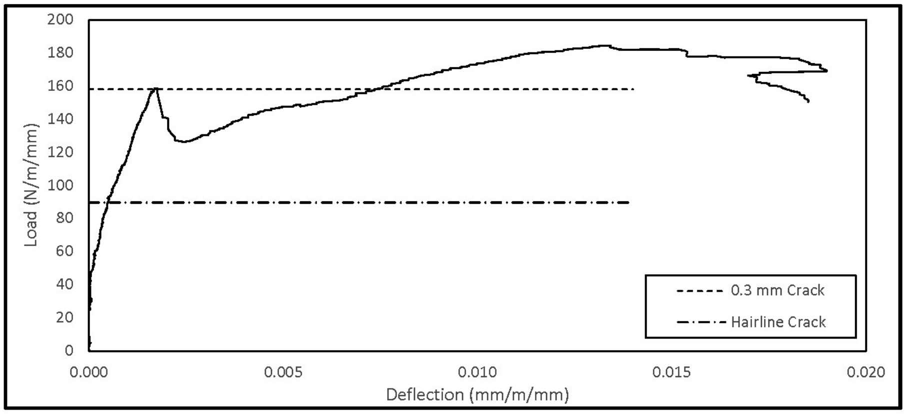

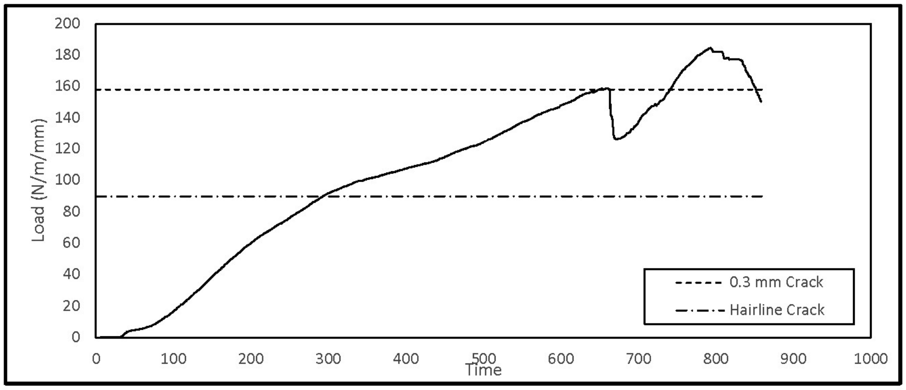

THREE-EDGE BEARING TEST REPORT

Test Date 07/06/2019 **Mfg. Date** 15/05/2019 **Test ID** 38 68 (ccp)

Pipe Size 2100 **Class** 140D **Length** 2.44 m

Actual Size 2138.0 **Wall** 203 mm

Cage Design: **RFT Area**

Inner: D10 **@** 38 1698 mm2 **As Inner:** 2886 mm2

Outer: D7 **@** 38 1189 mm2 **As Outer:** 2377 mm2

Elliptical: D7 **@** 38 1189 mm2

Age: 23 days

Hairline: 324 kN 62.2 N/m/mm (Obsv.) **Cover:** 25 mm

M. Hairline: 394 kN 75.6 N/m/mm (Obsv.) **f'c:** 57 MPa (actual)

0.3-mm DL: 919 kN 176.3 N/m/mm (Obsv.) **Equivalent Class:** 174.5 D

Ultimate: 1137 kN 218.1 N/m/mm **UL/0.3DL:** 124%

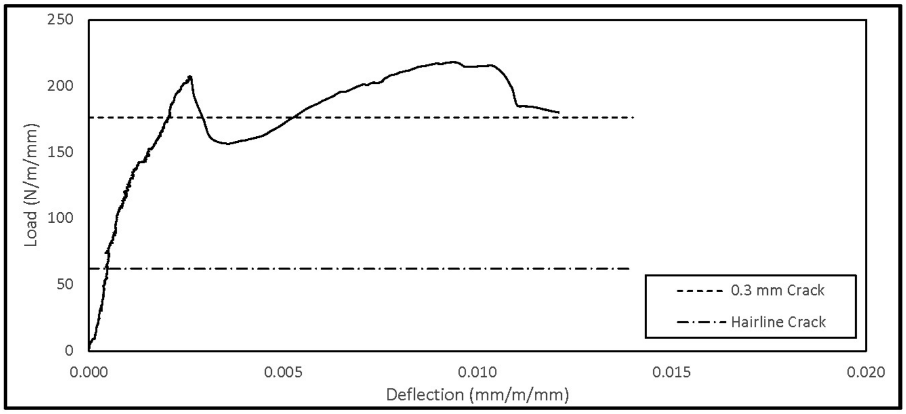

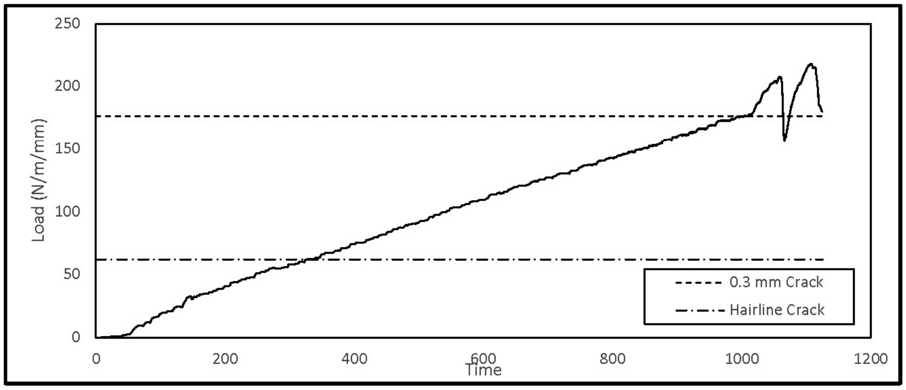

THREE-EDGE BEARING TEST REPORT

Test Date	11/06/2019	**Mfg. Date**	09/05/2019	**Test ID**	39 70 (ccp)
Pipe Size	2100	**Class**	100D	**Length**	2.44 m
Actual Size	2138.0			**Wall**	203 mm

Cage Design: **RFT Area**

Inner:	D6	@	50	774 mm2	**As Inner:**	1548 mm2
Outer:	D6	@	50	774 mm2	**As Outer:**	1548 mm2
Elliptical:	D6	@	50	774 mm2		
Long. :	18	@	380 mm		**Age:**	33 days

Hairline:	291 kN	55.8 N/m/mm	(Obsv.)	**Cover:**	30 mm
M. Hairline:	406 kN	77.9 N/m/mm	(Obsv.)	**f'c:**	57 MPa (actual)
0.3-mm DL:	694 kN	133.1 N/m/mm	(Obsv.)	**Equivalent Class:**	111.2 D
Ultimate:	869.4 kN	166.8 N/m/mm	**UL/0.3DL:** 125%		DT failure at obvert

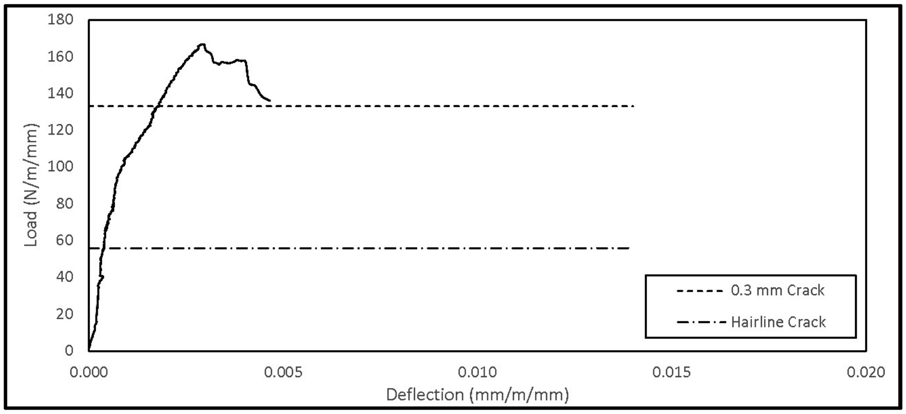

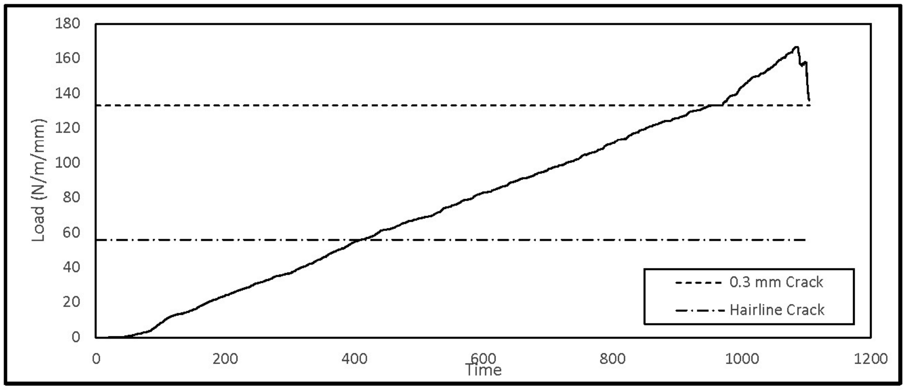

THREE-EDGE BEARING TEST REPORT

Test Date	11/06/2019	**Mfg. Date**	09/05/2019	**Test ID**	40 71 (ccp)
Pipe Size	2100	**Class**	100D	**Length**	2.44 m
Actual Size	2138.0			**Wall**	203 mm

Cage Design: **RFT Area**

Inner:	D6 @ 50	774 mm2		**As Inner:**	1548 mm2
Outer:	D6 @ 50	774 mm2		**As Outer:**	1548 mm2
Elliptical:	D6 @ 50	774 mm2			
Long. :	18 @ 380 mm			**Age:**	33 days

Hairline:	214 kN	41.1 N/m/mm	(Obsv.)	**Cover:**	30 mm
M. Hairline:	358 kN	68.7 N/m/mm	(Obsv.)	**f'c:**	50.8 MPa (actual)
0.3-mm DL:	609 kN	116.8 N/m/mm	(Obsv.)	**Equivalent Class:**	103.3 D
Ultimate:	807.3 kN	154.9 N/m/mm	**UL/0.3DL:** 133%		DT failure at obvert

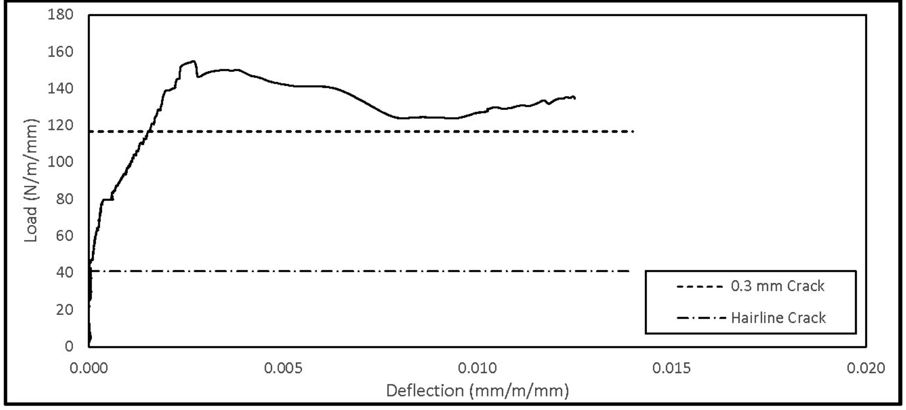

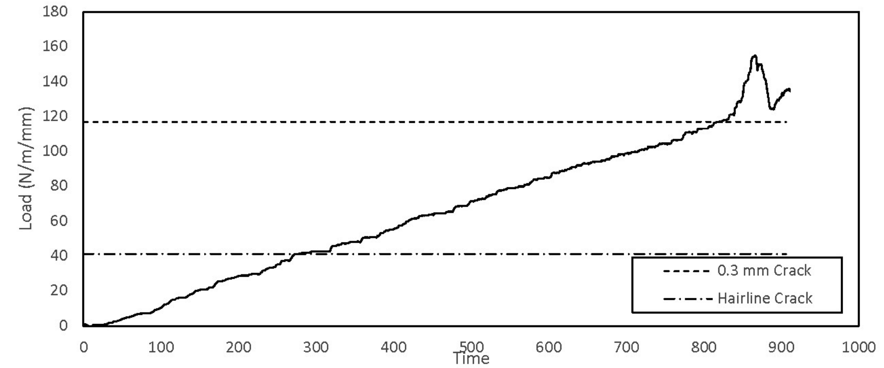

THREE-EDGE BEARING TEST REPORT

Test Date 7/23/2019 **Mfg. Date** 7/5/2019 **Test ID** 46 78 (ccp)

Pipe Size 2400 **Class** 140D **Length** 2.46 m

Actual Size 2433.0 **Wall** 237 mm

Cage Design: **RFT Area**

Inner: D12 @ 50 1548 mm2 **As Inner:** 2839 mm2

Outer: D10 @ 50 1290 mm2 **As Outer:** 2581 mm2

Elliptical: D10 @ 50 1290 mm2 **Longitud.:** 36

Stirr. : W4.5 @ 76 382 mm2 **Age:** 18 days

Hairline: 333 kN 55.6 N/m/mm (Obsv.) **Cover:** 25 mm

M. Hairline: 448 kN 74.9 N/m/mm (Obsv.) **f'c:** 47.4 MPa (actual)

0.3-mm DL: 985 kN 164.6 N/m/mm (Obsv.) **Equivalent Class:** 155 D

Ultimate: 1158 kN 193.5 N/m/mm **UL/0.3DL:** 118% DT failure at obvert

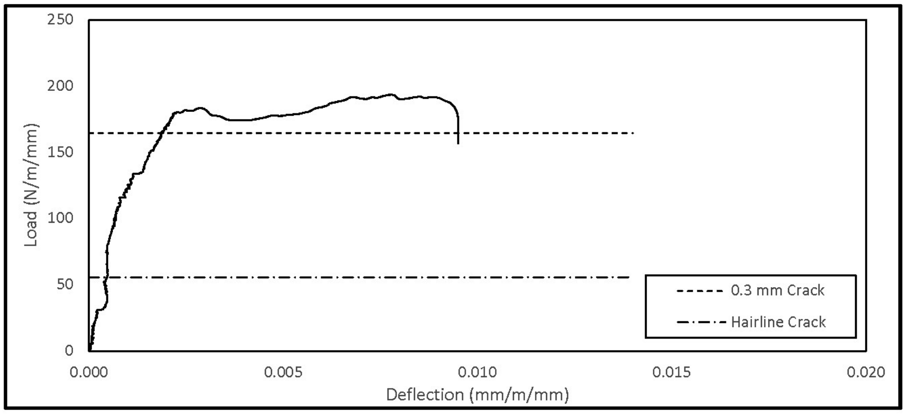

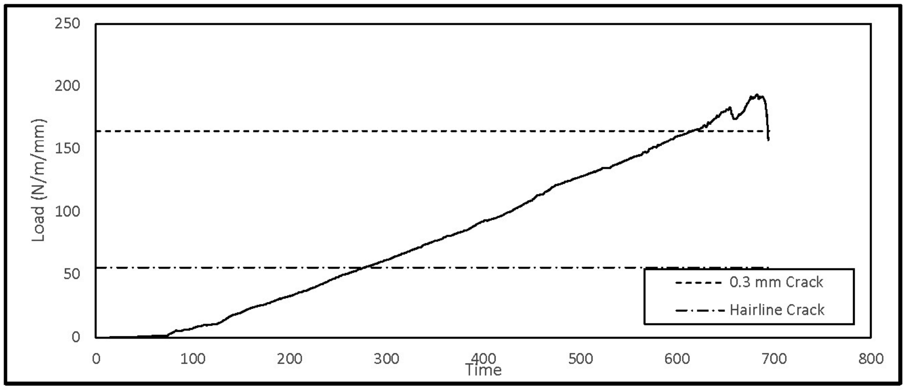

THREE-EDGE BEARING TEST REPORT

Test Date	7/29/2019	**Mfg. Date**	7/5/2019	**Test ID**	46 77 (ccp)
Pipe Size	2400	**Class**	140D	**Length**	2.46 m
Actual Size	2439.0			**Wall**	2.47 mm
Cage Design:		**RFT Area**			
Inner:	D12 @ 50	1548 mm2		**As Inner:**	2839 mm2
Outer:	D10 @ 50	1290 mm2		**As Outer:**	2581 mm2
Elliptical:	D10 @ 50	1290 mm2		**Longitud.:**	36
Stirr. :	W4.5 @ 76	382 mm2		**Age:**	24 days
Hairline:	362 kN	60.3 N/m/mm	(Obsv.)	**Cover:**	25 mm
M. Hairline:	485 kN	80.8 N/m/mm	(Obsv.)	**f'c:**	49.2 MPa (actual)
0.3-mm DL:	957 kN	159.5 N/m/mm	(Obsv.)	**Equivalent Class:**	157 D
Ultimate:	1177 kN	196.2 N/m/mm	**UL/0.3DL:** 123%		DT failure at obvert

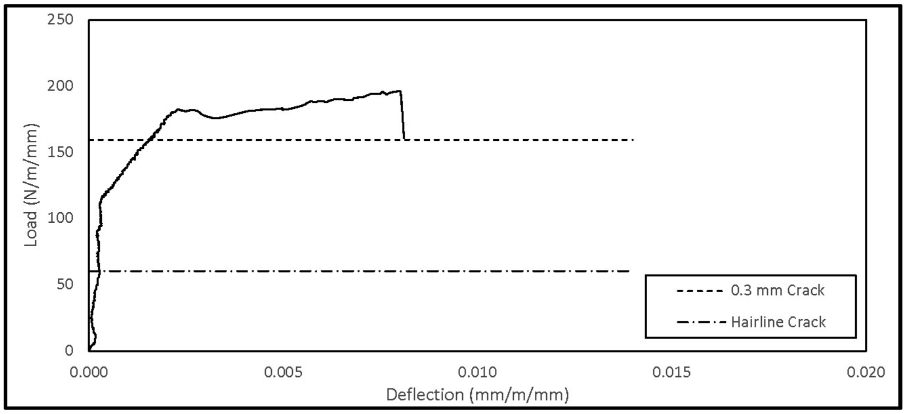

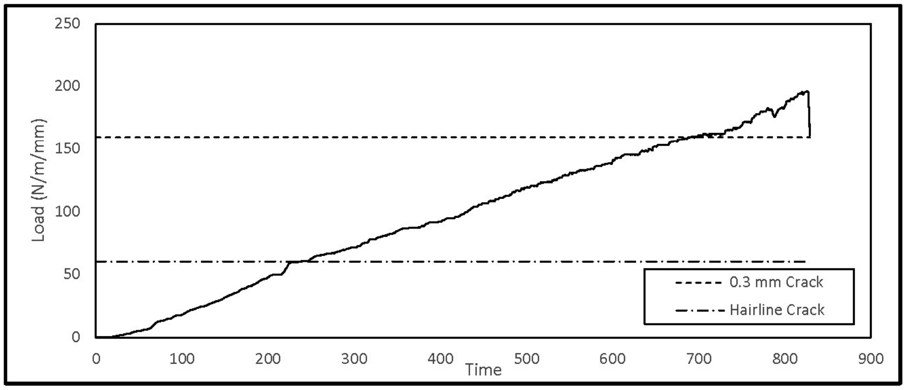

Curriculum Vitae

Name:	Abdul-Aziz Younis
Post-secondary Education and Degrees:	Western University London, Ontario, Canada 2013-2017 B.E.Sc.
Honours and Awards:	Western University Entrance Award Scholarship 2013
	JD Hole Global Opportunities Scholarship 2015
Related Work Experience:	Teaching Assistant Western University 2018-2020
	Research Assistant Con Cast Pipe 2018-2019
Publications:	**Younis, A.**, Ramadan, A., Wong, L.S., and Nehdi, M.L. "New Rational Test for Reinforced-Concrete Pipe Eliminating Subjective Crack-Width Criteria", *Structures*. Under Review.
	Younis, A., Shehata, A., Ramadan, A., Wong, L.S., and Nehdi, M.L. "Modeling Structural Behavior of Reinforced-Concrete Pipe with Single, Double and Triple Cage Reinforcement", *Engineering Structures*. Under Review.
	Ramadan, A., **Younis, A.**, Wong, L.S., and Nehdi, M.L. "Investigation of Structural Behavior of Precast Concrete Pipe with Single Elliptical Steel Cage Reinforcement", *Engineering Structures*. (2020).
	Ramadan, A., Shehata, A., **Younis, A.**, Wong, L.S., and Nehdi, M.L. "Modeling Structural Behavior of Precast Concrete Pipe with Single Elliptical Steel Cage Reinforcement", *Structures*. (2020).
	Ramadan, A., **Younis, A.**, Wong, L.S., and Nehdi, M.L. "Reinforced Concrete Pipe Design with Single Elliptical Steel Cage Reinforcement", *CSCE Annual Conference.* (2019).